FUNDAMENTAL STUDIES ON WHEEL WEAR IN ELID GRINDING

INDRANEEL BISWAS

BME (HONS), MS

A THESIS SUBMITTED

FOR THE DEGREE OF DOCTOR OF PHILOSOPHY

DEPARTMENT OF MECHANICAL ENGINEERING

NATIONAL UNIVERSITY OF SINGAPORE

2009

To

My Family

ACKNOWLEDGEMENT

I am grateful to my supervisor Assoc. Prof. A. Senthil Kumar for being a source of encouragement in the face of all research predicaments. I also express gratitude towards my supervisor Prof. M. Rahman for his advice to help me overcome hurdles. Without their support and their confidence in my research, completion of the thesis would be impossible.

I have heartfelt appreciation for Dr. Lim Han Seok whose praise for my research idea provided hope and confidence. I have been helped on several occasions by NUS staff, Mr. Neo Ken Son, Mr. Tan Choon Huat, Mr. Lee Chiang Soon, Mr. Nelson, Mr. Wong Chian Loong, Mr. Lim Soon Cheing, Mr. Simon, Mr. Ho Yan Chee and Mrs. Siew Fah, for which I am grateful to them.

I am grateful to my fellow research scholars at NUS, Tanveer, Ahsan, Pervej, Sharon, Woon, Haiyan, Xue, Masheed, Sadiq, Poh Ching, Lingling, Shaun and Asma, who have become valuable friends after sharing ups and downs of academic research.

I am not grateful to my friends, Manish, Arup, Mrinal, Satyaki, Meiling, Jinyun, Santanu, Mrs. Priyasree Home and Shalini for being friends in need, because expressing gratefulness towards them will make them shy.

I cannot be grateful to my Father, Mother, Brother, Sister-in-law, Neil and other relatives without whose belief, love and support I would not be, let alone the thesis.

TABLE OF CONTENTS

Summary

Metal bonded superabrasive grinding wheels are extensively used for machining and finishing hard and brittle materials, like mono-crystalline silicon, BK7 glass, silicon nitride, PVD hard coatings, etc, used in the electronics, optical, aerospace, nuclear and automobile industries. Electrolytic In-process Dressing (ELID) is perhaps the most popular technique for conditioning such wheels.

In ELID, electrolysis forms soft and brittle anodic oxide of the metal bond of the grinding wheel. This oxide is eroded off during grinding action, exposing new sharp abrasives and shedding off old worn ones, along with grinding chips. The mechanism of wheel wear in ELID is essentially through dissolution of the metal bond and investigation of the underlying electrochemical phenomenon is the key to wheel wear predictions. This is the basic approach of the thesis, which has not been the concentration of previous researchers.

The electrolytic dressing process sets aside ELID grinding from conventional grinding. Role of the electrolyte in the dressing process is first investigated. Other than electrolyte, the dressing process is also characterized by electrolytic current and thickness of anodic oxide layer. Fundamental behavior of the overall dressing process is investigated to understand the relationship of dressing conditions with oxide layer and electrolytic current and the process is modeled.

The combined effect of mechanical and electrolytic action during ELID grinding is then investigated by parametric study of wheel wear in ductile regime grinding. The process showed initial and steady stages of operation. The steady stage has cyclic

variations of grinding force and dressing current within specific limits such that the average value per cycle is constant. It is found that wheel wear rate in steady stage has a linear trend with a benchmark function defined from machining and dressing conditions.

Brittle mode grinding experiments with coarse abrasives are carried out to find that its steady stage of grinding does not have cyclic variations of force and current, but retains a stable value. This is because the rates of oxide erosion and formation reach equilibrium and maintains a stable layer thickness of oxide. Combination of the dressing theory and an oxide erosion model is used to simulate the dressing/electrolytic current which agrees with the experimental values.

Finally, an analytical and an empirical model for oxide erosion in ductile regime grinding are developed. Each of these is combined with the dressing model to simulate values of wheel wear rate and dressing current. The simulated values for steady phase of grinding agree with the experimental values. The models are verified with different types of experiments and are successful in predicting the profile of the ground component by compensating wheel wear.

LIST OF FIGURES

LIST OF TABLES

SYMBOLS AND ABBREVIATIONS

Symbols

c ratio of oxide volume to oxide minus metal volume

d_c depth-of-cut (μ)

d_r current duty ratio

f_r feed rate (mm/min)

f_l flow rate of electrolyte (lt/min)

h ordinate of control asperity

h_0 maximum height of control asperity

h_{ox} height of oxide from base of asperity

h_v thickness of oxide displaced by grinding chips

$i, i+1$ used as subscript for denoting rotation number

i current density

i_0 exchange current density

k_o 0.044 carat of abrasive per cm^3 of bond

k_x empirical constant for determining oxide erosion rate

k_{vg} volume of hydrogen generated per unit charge

l_c erosion of oxide layer per rotation of wheel representing wheel wear rate (μ)

l_{c0} initial value of mechanical wheel wear per rotation (μ)

l_e increase in layer thickness due to oxide formation per rotation of wheel (μ)

l_t wear due to pitting (μ)

m_r material removed per rotation of wheel

p concentration specification of grinding wheel

s_a density of abrasive (gm/cc)

s_m density of metal bond (gm/cc)

s_o density of metal oxide (gm/cc)

t time (sec)

t_i pulse increase time (μsec)

t_d pulse decrease time (μsec)

t_e time of electrolysis per unit rotation of wheel (sec)

w_r wheel wear rate

z valency of metal bond

Ac cross-section area of asperity

A_e cathode area (cm^2)

A_f area of new surface created by crack propagation

C_{PBR} PBR ratio

E_a electrode potential for the anode (V)

E_c electrode potential for the cathode (V)

E_f — energy for fracture

F — Faraday's constant (CGS units)

F_n — normal component of grinding force (N)

F_t — tangential component of grinding force (N)

G — Griffith Crack Propagation parameter

I — dressing current (amp)

I_{avg} — average current

L — oxide layer thickness (μ)

L_a — increase in wheel radius due to oxide formation (aka oxide growth)

$\dot{L}_{ec}$ — rate of oxide formation obtained theoretically from electrochemistry

L_g — inter-electrode gap (cm)

L_1 — maximum thickness of stable oxide during coarse grinding (μ)

L_2 — minimum thickness of stable oxide during coarse grinding (μ)

$\dot{L}_{ec}$ — hypothetical wheel wear rate

L_s — steady state thickness of oxide layer (μ)

L_t — minimum layer thickness beyond which pitting is initiated (μ)

$L_{\eta 2}$ — thickness of oxide layer corresponding to minimum current efficiency (μ)

M, M_m — molecular weight of metal bond

M_o — molecular weight of anodic oxide

R — Gas constant

R_e	resistance of electrolyte (Ω)
S	grinding wheel speed (rpm)
S_o	grinding wheel speed (m/sec)
T	temperature in absolute scale (K)
T_0	total time of dressing (sec)
T_{ON}	ON time of voltage pulse
T_{OFF}	OFF time of voltage pulse
V	voltage function (V)
V_{asp}	volume of the asperity from peak upto height h
V_0	peak voltage (V)
V_{Ω}	Ohmic potential drop
$\dot{V}_g$	volumetric gas generation rate
V_m	volume of metal bond (cc)
V_{ox}	volume of anodic oxide (cc)
V_r	resistance overpotential
V_t	total volume of bond and abrasive
V_v	volume of grinding chips generated by control area per rotation of wheel
α	fraction of overpotential associated with metal dissolution
β	and the volume proportion of gas in electrolyte
δ	increase/decrease of mechanical wheel wear rate per rotation
η	current efficiency (%)

η_1	maximum current efficiency (%)
η_2	minimum current efficiency (%)
η_a	activation overpotential
η_{conc}	concentration overpotential
η_H	current efficiency for hydrogen generation
λ	abscissa of control asperity (μ)
λ_0	base diameter of control asperity (μ)
ρ	resistivity of anodic oxide (Ω-cm)
ρ_e	resistivity of electrolyte (Ω-cm)
ρ_g	resistivity of electrolyte with gas generation

Abbreviations

CIB	cast iron bond
ECD	electro-chemical deposition
ECM	electro-chemical machining
ED	electro-discharge
EDM	electro-discharge machining
ELID	electrolytic in-process dressing
EWF	ELID wear factor
MR	material removal
MRPR	material removal per rotation

MRR   material removal rate

MWF   mechanical wear factor

PBR   Pilling Bedworth Ratio

SD   synthetic diamond

SDC   sufficiently dressed condition

UDC   under- dressed condition

WWR   wheel wear rate

Chapter 1

INTRODUCTION

1.1   Evolution of Abrasive Machining

The fundamental Abrasive Machining process has been in existence since the Stone Age with man rubbing stones against each other to produce sharp weapons. The Egyptians have been known to polish jewelry and vases. Chinese texts of the 13th Century document the use of seashell glued on parchment with natural gums, and used for polishing purposes. In the 15th Century, the Swiss have been known to use crushed glass on paper substrate as emery paper [1]. The first historical record of rotary grinding stone has been depicted in drawings in the 1st Century AD, and later in the drawings of Leonardo da Vinci [2]. Finally, the modern grinding machines were invented in the first half of the 19th Century for finishing clock parts [2]. Further industrialization led to the development of abrasive machining processes into the categories of honing, lapping, polishing and grinding, for achieving desired levels of surface finish and integrity.

The most popular abrasives used for these processes are silicon carbide (SiC) and aluminum oxide (alumina). SiC and alumina, historically known as corborundum and alundum respectively, were invented in the 1890s and have hardness of approximately 24 and 21 GPa respectively [3]. Till date, these grades of grinding wheels represent approximately half of conventional grinding and are used for a wide range of mass produced precision components [3].

Advancement of grinding technology took a leap unlike its initial slow paced evolution. The first computers like Z3, Atanasoff–Berry Computer (ABC), Electronic Numerical Integrator And Computer (ENIAC) were completed in the 1940s and marked the beginning of the Information Age. Integrated circuit (IC), invented in 1958, initiated the electronics industry which is still growing and Moore's Law states this growth in electronics performance to be approximately doubled every two years. The boost in the electronics industry has accompanied with a rapid progress in automobile, aerospace, optical, nuclear, communication and relevant industries. New fields of engineering like mechatronics, bio-engineering, MEMS and nano-technology have been founded as a result of this advancement, and have produced the need for advanced materials. Development of electronics has also introduced miniaturization.

Since the natural resources are limited, miniaturized products cater to the increasing population and maintain the exponential industrial growth. Increase in performance and miniaturization has been made possible through the use of innovative and advanced materials with excellent physical properties. So, hard and brittle, difficult-to-cut materials like optical glasses, cemented carbides, PVD hard coatings, single crystal materials (like silicon), advanced ceramic materials (like alumina, silicon nitride, silicon carbide and zirconia), due to their advanced mechanical, chemical and electrical properties, have become popular choice of the industries. However, the enhanced properties which make the materials suitable for the industries also challenge the existing manufacturing engineering and innovation.

1.2   Advances in Grinding Technology

Grinding technology kept pace with these increasing demands of the new age materials and had to evolve from the use of conventional SiC and alumina abrasives.

Grinding of hard and brittle, difficult-to-cut materials require the use of superabrasives like cubic boron nitride (CBN) and synthetic diamond (SD), which were invented in the 1950s by the researchers of the General Electric Company. These abrasives have the advantages of long tool life and dimensional stability because of high hardness (56 - 102 GPa for SD and 42 - 46 GPa for CBN [3]), wear resistance and thermal stability.

Application of hard and brittle materials was boosted with the advent of ductile regime grinding during 1980-90. Grinding thus bridged the gap between the coeval conventional grinding (with MRR greater than 0.1 mm^3/mm/sec) and super-finishing processes (with MRR upto 10^{-4} mm^3/mm/sec) [4]. The state of the art of grinding can now encompass a wide range of MRRs, from bulk removal/machining of difficult-to-cut materials [5], to components requiring polished surface finish and parts requiring high profile accuracy [4, 5].

But abrasives are not the only important constituents of the grinding wheel which delivered the desired results. Bonds, like abrasives, are also of immense importance which dictates the results of the ground surface. Hard and thermally stable vitrified bonds are often used with SD and CBN abrasives (specially vitrified bonded CBN wheels) for its self-sharpening/self-dressing effect by fracture of the porous bond [6].

However, metal bonds are most extensively used with superabrasives [7] for grinding of hard and brittle materials. They deliver highest surface finish values for ceramics, for the same grain size, as compared to resin and vitrified bonds [8]. Metal bonds have excellent abrasive retention capability [9] due to their toughness and wear resistance. Also, metal bonds are indispensible in high speed grinding (from grinding speeds of 60 m/sec in 1980 to 200 m/sec by 2007) for the ability to withstand the hoop and radial stresses generated due to high centrifugal forces [3].

1.3   Challenges in Wheel Dressing

Whereas the hardness, thermal resistance and tool life of the metal bonded superabrasive wheels is advantageous for difficult-to-cut materials [10], conditioning (truing and dressing) of such wheels become a challenge. Conventional techniques employ diamond dresser, or silicon carbide, or alumina wheel/stone for mechanical truing and dressing. Such crude mechanical dressing techniques can also damage the abrasives which affect the precision grinding operation. Moreover, these dressing techniques being intermittent can add to unproductive time.

Laser, electro-discharge and electro-chemical technologies have been employed to ensure dressing of such wheels. Dressing with laser technology was introduced by Westkamper [11] during in-process dressing of resin bonded CBN grinding and has now evolved for metal bonds. Laser dressing of metal bonded diamond wheels causes damage to abrasives by graphitization and micro-cracks, and the molten metal bond also re-solidifies [10] and is perhaps the reason for being more popular with vitrified bonded wheels. It also requires expensive equipment.

Electro-discharge dressing (EDD) and truing of metal bond grinding wheels was probably first proposed by Suzuki in 1987 [12] and has, since then, been researched thoroughly [13-17] with dry discharge, mist-jetting, and flowing electrolyte. Like laser dressing, EDD is also associated with the problems of graphitization of the diamond due to high thermal energy [15].

The most successful dressing technique for metal bonded superabrasive wheels is by the use of electrochemical technology, pioneered by Murata in 1985 [18], when introduction to electrolytic in-process dressing was made for grinding high-strength ceramics. Several articles on electrolytic and electro-discharge dressing were

proposed since 1985 in Japan [19]. Several pioneering works on electrochemical dressing has been carried out since [19-28].

1.4   Introduction to ELID Grinding

During ELID grinding, electrolysis is initiated between the metallic wheel as anode and a conductive cathode charged by a high voltage pulsed power supply. Electrolyte, which also doubles as a coolant, is continuously flushed between the electrodes. The metal bond is electrochemically dissolved simultaneously with the grinding action, so that the worn off abrasives are also removed, and new sharp ones are exposed to carry out efficient grinding. Dissolution of the bond also removes the grinding chips sticking to the wheel. The most popular electrolytic dressing technique, which has been coined 'Electrolytic In-process Dressing (ELID) Grinding' employs special electrolyte so that the metal forms an anodic oxide.

Research has concluded ELID Grinding to be very effective *in producing high quality surface finish* and *in bulk removal of hard and brittle materials*. It has been reported to produce nano-level surfaces and also fabricate micro-components. The process has undergone several modifications to increase its efficiency and effectiveness in order to suit the delivery requirements of a wide range of products.

With the increasing demands of the industries on surface finish parameters, requirements on *profile accuracy of components* have also increased accordingly. Profile accuracy of ground surface depends on (i) tool wear and (ii) high precision, high stiffness machine tools. The later is readily available to the precision industries, and the former depends on the understanding of the fundamentals of the grinding process itself. Once the wheel wear can be estimated with prediction algorithms, or measured with suitable instrumentations, compensation of the grinding parameters

can be carried out accordingly and profile accuracy of ground components can be obtained.

Understanding of the wheel wear phenomenon requires rigorous fundamental research. ELID grinding is a combination of electrochemical and mechanical processes and given the stochastic nature of the grinding process, wear predictions become difficult. Considering the amount of fundamental research on other established electrochemical processes, like electrochemical machining (ECM) and electrochemical deposition (ECD), the state of fundamental research on ELID has a lot of room for expansion. By definition of ELID, electrochemical reactions are supposed to be the mode of bond wear, and since electrochemistry is a more deterministic science than wear of grinding wheels, it is worthwhile to probe in that direction. This approach to investigation of ELID grinding requires studying the electrolyte properties, dressing process, and experimental observation of wheel wear.

1.5   Arrangement of Thesis

The study is started, from the next chapter, with an in-depth analysis of the existing literature on ELID grinding so that the fundamental process is clearly understood and the precise direction and target of the thesis is decided. The experimental setup and procedures are discussed in Chapter 3. In Chapter 4, the study of electrolytic dressing is initiated with investigation on the mechanism of electrolysis and electrolyte. The oxide layer formation and current during electrolytic dressing process is theoretically and experimentally examined in Chapter 5. Combination of electrolytic dressing and grinding is observed by experimental study of wheel wear in Chapter 6. The next chapter describes a semi-empirical model for wheel wear through the combination of the dressing theory and empirical relation for oxide erosion. Analytical model for

oxide erosion is proposed in Chapter 8. The models are evaluated with three case studies including profile estimation experiments in Chapter 9. The final chapter discusses the conclusions and contributions of the thesis, and also explores possibilities of future works.

Chapter 2

LITERATURE SURVEY

Murata pioneered the concept of dressing of metal bonded grinding wheels with electrochemical technology in 1985 [18] by introducing electrolytic in-process dressing for coarse grinding of high-strength structural ceramics. Several articles on electrolytic and electro-discharge dressing were proposed since 1985 in Japan [19]. It was further enhanced by Ohmori in 1990 [20] by generating mirror finish surfaces on silicon wafers by the application of the same technology of ELID. Electrolytic technology for dressing was also independently studied by other researchers like Kramer [21], Lee [22] and Boland [23] who developed intelligent systems for optimizing and controlling the electrochemical dressing reaction based on the mechanical grinding rate. Suzuki [19] proposed an efficient two electrode electrolytic dressing technique with AC supply.

Over the last two decades, there has been significant advancement in research on ELID grinding. The reports can be broadly classified into the categories of (i) fundamental process, mostly during the initiation of ELID and some later studies; (ii) theoretical studies; (iii) process modifications, so that the process can be tailored to suit different applications and increase efficiency; (iv) performance of ELID grinding on different hard and brittle materials. Discussion on the first category will also include a detailed description of the process which is required before continuing further study.
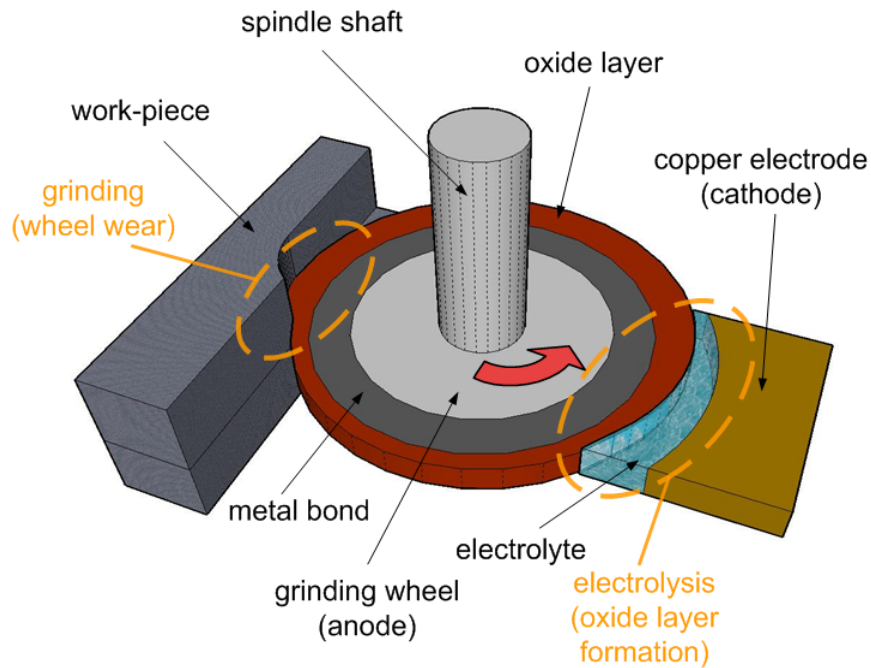
Figure 2.1: Schematic of ELID Grinding process

2.1 Fundamentals of ELID Grinding

2.1.1 Basic Mechanism of ELID Grinding

In ELID Grinding, electrolytic action takes place between the anodic metal bonded (generally cast iron, cobalt or bronze) grinding wheel and a conductive cathode separated by gap, usually in the range of 100 to 500µ, fixed according to requirement (Figure 2.1). The electrolyte, which doubles as a coolant is flushed into the electrode gap. Electrolysis is initiated with a high voltage (preferably 60 to 120V), DC, high frequency, pulsed power supply which forms a soft, brittle, friable and electrically insulating layer of anodic oxide by consuming the metal bond. Due to the soft and brittle nature of the oxide, it wears off easily during mechanical action of grinding and reveals sharp abrasives embedded in the metal bond matrix. Erosion of the oxide also removes the grinding chips and blunt abrasives. Since the oxide layer has high resistivity (insulating), its wear reduces the resistance and increases the dressing current, which in turn forms more oxide and the layer is reinstated. Subsequent

9

grinding again erodes the oxide, and the cycle continues as shown in Figure 2.2. So, it is essential for the oxide layer to be present for efficient ELID grinding. But it is not present at the start and a layer needs to be grown before commencing the grinding operation. This is called the *pre-dressing operation* when only the electrolysis with the wheel rotating is carried out for 10 mins [20] to 90 mins [24], as per user requirements.
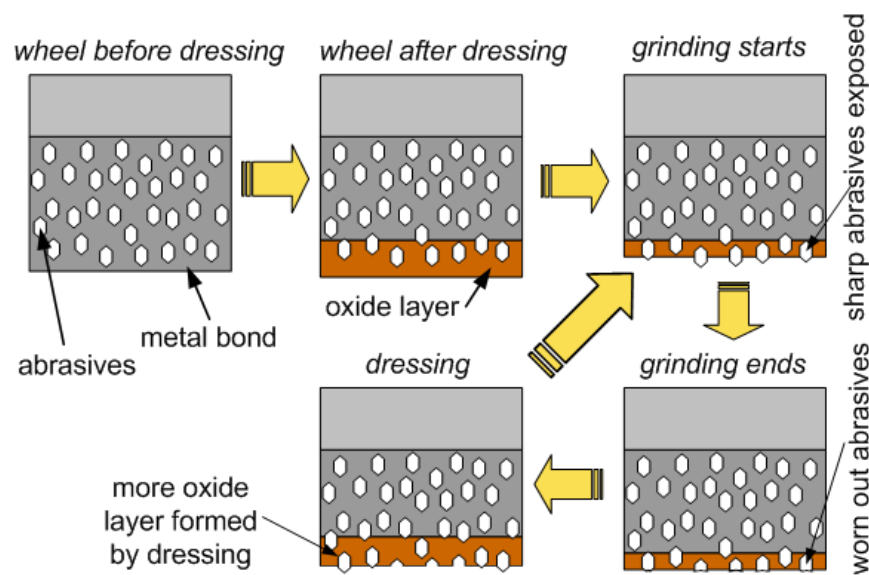
Figure 2.2: Mechanism of ELID Grinding

2.1.2 Detailed Analysis of ELID Grinding Mechanism

The fundamental operation of ELID grinding was initially reported by Murata for coarse grinding of structural ceramics [18] with #400 abrasive size. Ohmori proved the process to be valid for mirror finish of hard and brittle materials with reports on silicon wafers [20], silicon nitride and BK7 glass [25] by grinding with several ultra-fine abrasive sizes with several grinding schemes.

The electrolytic chemical reactions for the process were reported [26] for CIB (cast iron bond) wheel. Once made anodic, the iron dissolved into the electrolyte as ferrous and ferric ions. The electrolyte is dissociated into hydrogen and hydroxyl ions. The

negative hydroxyl ions move towards the anode to form ferrous and ferric hydroxides, which stick to the surface of the grinding wheel.

Ohmori [27] experimentally explored the variation of the electrolytic behavior and grinding forces for different electrolytes, input voltage wave forms, bond materials and several work materials. The change in current and voltage during pre-dressing was also touched, but the details of the power supply were not provided, due to which dressing behavior could not be properly ascertained. The DC power source developed the thickest oxide layer on CIB-D (cast iron bond diamond) wheel, followed by the pulsed DC and then the AC, but the amount of metal bond corroded (etched layer thickness) was found to be lowest for pulsed DC. So, pulsed DC became the common choice of power supply for ELID.

Bandyopadhyay [28], also contributed to fundamental understanding of ELID by discussing stable and unstable nature of grinding forces, among other observations. Lim [29] reported a very fundamental and detailed study of the process mechanism by conducting experiments with varying feed rates and duty ratios which were then compared with results for conventional grinding. The results concluded that the oxide layer built up to a certain thickness until the grinding forces reached high enough to break it, suddenly reducing its thickness along with resulting forces. With the oxide layer reduced, resistance dropped and the dressing current increased. It was also found that the oxide layer acts as a damper and enhances mirror finish generation. It was reported that a higher duty ratio decreases surface roughness values, but increases the wheel wear. There exists a threshold value of feed rate for grinding, beyond which grinding burn occurs because rate of wheel wear (oxide layer erosion) becomes higher than rate of its formation.

(a) brittle mode with 20%   (b) cracks with 40%   (c) ductile mode with 60%
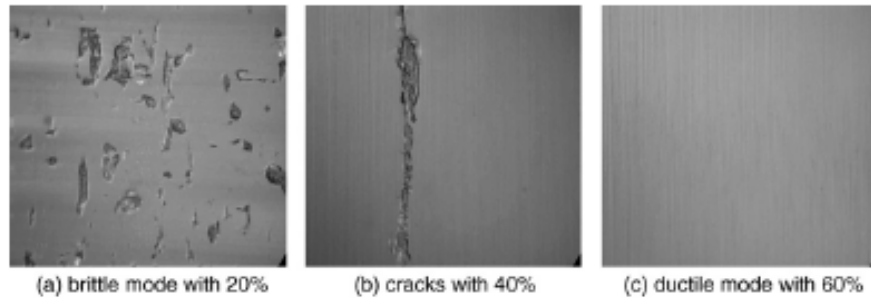
Figure 2.3: Brittle to ductile transition for BK7 glass for varying current duty cycle [30]

Ra 0.5629μm @ #325   Ra 0.1614μm @ #1200   Ra 0.0604μm @ #4000
(a)   (b)   (c)
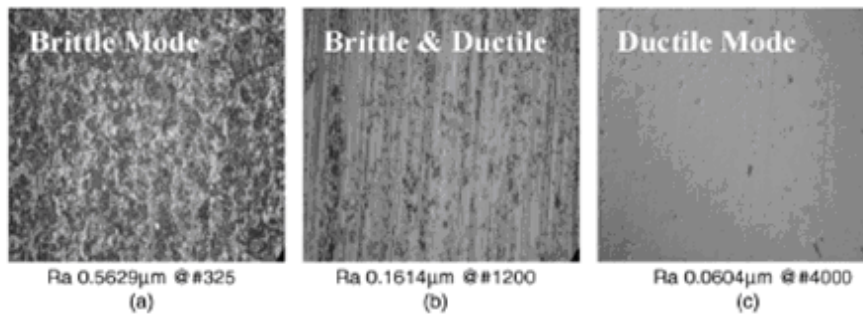
Figure 2.4: Brittle to ductile transition for BK7 glass for different grit sizes [30]

Mirror surface generation on hard and brittle materials is possible by ductile regime grinding [4]. Fathima [31] found that higher critical depth of cut with ELID can achieve mirror finish surfaces, as compared to conventional grinding. The oxide layer (active bond) was concluded to be responsible for ductile regime grinding, and so the grinding mechanics was proved to be highly dependent on electrolytic dressing. Mode of wheel wear was found to be macro-fracture which can be reduced with shorter pulse ON time. Damage on the work surfaces with respect to current duty ratio was reported by Kumar [32]. Cracks and brittle mode of material removal was found for low duty ratios (Figure 2.3), and better surface characteristics (ductile mode material removal) for higher duty ratios. The surfaces were compared with respect to different grit sizes, with brittle mode removal for higher grit sizes and ductile mode for finer ones (Figure 2.4).

2.1.3   Theoretical Analysis

Investigations on basic physics of ELID was first reported by Bifano [33], where the theoretical anodic metal dissolution rate was calculated based on Faraday's Laws of Electrolysis. Dressing experiments were conducted to find the wheel corrosion rate and oxide film/layer growth rate and compared with theoretical results. The effectiveness of the ELID technique was proved but its predictability and controllability was concluded to be poor because of material inhomogeneity (of the bond and the electrolyte) and effects of film formation in microscopic scales. Boland [23] and Lee [22] also investigated the process with Faraday's Laws of Electrolysis. Zhu [34] in the process of design and development a suitable electrode for electrolytic dressing of high speed ELID grinding also hinted the physics underlying the process.

It is not possible to analyze ELID grinding process, unless the dressing process itself is understood. Chen [38, 39] carried out extensive mathematical analysis for developing a model of the metal dissolution rate from the first principles of electric field variation on metal matrix, due to presence of diamond abrasives (insulators). The potential across the electrolyte was determined by Laplace equation, with suitable boundary conditions. Pavel [35], based on the research of Chen formulated a model for pre-dressing to predict the oxide layer thickness with a given dressing time and other parameters. Klocke [36] carried out fundamental experimental studies of electrolytic dressing behavior of various electrolytes on different compositions of bond materials. Chemical analysis of the resulting oxide was also performed as well as investigations on thickness of oxide layer and thickness of etched layer.

Fathima [37] proposed a model for ELID grinding based on the fact that contact between wheel and workpiece, in ultra-precision grinding, was not through abrasives but through asperities on the surfaces of wheel and work material. Several tests and

measurement of the wheel were carried out to find parametric values of the model and the simulated grinding forces for different parameters could be explain with experimentally obtained forces.

2.2 Types of ELID Grinding

A specialty of ELID grinding is that, it can be implemented by attaching some simple fixture and a power supply to any ordinary grinding machine [20]. Part of the fixture includes an electrode, and for in-process dressing, the electrode should be adjacent to the grinding wheel working surface. But often, due to the shape of the work material/work surface or working area constraints some modifications are required and has lead to the following types of ELID [38]:

i. Electrolytic in-process dressing (ELID-I)

ii. Electrolytic interval dressing (ELID-II) (Figure 2.5)

iii. Electrolytic electrode-less dressing (ELID-III) (Figure 2.6)

iv. Electrolytic electrode-less dressing using alternating current (ELID-IIIA) (Figure 2.7)
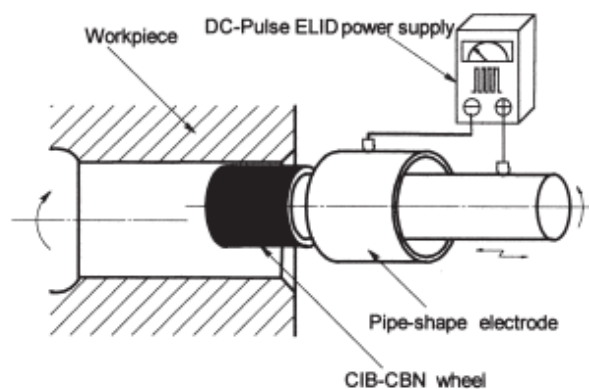
Figure 2.5: Schematic of internal grinding with ELID-II [39]
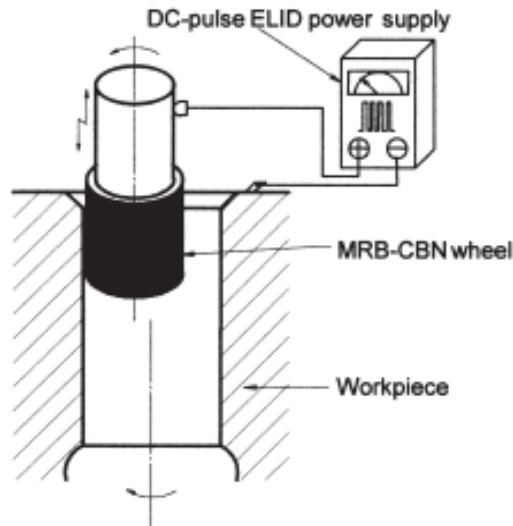
Figure 2.6: Schematic of internal grinding with ELID-III [39]
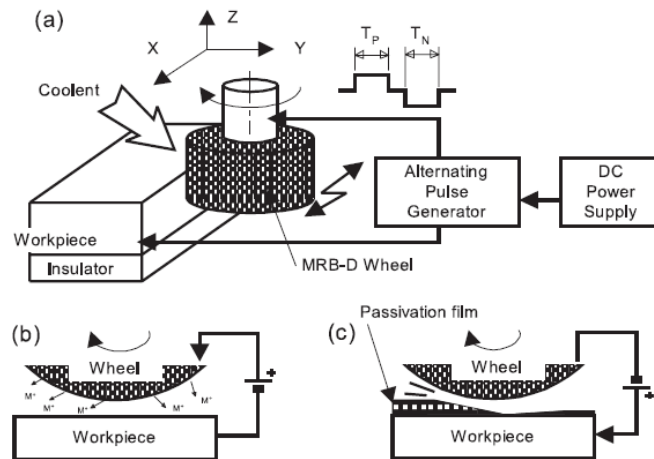
Figure 2.7: Schematic diagram of ELID-IIIA [38] (a) ELID-3 machining system with alternating current. (b) ELID without electrode. (c) Electrolysis of workpiece

The common elements in all these processes are the metal/resin bond wheels, DC power supply (except ELID-IIIA) and electrolyte coolant. ELID-I is the basic grinding scheme that has already been discussed. ELID-II uses a fixed electrode for interval dressing. ELID-III (Figure 2.6) is electrodeless, and is used with a metallic workpiece that is maintained at negative potential (but is carefully isolated from the machine body) [39]. This will also bring in unwanted spark erosion as the mode of material removal but can be avoided or restricted using some simple measures.

There are some other variants. *ELID-Lap Grinding* [24, 40] uses controlled force for material removal to avoid damage to work surface. *Electrical Grinding Technique* [41] is similar in principle to ELID Grinding, where the metal workpiece is superficially oxidized to enhance finished surface properties. A *new ELID grinding technique* was developed where the electrolyte flows through a nozzle, between two plate in-built electrodes, when it is dissociated into ions. As the ions strike the electrically neutral grinding wheel, the oxide/hydroxide of the metal bond takes place [42]. It is imperative that the electrolyte loses some ionization as it leaves the electrode gap, and the resulting dressing rate is very low, suitable for fine grinding/fabrication of micro-components. An *ELID Truing System* was devised by Saleh [43] by implementation of an intelligent control system which increases current proportional to the run-out of the wheel segment being dressed. Several other modifications of ELID grinding are also present, but not in the process level, but in the component level. These have been dealt in the next section.

2.3   ELID Grinding System and its Developments

Over the years, components of ELID grinding have been modified for higher efficiency, additional advantages, process control and to suit specific product requirements and are listed below:

2.3.1   Power Supply

Murata [18], Kramer [21] and Boland [23] developed power supplies for controlling and optimizing dressing and grinding rates. More recently, Patham [44] devised a power supply which, based on optimal dressing data, keeps the dressing current constant for varying grinding conditions.

2.3.2 Cathode

A new foil electrode, based on the principle of hydrodynamic bearing action, was introduced by Zhu [34, 45] to eliminate the air film and enable contact between rotating wheel and electrolyte. The injection electrode (IE), was suggested by Islam [46] which doubles as the cathode as well as the device for ejecting electrolyte and enables better contact of electrolyte and wheel to ensure efficient oxidation.

2.3.3 Machine

Results of in-process measurement of wheel wear and work profile geometry can be used to compensate the grinding parameters so that the resulting work profile can have a close tolerance. An intelligent machine tool (Figure 2.8) with these control and sensor systems was developed by Saleh [47] and Sazedur Rahman [48]. A desk-top 4 axis ELID machine, 'Trider-X', was developed for micro-fabrication purposes [49].

Figure 2.8: Developed ELID machines at NUS [47]

2.3.4 Grinding Wheel

Itoh developed a novel metal-free resinoid ELID grinding wheel for better surface roughness [50] in which the oxide wears off easily and yet retains a high frictional coefficient compared to CIB. Saito [51] developed grinding wheels to control the

subsurface composition of the workpiece and enhance its properties with controlled diffusion of elements from the wheel.

2.3.5   Truing

Since the power supply used in ELID grinding can be same as EDM power supply, electro-discharge truing (ED Truing) is often used prior to ELID grinding (Figure 2.9) [39, 52-54]. Successful truing with ELID technology has not been reported by Saleh [43].
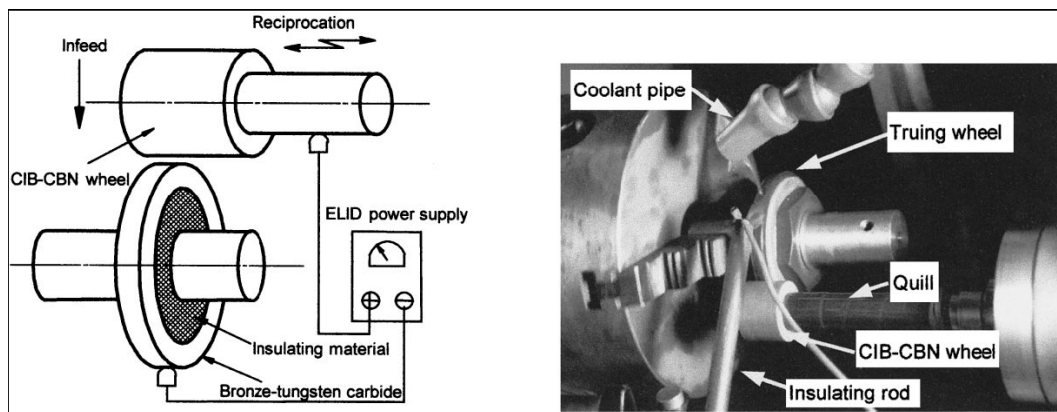
Figure 2.9: ED-truing scheme [39]

2.3.6   Electrolyte

Specially developed electrolyte was introduced by Ohmori [55] for grinding bio-compatible alloys.

2.4   Applications of ELID

Theoretically, ELID Grinding can be applied to any material which can be ground by conventional grinding, as long as it is not soluble or reactive to the electrolyte. Reports on applications of ELID grinding to various materials and the resulting surface finish are vast. A gist of the important papers on some critical work materials are given in this section. Common information in most of these papers is the

generation of predominant ductile mode material removal for mirror surfaces, and brittle mode for lower quality surfaces with different grinding parameters (Figure 2.3 and Figure 2.4).

Figure 2.10: Mirror surface generation on Si wafer [30]

Silicon: Ductile regime grinding. Creep-feed, in-feed and rapid feed grinding schemes carried out [20]; Combinations of grinding and dressing parameters used. Subsurface damage detected. Cracked layer detected to depth of 1.3 µ for #2000 and 0.4 µ for #8000 wheels. 3.29 angstrom Ra achieved for lapping with #3000000. Upto 3.0 nm Ra reported with CIB-D #120000. [25]; ELID lap grinding on single sided lapping machine. No brittle fracture was present along grain paths for all abrasive sizes. [40]; Wafer thinned from 750 to 70 µ. New electrolyte injection cathode introduced. 6 nm Rt reported. (Figure 2.10) [46]; Detailed investigation of ELID Grinding characteristics. Intermediate range of current duty ratio and feed rates reported to produce better surface finish. Lower subsurface damage reported [47, 56];

BK7 glass: Material removal by brittle fracture predominant for lower grit size as compared to higher ones. Constant in-feed pressure, speed and depth-of-cut in conventional lapping machine. [25]; Tool wear ratio reported upto 0.24. 8 nm Ra reported with #4000. [29]; Variation of surface roughness with duty ratio investigated [32]; ELID lap grinding on single sided lapping machine. No brittle fracture was

present along grain paths for all abrasive sizes. Depth of grinding mark for #3000000 was 1.7 nm. 2.8 nm Rmax achieved with MRB-D #3000000. [40];

Si$_3$N$_4$: Material removal by brittle fracture predominant for lower grit size as compared to higher ones. [25] Creep feed grinding. Ra value increased for higher mesh size wheels with increasing feed rates (80 to 200 mm/min). Depth-of-cut was at 1 μ per pass. [26]; Study for high MRR. Reduction of grinding forces by applying ELID. Stable grinding was performed at MRR of 500 mm^3/min. Intricate shapes of Si$_3$N$_4$ blocks produced. [28]; Cutting action was successful though the MRR gradually reduced. [33]; Successful ELID grinding for mirror surface generation reported with Ra 7nm for #4000 grit. [56]; Study of flexural strength. Significant increase in bending strength (740 to 806 MPa) after ELID grinding of specimens. Ductile mode grinding reported. Depth of cracked layer investigated [57];

SiC: MRR was higher for ELID. Constant force (5N) plunge grinding. Combinations of electrolyte (NaCl solution) concentration with pulse types compared. [33]; In-feed grinding of CVD-SiC film. Surface roughness by ELID was slightly better than ordinary grinding. [58]; Subsurface effects of Sintered SiC, Zerodur, CVD-SiC investigated. Ideal depth-of-cut was 0.4 μ of #4000 for the materials. 8 nm Ra with SD #4000 [59];

Bearing steel: Cylindrical grinding in plunge mode and traverse mode. Traverse mode grinding reported preferable to plunge mode. ELID produced better surface roughness, skewness and slope, compared to honing and electric polishing, though the machining efficiency reported to be lower. Residual compressive stress of 150 to 400 MPa reported. ED truing used to reduce wheel run-out to 3 μ. [52]; Detailed surface roughness analysis. Carbide pull-out was arrested with use of ELID, though burnishing action of the grits reduced. Upto 7 nm Ra and 46 nm Rz achieved with

#200/230 grits. [60]; ELID-II, Internal grinding. Pipe electrode & arc electrode compared. ED-truing and ELID grinding. [39]; ELID-III, Internal grinding. Harder materials with better surface finish [39];

Al$_2$O$_3$: *Small hole grinding* characteristics investigated. ELID-II grinding. Small hole grinding. ED truing carried out. Entrance and exit feed rates of the grinding wheel play important role in final finish. [53]; Study on Surface roughness. ELID-II, Internal grinding. *Pipe electrode & arc electrode* compared. ED-truing and ELID grinding [39];

Small parts of hardened steel, SKD61, Si$_3$N$_4$, ZrO$_2$ ferrule, ZrO$_2$: *ED-truing, Centerless grinding*. Detailed report on surface roughness values for different grit sizes. Mirror finish reported [54];

WC, Si and Complex material of Si and WC: Surface roughness study. *ELID lap grinding*. Material removal mechanism for coarse grits was predominantly brittle and that of finer grits was more ductile. Transition from brittle to ductile mode was at #8000 for Si. It was #4000 for WC and also #4000 for the complex material. 3.8 nm Ra of WC reported with CIB-D #4000 [24];

SKD11, SKH51, WC-Co: *ELID-III, Internal grinding*. Harder materials reported to have better surface finish. Lower current level should be chosen for ELID. Mirror finish obtained in ordinary grinding machine. Upto 4 nm Ra achieved with #4000 [39];

TiAlN film on cemented carbide substrate: *Tribological characteristics investigated*. Low friction co-efficient, low wear rate after ELID grinding. Oxide layer produced on machined surface. 2.4 nm Ra reported with #30000 [61];

AlN: *Surface modifying effects* studied. *Oxygen diffusion to the ground surface* was reported, the effect of which was higher hardness and better sliding characteristics. Roughness of 8 nm with #30000 wheel [62];

Schmidt plate (fused silica plate): *Form accuracy* and surface roughness for large surface reported. 1.2μ/270mm p-v and 2.8μ/180mm p-v in x and y directions respectively. p-v 2.5 μ in 300x200 mm after tool path compensation. Final profile was generated by polishing [63];

Fused silica and fused quartz: Specimens ground in *high rigidity grinder* Tetraform C. *Acoustic emission* used to monitor in-process grinding conditions to control finished surface and subsurface quality. Fused quartz roughness reported from 2 to 3 nm rms [64];

Cemented carbide alloy: *New ELID system* reported. *Micro-tools* with tip diameter of less than 1μ developed. Surface modifying effects and workpiece strength improvements reported [42];

2.5 Discussion

There is a comprehensive amount of research on the applications of ELID grinding. Almost all the literature on ELID applications has reported enhanced surface finish of work material. Few papers [48, 63] have reported profile accuracy of the ground component achieved by control of grinding parameters from feedback of profile measured intermittently in-process. Yin [63] used highly specialized sensors and control systems which are too cumbersome and expensive for commercial industrial application and the innovative technology of Sazedur [48] needs to be improved.

Significant improvements and modifications of ELID grinding have also been reported to cater special applications, like micro-component fabrication, and grinding biomaterials, and impart additional properties to the work material, like enhance tribological properties and oxidation of ground surface. Power supplies have been designed to increase the efficiency and to control the dressing process by monitoring the grinding operation.

Among the theoretical studies, Bifano [33] suggested a partial model of dressing and an explanation for the thickness of oxide film/layer. The experiments were based on bronze bond grinding wheels and NaCl solution was used as electrolyte (which is not generally used in modern commercial ELID). The report did not discuss the specialty of ELID grinding mechanics due to presence of the oxide layer. Chen [65, 66] suggested a model for anodic dissolution but did not involve the effect of the oxide layer. Physics of the electrolytic process was also partly explained by Lee [22], Kramer [21] and Zhu [34], but were not successful in providing a complete formulation for the dressing process. Pavel [35] developed a formulation for pre-dressing but the theory was not sufficiently substantiated with experimental results. Lim [29] and Fathima [31] explained the working mechanism of ELID grinding in great detail, but correlation between input parameters and process signals could not be quantitatively defined. In a later work of Fathima [37], relation between grinding forces and grinding input parameters was obtained, but there was no consideration for wheel wear.

Fundamental work on electrolysis was reported by Ohmori [27] where oxide thickness was investigated for various electrolytes, bonds and power supplies. Voltage and current characteristics during pre-dressing was also mentioned, but the details of

the power supply was not revealed. Klocke [36] carried out similar work on bronze bonds in detail.

It is clear from the above discussion that wheel wear in ELID has not be studied in detail. Profile accuracy is largely dependent on wheel wear. Wheel wear mechanism was explained by Fathima [31] from experimental results, who concluded wheel wear to occur by macro fracture of the oxide layer. Lim [29] reported the ELID grinding forces and dressing current to be periodically varying with unpredictable frequency. Both, macro fracture and periodically varying grinding forces point towards unpredictable wear mechanism. So, correlation between wheel wear and input parameters could not be obtained. Ideally, wheel wear in ELID grinding takes place by electrolytic dissolution of the metal bond and consequent oxide formation. A meticulous and methodical study of the electrolytic process and the oxide erosion phenomenon can reveal greater insight on wheel wear, and will be an important contribution to ELID grinding research.

2.6 Scope of Work

Electrolytic action forms a layer of soft and brittle anodic oxide on the grinding wheel which wears off as a reaction to the grinding of work material. So, the metal bond is consumed by electrolytic action i.e. wheel wear in ELID grinding occurs through electrochemical reaction. Rate of oxide formation is directly proportional to electrolytic current. Again, electrolytic current (aka dressing current) depends on the applied potential and the mechanism of electrolysis. The later depends on the properties of the electrolyte flow system and the existing oxide layer. So, *study of the electrolyte for investigating its properties relevant to dressing current* is important but unreported.

Properties of the electrolyte and the fundamental mechanism of electrolysis being known, they are applied in theorizing the dressing process. Thus, the *dressing current and oxide layer are correlated to the applied voltage and electrolyte flow system.* Experimental inspections of the dressing behavior and oxide layer properties are also carried out under different conditions.

Investigations on dressing behavior being completed, the overall process of ELID grinding is then examined through rigorous experiments. The *mechanism of the process is scrutinized with specific reference to wheel wear and dressing current,* so that their variation with respect to various input conditions can be realized.

Derived theory of electrolytic dressing is combined with knowledge of grinding mechanism to develop models for ELID grinding. The models provide deeper understanding of the process and *predict dressing current, and wheel wear rate* and also used to predict profile accuracy of ground components.

2.7 Objectives of the Thesis

Based on the discussion in the previous section, the objectives of the thesis are defined as follows:

- *Study the mechanism of electrolytic dressing and investigate the properties of the electrolyte flow system affecting dressing current.*

- *Characterize the electrolytic dressing process by establishing definite relationship of dressing current and oxide formation with applied potential and electrolyte flow system as input conditions.*

- *Experimental investigation of the mechanism of ductile regime ELID grinding with special emphasis on parametric study of wheel wear to establish an empirical benchmark function.*

- *Formulate models of dressing current and wheel wear rate in ELID grinding.*

- *Evaluate the models for achieving profile estimation of ground components.*

Chapter 3

EXPERIMENTAL SETUP

AND PROCEDURES

The objectives of the thesis can be accomplished by investigating the character of (i) electrolytic dressing, and (ii) wheel wear through experiments, and subsequently examine the results to find a theoretical explanation. Described in this chapter is the basic experimental setup and procedures used in this study.

3.1   Setup Equipment
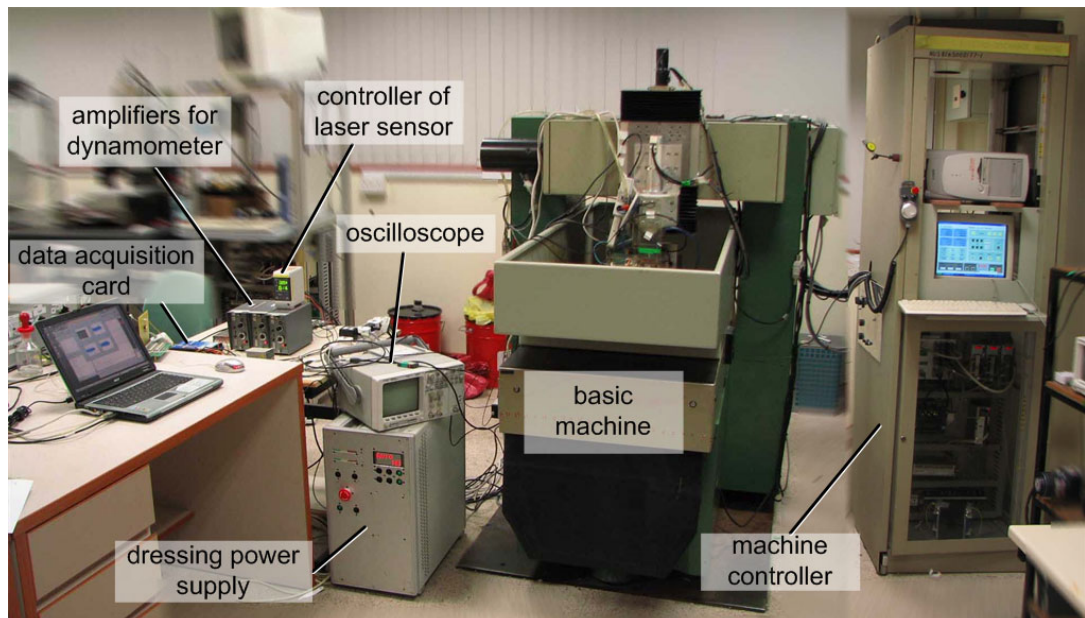
Figure 3.1: Complete experimental setup with machine tool and sensor instrumentation

The basic experimental setup consists of a (i) NC (numerical control) Machine Tool, used with a (ii) High Voltage Pulsed Power Supply for electrolytic dressing, as shown in Figure 3.1. A data acquisition card is used to record the required signals from the sensors to the computer.

3.1.1   NC Machine Tool
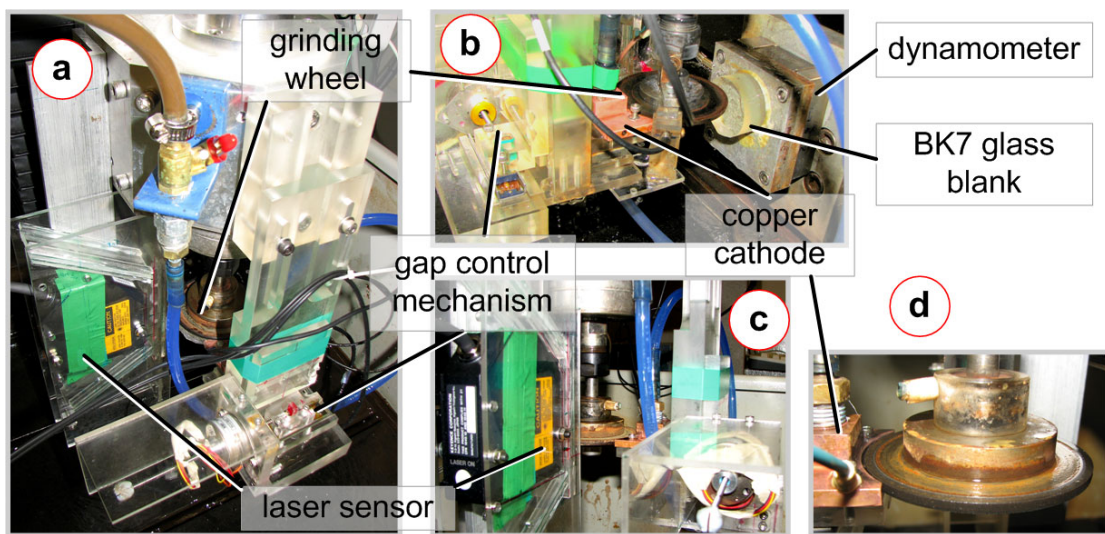
Figure 3.2: Close-up photographs of the grinding scheme with sensor and fixture accessories

The NC machine tool is indigenously developed, from a 4-axis machine tool body refitted with AC servo motors [47]. Information on the machine axes are given in Table 3.1. The scheme used for the experiments is vertical surface grinding with a flat wheel (plunge grinding) of type 1A1, as shown in Figure 3.2. The copper electrode conjugate to the wheel, which covers 90° of the wheel sector, doubles as an injector for electrolyte (Figure 3.2) [46]. The injecting electrolyte ensures better contact of electrolyte and wheel. It is attached adjacent to the wheel using a fixture. The fixture incorporates an adjustment mechanism for manipulating the electrode gap. The electrolyte delivery system is also fitted with a manual flow control valve so that the flow rate can be metered as required. The experiments require on-machine

measurements of grinding forces, dressing current and grinding wheel profile and the relevant sensors used are as follows, and are depicted in Figure 3.2:

i. A Keyence[®] laser displacement sensor (LDS), with a resolution of 100nm, is attached to the main spindle in a way that enables measurement of the grinding wheel profile, and its output can be used to obtain the change in wheel radius.

ii. A 3-axis Kistler[®] dynamometer is used for measurement of grinding forces. Its signal is processed by amplifiers before being recorded in the computer with the DT9800 series data acquisition card of Data Translation[®] (10 kHz).

iii. An Agilent[®] current probe is used to measure the dressing current and its signal is also recorded with the data acquisition card. An Agilent[®] oscilloscope is used for continuous display of the current and force signals.

Table 3.1: Axis specifications of the NC machine

Parameters	X axis	Y axis	Z axis
Full stroke (mm)	250	250	150
Resolution (μ)	1	1	1
Natural frequency (Hz)	817	2000	1429
Damping ratio	0.0765	0.086	0.014

Cast iron bonded (CIB) wheels with synthetic diamond (SD) abrasives of different sizes and wheel diameter of 75 mm and thickness 3 mm, are used in the study. The electrolyte used is of grade CIMIRON CG7, and both the electrolyte and wheels are purchased from FujiDie[®], Japan. The electrolyte is diluted with approximately 50 parts of water to maintain a pH of 10 to 11.

3.1.2 Dressing Power Supply

The high voltage pulsed power supply used is capable of generating variable square pulse ON and OFF time from 2 μ-secs with peak voltage from 30 to 105 V. It has an internal resistance of 1 Ω. This ensures high and almost constant working voltage across the electrode gap for all current values.

3.2 Procedure

Three kinds of experiments are performed with the setup described, viz,

  i. experiments for measuring impedance of electrolyte,

  ii. experiments for finding the current and oxide layer formation characteristics during dressing,

  iii. experiments for finding process forces, dressing current and wheel wear during ELID grinding.

3.2.1 Measurement of Electrolyte Impedance

Impedance studies of the electrolyte are required so that examinations on the electrolytic dressing process can be carried out. In general, impedance of the electrolyte is studied by the electrochemical impedance analysis which uses a three electrode system. One of the electrodes should be placed in the electrode gap, which in case of ELID is in a very small range of 100 to 500μ, and is hence practically impossible to achieve [36]. If the impedance of the static electrolyte is measured, then its change with flow rate, dimension of electrode gap and grinding speed cannot be ascertained, and will hence lose all practical significance. So, the impedance has to be measured in a different way. Therefore, the oxide is scrapped off the CIB wheel with an abrasive cloth (Scotchbrite[®] industrial grade) and electrolysis is initiated with the

pre-determined voltage and electrolyte flow settings. A layer of oxide covers the metal wheel surface over a brief period of time. However, the oxide formed during the first 100 milli-seconds is negligibly small because the variation of current over this time is also negligible (within 0.5%). The current response over this time period is used to carry out the impedance analysis of the electrolyte.

3.2.2   Dressing Experiment

Dressing takes place with the formation of anodic oxide when current is passed between the grinding wheel and the cathode in presence of the electrolyte. Formation of oxide on the wheel results in increase of its radius, because the volume of iron oxide is higher than the volume of iron it consumed. Increase in oxide layer thickness also results in increased resistance to current flow. So, dressing current and oxide layer thickness are two different outputs of the dressing system. The inputs are the power supply characteristics of *peak voltage, pulse ON time and OFF time*, and the electrolyte flow character determined by *grinding speed, inter-electrode gap and electrolyte flow rate*.

The behavior of current and oxide layer thickness over a period of electrolysis is determined by the dressing experiments. Oxide layer thickness cannot be measured directly and so increase in the wheel radius is measured with the LDS from which the layer thickness is calculated. Dressing current is measured with a current probe. Electrode gap is fixed to a pre-determined value with the gap-control mechanism; the flow is fixed with the flow control valve; and grinding speed is controlled by spindle speed control with machine controller. Dressing operation is carried out for 40 mins and the wheel radius and dressing current are measured at regular intervals of 5 mins.

Continuous splashing of the electrolyte on the grinding wheel does not allow proper triangulation of the laser from the displacement sensor, and the wheel has to be dried before its profile measurement is possible. This is achieved by rotating the wheel at 2000 rpm for 5 minutes so that the centrifugal action ejects the electrolyte adhering to the wheel. Consequently, the wheel wear is measured intermittently during the experiments.

3.2.3   Grinding Experiments

Experiments are carried out to investigate the wheel wear rate (WWR) and dressing current in ELID grinding for various input parameters (*depth-of-cut, fed-rate, spindle speed* and *duty-ratio*). Wheels with abrasive sizes of #1200 (mean dia. 13µ) for ductile mode grinding and #325 (mean dia. 44µ) for brittle mode grinding are used. Inter-electrode gap is maintained at 250µ.

In order to ensure that initial condition of the wheel is the same for all experiments, 20 minutes of pre-dressing is carried out with wheel speed of 5.89 m/sec, 1.8 lpm electrolyte flow rate, 250µ inter-electrode gap with peak voltage of 100V and pulse ON and OFF times of 10µsec each.

Workpiece used is BK7 glass blanks of diameter 40 mm. Horizontal grinding of the entire surface is carried out (Figure 3.2b) and the grinding locus is designed to eliminate idle strokes which produce oxide without immediate mechanical wear (Figure 3.3). It is also ensured that the grinding surface of the wheel does not overlap with the ground surface generated by the last horizontal pass, i.e. the distance between the horizontal passes is equal to the wheel thickness. This ensures equally distributed wear along the width of the wheel.

Measurements of grinding forces, dressing current and wheel radius are taken. Force and current are measured after regular intervals for 30 to 45 secs. Wheel wear is measured after 5 passes of material removal, and the method of measurement is the same as the one used for dressing experiments.
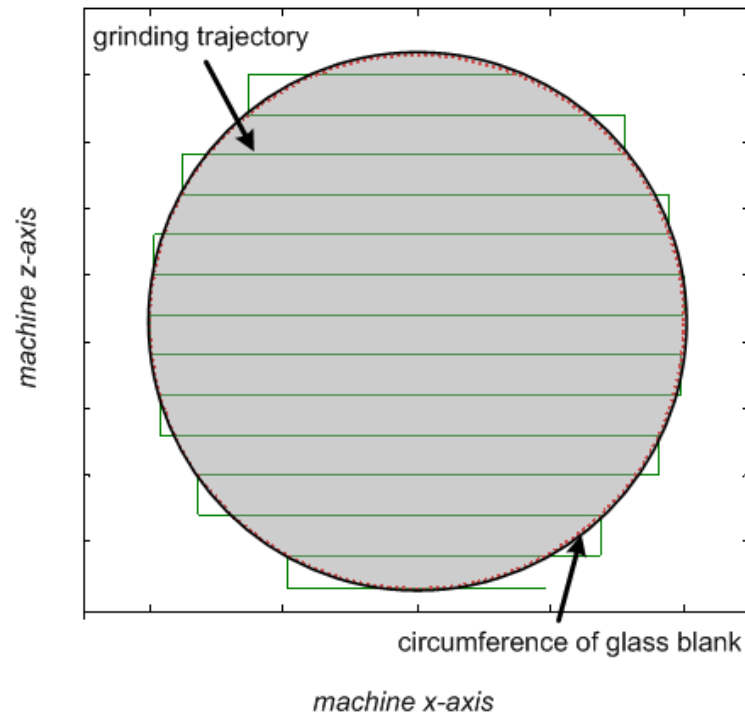
Figure 3.3: Locus of grinding wheel traverse along the BK7 glass blank for wheel wear experiments

3.3 Summary

In this chapter the experimental setup and procedure has been discussed. The setup consists of a NC machine tool and a power supply for electrolytic dressing, fitted with a system of sensors and signal recording instruments. The three different kinds of experiments have also been discussed. The next chapter discusses the first part of the research which is the study of the electrolyte.

Chapter 4

IMPEDANCE STUDIES OF

ELECTROLYTE

4.1 Introduction

The main objective of the thesis is to investigate and model wheel wear in ELID grinding. As discussed in Chapter 2, wheel wear occurs through a combination of electrochemical action (to form oxide from the metal bond), and reaction of grinding (which erodes the oxide). The dressing process uses the metal bond to produce the oxide layer, and the rate of production is controlled by the electrolytic current. This current depends on the applied potential and the mechanism of charge transfer in electrolysis. The rate of oxide formation is important for grinding performance, and this in turn, is directly related to dressing current. Hence, investigation of the factors affecting the current is important. These factors are (i) *electrolyte flow system*, and (ii) *existing oxide layer*. This chapter is dedicated to the study of the electrolyte flow system and how the charge flowing through it responds to applied potential.

More specifically, the target of the chapter is to answer some very definite questions, listed as follows:

i. *Relationship of current to applied voltage*: In electrolysis, relation between applied voltage and resulting current depends on many factors like

concentration gradient, diffusivity, degree of dissociation, conductivity of electrolyte etc. [67]. This exact relation between current and applied voltage has to be established to understand the behavior of electrolytic dressing.

ii. *Impedance of electrolyte*: Electrolyte impedance can be capacitive, inductive, resistive, or a combination of any of these. Response of electrolyte flow to square pulse voltage is explored to find the impedance function.

iii. *Effect of gas generation*: Gas generation rate at the cathode is a function of the dressing current. But the effect of gas generation on conductivity is unknown.

iv. *Variation of electrolyte behavior with flow conditions*: Grinding speed, inter-electrode gap and flow rate affect the flow dynamics of the electrolyte. Their effect on dressing current is to be ascertained.

These concerns are important for the theoretical development of electrochemical machining (ECM) [68-73], where electrolytic action is used to dissolve the anodic work metal with a shaped cathode, the trajectory and geometry of which gives the final shape to the work. ELID is similar in principle with ECM except for the deliberate presence of the oxide layer, and development of the later can be used as a pointer for the former.

4.2 Governing Principle of ELID

When electric current flows through the electrolyte, dissociation of water molecules and other compounds takes place. The anode goes into solution by forming metallic cations and the negative ions in solution bond with them to form the anodic oxide deposit. Transport of ions takes place through three mechanisms:

i. *migration* due to electrical potential difference between the electrodes,

ii. *diffusion* due to difference in concentration of ionic species between the electrodes,

iii. *convection* due to physical movement of the electrolyte.

The relationship between the applied voltage and current response in an electrolytic system established from these mechanisms can be obtained from Eqn. 4.1 [67].

$$V = \left(E_c - E_a\right) + \eta_a + \eta_{conc} + V_r + V_\Omega \qquad (4.1)$$

When two metals are in contact and in presence of an electrolyte, flow of charge takes place due to the different electrode potentials inherent in the metals. This natural potential difference is the reversible potential, $\left(E_c - E_a\right)$ of the electrolytic cell, where E_c is the electrode potential for the cathode and E_a for the anode. Activation overpotential, η_a, is the extra potential required to ionize the anode to discharge its ions for metal dissolution. Concentration overpotential, η_{conc}, is the potential formed due to the concentration gradient of ions formed near the electrode boundary. Since the electrolyte is in constant turbulence in ELID Grinding, this overpotential is absent, or negligible. The anodic oxide formed has a high resistance and causes a potential drop. This is the resistance overpotential, V_r, and is of major importance in ELID Grinding, though not in the present study where oxide has been scraped off. V_Ω is the Ohmic potential drop across the electrolyte and the potential applied by the external power supply is V.

The activation overpotential represents the amount of energy responsible for the dissociation of ions from the anode and cathode and is related to current density. The relation is explained by the Butler-Volmer Equation (Eqn. 4.2) [67].

$$i = i_0 \left[\exp\left(\frac{z\alpha\eta_a F}{RT} \right) - \exp\left(\frac{z(1-\alpha)\eta_a F}{RT} \right) \right] \qquad (4.2)$$

Here, i is current density, i_0 is exchange current density, z is the valency of metal ion, α is the fraction of overpotential associated with metal dissolution, F is the Faradays constant, R is the Gas constant and T is the temperature in absolute scale.

Since, in ELID, the cathode remains chemically unchanged and dissolution/oxide formation occurs only on the anode, the overpotential for cathode is negligible, and the Butler-Volmer Equation, reduces to the Tafel Equation (Eqn. 4.3) [67].

$$\eta_a = \left(\frac{2.303 RT}{z\alpha F} \right) \log \frac{i}{i_0} \qquad (4.3)$$

The Ohmic potential drop across the electrode gap is given by the Eqn. 4.4.

$$V_\Omega = i A_e R_e \qquad (4.4)$$

Here A is the area of the electrode surface, and R_e is the impedance offered by the electrolyte.

Combining Eqns.4.1, 4.3 and 4.4, the relationship between the current and applied voltage only due electrolyte can be obtained as shown in Eqn. 4.5.

$$V = \left(E_c - E_a \right) + \left(\frac{2.303 RT}{z\alpha F} \right) \log \frac{i}{i_0} + i A_e R_e \qquad (4.5)$$

Constants in Eqn. 5 can be evaluated from the materials used in the experiment. The oxidation-reduction potentials for the anode and cathode materials used, i.e. iron and copper respectively are E_a = - 0.44V (for Fe^{++}) and E_c = +0.34V. So, the reversible potential is $E_c - E_a$ = 0.78V

The constants required for the calculation of activation overpotential are, $R=8.3145$ J/K-mole, $T=296$ K, $F=96486$ coulomb/mole, $z=2$. The exact values of α and i_0 are

unknown. However, value of α varies from 0.2 to 2 [67] and value of exchange current density, i_0 for most practical cases is in the range 10^{-6} to 10^{-4} amp/cm^2 [67]. Maximum peak current encountered in the experiments is approximately 10 amp, which gives a maximum current density, i of 6.3662 amp/cm^2 with A_e=1.5708 cm^2. The maximum possible activation overpotential for this range of values can thus be obtained for lowest values of i_0 and α. Thus, the maximum activation overpotential, η_a that can be achieved is 0.9992 V (from Eqn. 4.3).

So, the potential, other than the Ohmic drop is $E_c - E_a + \eta_a = 1.78V$, which is negligibly small as compared to the peak voltage used in ELID power supplies (60 to 100V). The resulting dressing current is therefore approximated to be due to the Ohmic potential drop across the electrodes (Eqn. 4.6).

$$V = IR_e \hspace{6cm} (4.6)$$

where R_e is the impedance of electrolyte flow.

This can be verified experimentally if the ratio of applied voltage, V, to dressing current, I, obtained for different input voltages remains constant.

Experiments are conducted to obtain the resistance of the electrolyte from the current and voltage signals with the oxide removed from the grinding wheel surface. Figure 4.1 shows an even distribution of the ratio of voltage to current, V/I, obtained against the different voltages in support to the theoretical conclusion in Eqn. 4.6. The three data sets shown are for 250, 300 and 350 μm electrode gaps with grinding wheel speed of 7.8 m/sec at a flow rate of 1.8 l/min. So, it is proved that the electrolyte load system can be modeled by impedance, and now, the type of impedance has to be determined.
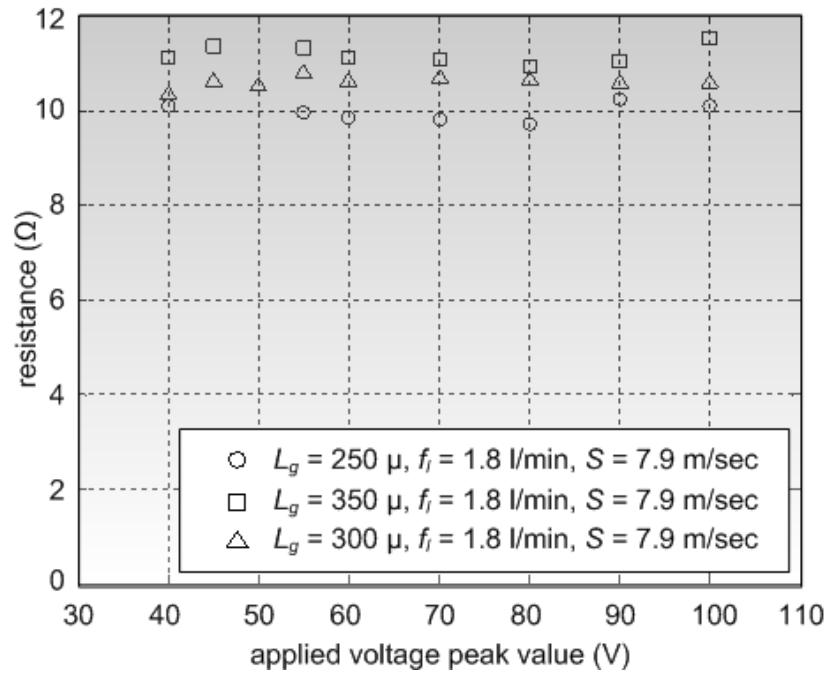
Figure 4.1: Resistance for changing input peak voltages

4.3 Impedance of Electrolyte
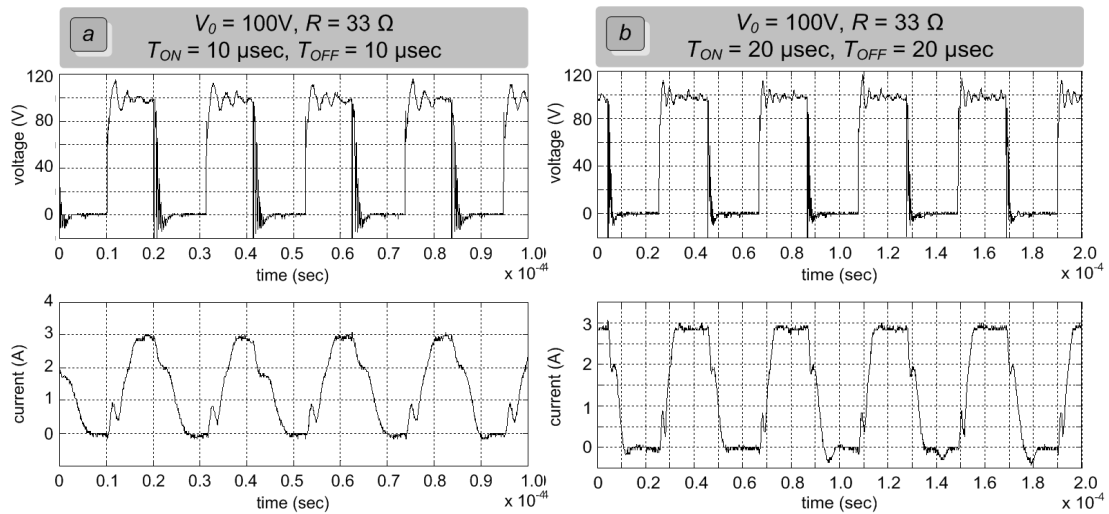
Figure 4.2: Voltage and current wave forms for resistive load of 33 Ω for (a) 10-10 μsec (b) 20-20 μsec pulse types

The type of electrolyte impedance i.e. whether it is resistive, capacitive, inductive or their combination, is investigated experimentally. The response to square pulse can provide this information. The experimental procedure is the same as in the last section. Input power source is a high voltage square pulse generator with variable voltage,

pulse ON time and OFF time. Before proceeding with the experiment, the power supply is evaluated by replacing the electrolytic load with a resistor of 33 Ω. The voltage and current characteristics obtained are shown in Figure 4.2 for pulse ON time and OFF times, T_{ON}-T_{OFF}, of 10-10 and 20-20 µsec. The current forms a trapezoidal wave, and the increase time, t_i, and decrease time, t_d, are both 6 µsec irrespective of the cycle time and duty ratio, d_r (Figure 4.3). A purely resistive load of the system should have produced current with an exact square pulse. Since the electrolytic load was replaced by a pure resistor, the reason for this kind of response must be due to stray inductance of the current path [74].
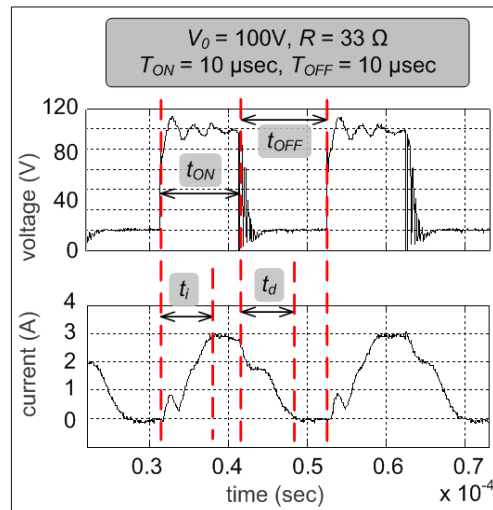
Figure 4.3: Voltage and current wave forms for electrolytic load

Electrolyte flow dynamics depend on the spindle speed, inter-electrode gap and flow rate. The gap is varied from 200 to 600 µ. Speed and flow rate are also varied but it is ensured that the gap is not deprived of electrolyte. Similar kind of wave form is obtained for the load due to electrolyte flow with t_i and t_d of 6 µsec irrespective of duty ratio, cycle time, electrolyte flow dynamics as shown in Figure 4.4 for different duty cycle and duty ratio. However, these dressing parameters change the peak value of the current. Naturally, for T_{ON} less than t_i of 6 µsec, the current wave form distorts to an approximate triangle before reaching the peak value so that the average dressing

current reduces, bringing down the peak voltage accordingly. Figure 4.5 shows such an instance of 5 µsec T_{ON} and T_{OFF}, where the applied 80V has reduced to approximately 40V, whereas Figure 4.4b shows the 70V peak for the same electrolyte load.
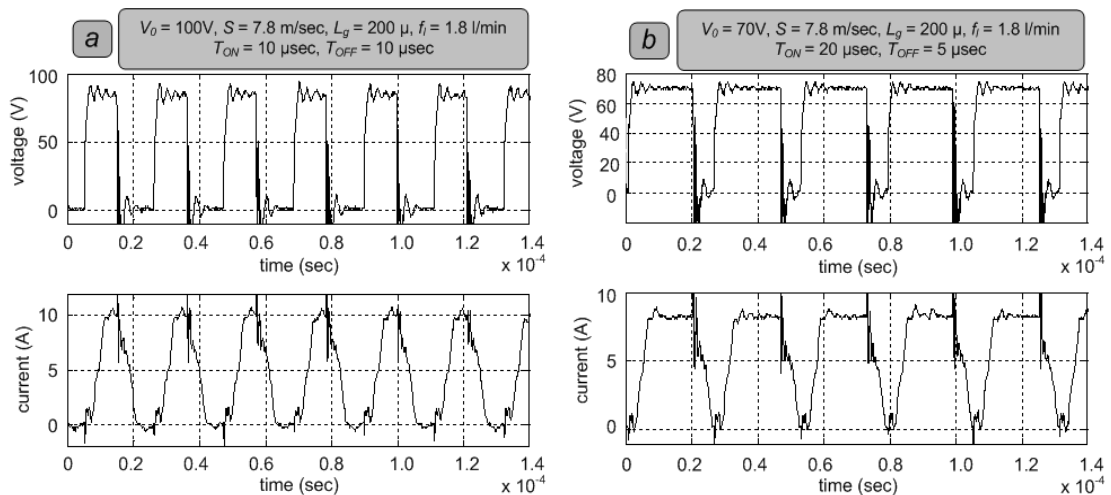
Figure 4.4: Voltage and current wave forms for dressing conditions (a) V_0=100V, T_{ON}=10 µsec, T_{OFF}=10 µsec, (b) V_0=70V, T_{ON}=20 µsec, T_{OFF}=5 µsec
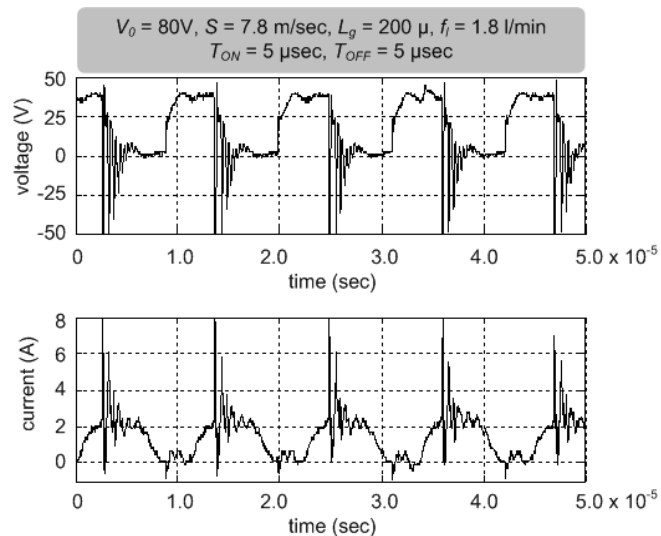
Figure 4.5: Voltage and current wave forms for 50% duty ratio and 10 µsec cycle time

It follows from Faraday's Laws of Electrolysis that the mass of oxide formation is directly proportional to the net charge. For a purely resistive load, the current response will also be square. Charge in the trapezoidal wave is approximately equal to that in a square pulse with the same peak voltage and ON time. So, oxide formation

41

should not be hampered by this distorted wave, and for such purposes, the net impedance due to the electrolysis can be assumed to purely resistive. This resistance will however change with the *grinding speed*, *inter-electrode gap* and *flow rate*.

4.4   Variation of Resistance with Flow Parameters

Now that the impedance of electrolyte is established to be resistive, its dependence on different flow conditions will be investigated. The electrolyte flows to the inter-electrode gap through an injecting cathode [46]. The general scheme of the flow volume is shown in Figure 4.6. The factors affecting the fluid flow are the rotation of the grinding wheel, S, the flow rate, f_l, and the inter-electrode gap, L_g, (Eqn. 4.7b) which in turn will determine the resistance, R_e, offered by it (Eqn. 4.7a). The resistivity, ρ_e, of the electrolyte will depend on all these variables.
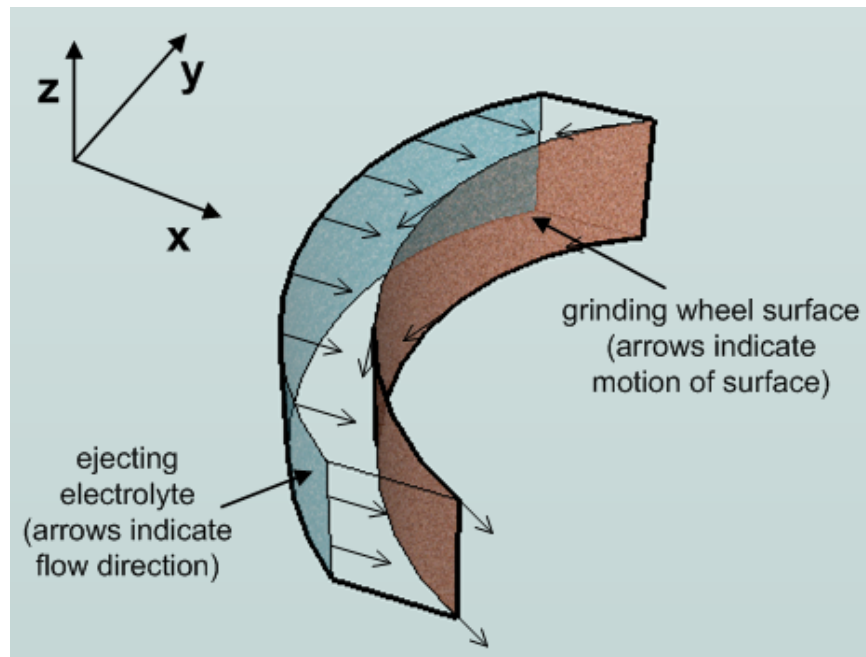
Figure 4.6: Simplified model for electrolyte flow within electrode

$$R_e = \rho_e \frac{L_g}{A_e} \qquad\qquad (4.7a)$$

$$\rho = f\left(S, f_l, L_g\right)$$

$$(4.7b)$$
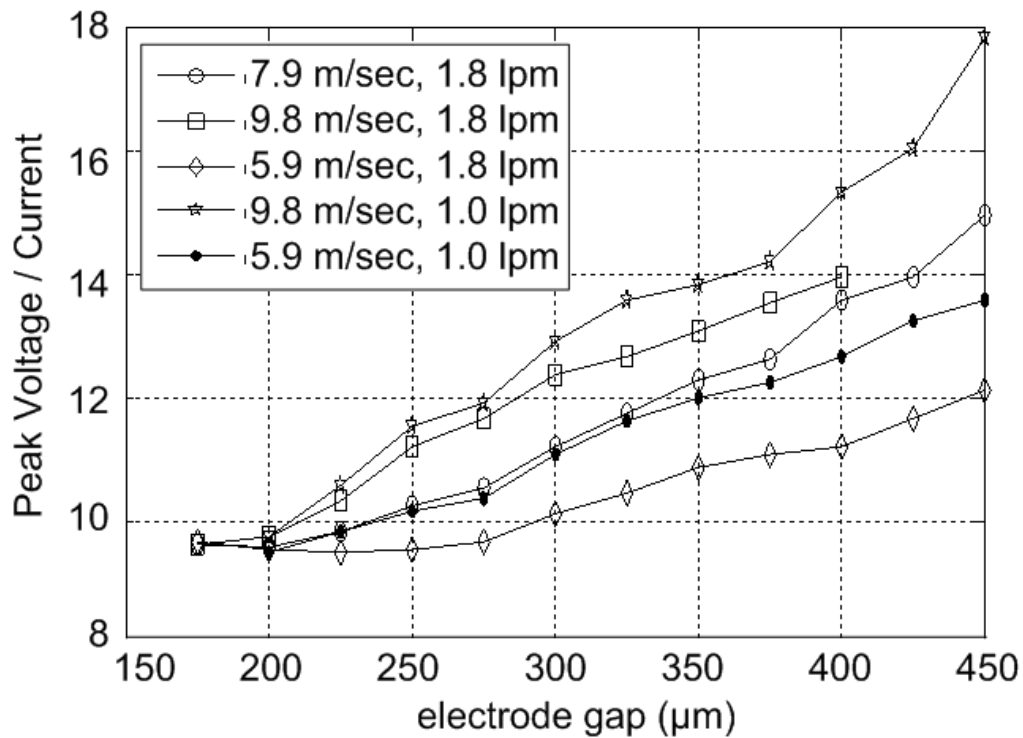
Figure 4.7: Change of electrolyte resistance with electrode gap, grinding speeds and flow rate

High velocity of fluid enhances ion movement and hence decreases electrical resistance. Experiments are conducted for measuring resistance for different flow conditions and the variation is shown in Figure 4.7. It can be seen that electrode gap is the most dominating factor followed by grinding speed. Large gap not only increases resistance due to length of charge flow path, but also loses more electrolyte owing to the unconfined flow volume. With lesser electrolyte reaching the anode from cathode, very high resistance changes take place. Increased flow rate keeps the electrode gap fully flooded and enhances current flow. High rotation speeds of the wheel causes churning of the fluid thereby increasing the flow turbulence and consequently its resistance. It should be noted that the resistance curves diverge from 200μ electrode gap with all the resistance values approximately same at that value. This is because,

smaller gaps produce sparking on the metal bond with no oxide present and the process mechanics change from electrochemical to electro-discharge (ED). So, ED-truing [54] will occur under low electrode gaps with the same applied voltage.
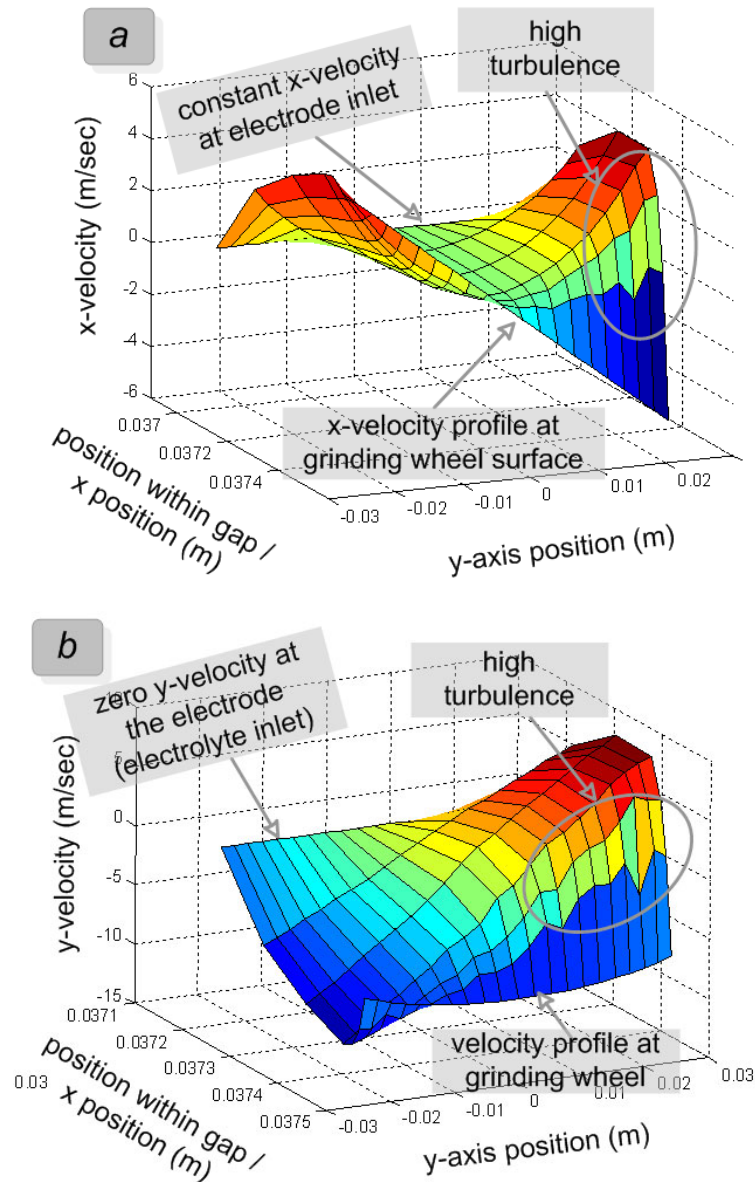
Figure 4.8: Velocity profile of electrolyte flow within the middle plane ($z = 0.0015$) of inter-electrode gap in the (a) x-direction and (b) y-direction respectively

The behavior of resistance change can also be explained by investigation of the flow condition in the inter-electrode gap. Average flow velocity of the electrolyte is obtained from preliminary CFD (computational fluid dynamics) analysis of turbulent flow where the control volume is modeled as per Figure 4.6. Electrolyte inlet is on the

concave surface of the control volume with outlet on the four plane sides. The concave surface of the control volume is the rotating wall. The Figure 4.8a and b show the velocity profile for the x and y components (co-ordinate system shown in Figure 4.6). The average velocity for different electrode gaps and wheel speeds is shown in Figure 4.9. Small gap produces high x-velocity that aids migration of ions and also reduces the flow length of charge thereby aiding dressing. The y-component of velocity increases with increasing speed and hinders the flow of ions from reaching the anode. So, increased spindle speed is not favorable for oxide formation.

4.5   Change in Resistance by Gas Generation
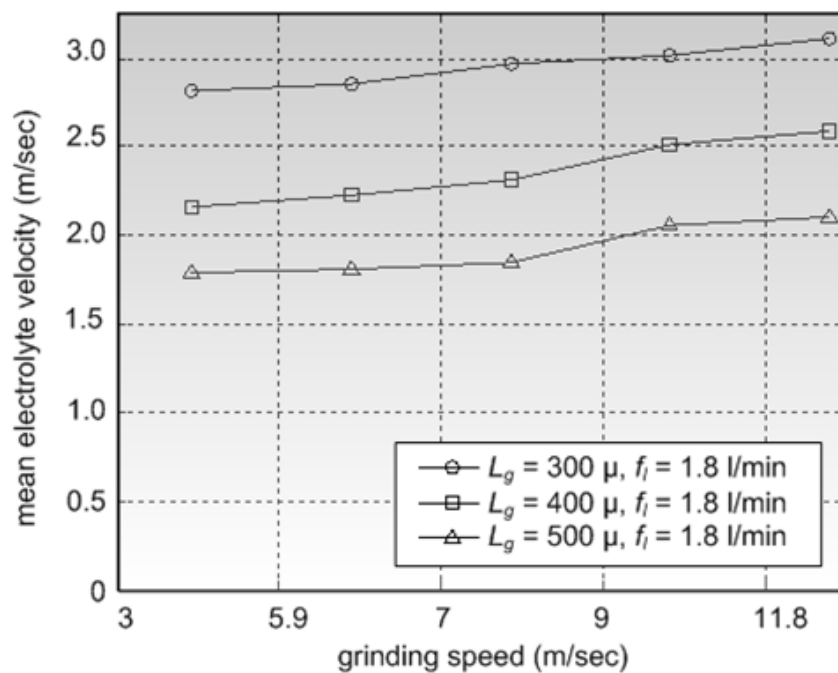
Figure 4.9: Average velocity of electrolyte for different electrode gaps and grinding speeds

Other than flow dynamics, hydrogen generation from the cathode surface, which depends on the current, also influences resistance of the electrolyte. Change in resistivity due to gas generation is obtained by Bruggeman's equation [67] (Eqn. 4.8a) which relates true resistivity of electrolyte ρ_e, resistivity with gas generation ρ_g and

the volume proportion of gas, β. β is obtained from Eqn. 4.8b. The rate of gas generation, $\dot{V}_g$ can be obtained from average current I_{avg}, using Faraday's Laws of Electrolysis (Eqn. 4.8c). The constant k_{vg} is the volume of hydrogen generated per unit charge and η_H is the current efficiency for hydrogen generation. Again, input voltage links current and resistance of electrolyte through Ohm's Law.

$$\rho_g = \rho_e (1-\beta)^{-3/2} \tag{4.8a}$$

$$\beta = \frac{\dot{V}_g}{\dot{V}_g + f_l} \tag{4.8b}$$

$$\dot{V}_g = \eta_H k_{vg} I_{avg} \tag{4.8c}$$
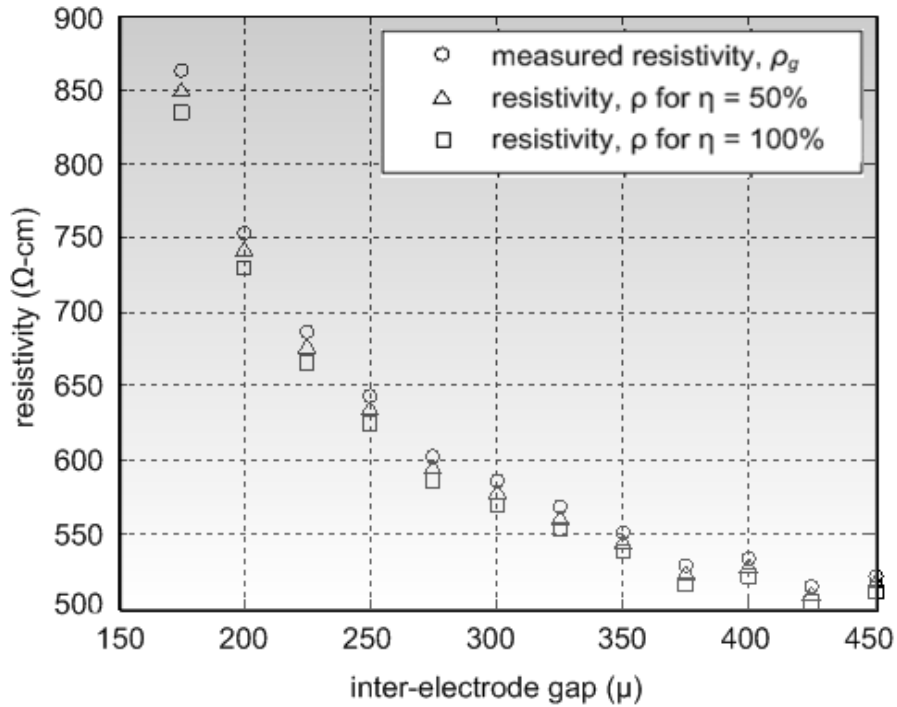
Figure 4.10: Comparison of resistivity with and without gas generation for resistance for grinding wheel speed of 7.9 m/sec and flow rate of 8 lpm

Electrolyte resistance for varying flow conditions was addressed in Section 4.4. This resistance was based on the resistivity (Eqn. 4.7a) with gas generation. Calculating the gas generation from the corresponding current, the actual resistivity is calculated.

Figure 4.10 shows the plot of resistivity with and without gas evolution. 50% and 100% η are used in the plot for comparing the amount of influence of gas generation. However, high η is not possible in ELID because, among other factors, much of the ionized electrolyte escapes before contact with anode due to the unrestrained electrode gap. There is a very marginal difference in the different resistivities, from where it can be concluded that the change in resistivity due to gas generation is marginal. This change can be significant if the flow rate of electrolyte becomes close to the value of gas generation (Eqns. 4.8a and 4.8b), i.e. if the electrolyte flow rate is starved.

4.6   Conclusions

The study is carried out to investigate some basic problems on electrical properties of electrolyte, common to researchers in ELID grinding. The findings are highlighted as follows.

- Voltage applied for electrolysis is equal to the sum of the overpotential and Ohmic potential. Overpotential in ELID is negligibly small compared to the high applied voltage.

- Gas generation during electrolysis can significantly affect the resistivity of the electrolyte but its effect is negligible in ELID, unless the electrolyte flow rate is deprived.

- Resistance decreases with decreasing electrode gap because the length traversed by the ions is smaller. Increasing grinding speed increases the turbulence and reduces the component of velocity responsible for ion transfer thereby increasing the resistance.

- Inter-electrode gap smaller than 200μ (approximately) with the metal bond of the wheel exposed lead to sparking. Electrolytic action occurs for higher gaps.

- Response of the electrolyte to square pulse voltage, irrespective of flow conditions (inter-electrode gap within 600μ and sufficiently flushed with electrolyte) and dressing parameters, is a trapezoidal wave formed due to inductance of current flow path and resistance of electrolyte. However, with pulse ON time less than the rise time, the current pulse becomes triangular thereby reducing the average current.

With these conclusions in place, the study of dressing characteristics can now be commenced.

Chapter 5

STUDIES OF

ELECTROLYTIC DRESSING

5.1 Introduction

ELID grinding produces lower grinding forces and generates high quality surface finish as compared to conventional grinding processes. The fundamental difference between ELID grinding and its conventional counterpart is the electrolytic dressing process. Electrolytic dressing, which forms the anodic oxide, is responsible for the lower forces and enhanced surface finish [18, 28, 29, 31, 58, 75-77]. The periodic variations of the grinding forces and current [29, 31] is also attributed to the presence of the oxide layer. So, study of the oxide layer formation process is critical to overall understanding of the ELID grinding process. Ideally, in ELID grinding, the oxide layer is formed during electrolysis and it wears off during grinding. Direct mechanical wear of the metal bond does not take place, and so, wheel wear is only through electrochemical action. Consequently, study of electrolytic dressing is indispensible for wheel wear studies as well.

Oxide formation rate is directly related to dressing current. Dressing current, on the other hand, is related to the existing oxide layer thickness. This relationship between oxide formation and dressing current has been formulated in this chapter.

5.2 Theory

5.2.1 Input and Output Variables

Dressing process in ELID is an electrochemical process which forms oxide at the expense of the metal bond and the electrolyte. Rate of dressing is determined by the magnitude of electrolytic current (aka dressing current), which in turn is controlled by the applied voltage and electrolyte impedance. The current value is also determined by the existing oxide layer thickness, but the dynamically changing layer thickness is again a function of the dressing current. So, the dressing process, for a given setup of grinding wheel and electrolyte combination, is governed by two input conditions, (i) electrical inputs of power supply viz. *voltage pulse type*, *peak voltage*, *cycle time* and *current duty ratio*, (ii) inputs determining flow conditions of electrolyte, viz. *spindle speed*, *electrolyte flow rate* and *inter-electrode gap*. Figure 2.1 shows the schematic representation of the grinding setup, where electrolytic oxidation takes place with a conjugate electrode (that also acts as an injector for the electrolyte), so that the oxide layer is formed on the periphery of the wheel.

The output of the dressing process is the *oxide layer (thickness)*, and its rate of change of volume is signified by the *dressing current*. Both, these quantities are the output variables of the process. The dressing current is easily measurable with a current sensor, but the layer formation, due to its electrical and mechanical properties is difficult to measure.

Moreover, oxide formation takes place by consuming the metal bond. Volume of particular type of oxide formed from the parent metal bears a constant ratio with the metal volume consumed, known as the *Pilling Bedworth Ratio* (PBR). So, electrolytic

metal bond dissolution is also a representative for oxide formation. The formulations of *metal dissolution* and *oxide layer formation* are both established in this chapter.

5.2.2 Governing Equations

5.2.2.1 Relation between Layer Thickness and Dressing Current

Metal dissolution or oxide formation during electrolytic reaction is related to the current by Faraday's Laws of Electrolysis (Eqn. 5.1). The rate of oxide formation per unit area of electrolyzed surface can be obtained from the rate of metal dissolution and its PBR, C_{PBR} (Eqn. 5.1b). This relates the amount of oxide formed with the density of the metal, s_m. The thickness of oxide layer, L, can also be directly obtained from current, I, by applying Faraday's Laws of Electrolysis, if the density of the constituent oxide, s_o is known [78] (Eqn. 5.1a).

$$\frac{dL}{dt} = \eta \frac{M_o}{zFA_e s_o} I \tag{5.1a}$$

$$\frac{dL}{dt} = \eta C_{PBR} \frac{M_m}{zFA_e s_m} I \tag{5.1b}$$

Here, M_m is the molecular weight of the metal ion, and M_o that of the oxide per oxygen ion, A_e is the electrode area, z is the valency of the metal ion, η is current efficiency and F is Faraday's constant.

5.2.2.2 Relation between Dressing Current and Applied Voltage

Current can be related to the input variables with the applied voltage and the governing equations of electrolysis. It is established, in Chapter 4, that overpotential for the electrolysis is negligible in ELID. So, the relation between applied voltage and current can be represented with an electrical circuit as shown in Figure 5.1. Moreover, the impedance of the electrolyte, R_e, (for electrode gap values used in ELID) is

resistive, as concluded in Chapter 4. The resistance to current flow is offered by the electrolyte and the existing oxide layer, R_a, and the internal resistance of the power supply, R_i. So, Eqn. 5.2 relates current with applied voltage and existing resistances.

$$(V_0 - U)d_r = (R_i + R_e + R_a)I \qquad (5.2)$$

Here, V_0 is the peak voltage of the applied potential, U is the overpotential, and d_r is the current duty ratio of the applied potential.
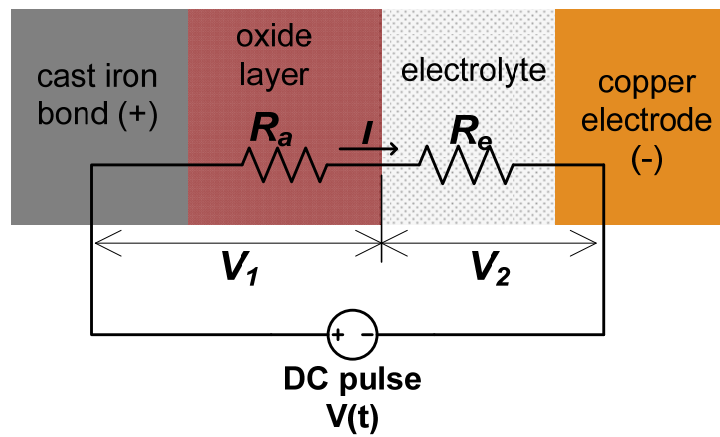
Figure 5.1: Representation of electrolytic dressing system as an electrical circuit

The value of the resistance for electrolyte flow conditions, R_e, is already determined in Figure 4.7. Resistance of oxide layer, R_a, is related to its thickness through Eqn. 5.3.

$$R_a = \rho \frac{L}{A_e} \qquad (5.3)$$

Relation of resistance of the electrolyte flow with spindle speed, inter-electrode gap and electrolyte flow rate is determined experimentally in Section 4.4.

5.2.2.3 Formulation for Charge Density

The Eqns. 5.1a, 5.2 and 5.3 can be combined to form the governing equation of the dressing process (Eqn. 5.4), which relates the outputs of dressing current and oxide layer thickness with the inputs of:

i. power supply, through V_0 and d_r

ii. electrolyte flow system, through R_e.

$$(V_0 - U)d_r = \left(R_i + R_e + \eta\rho \frac{Mq}{zFs_o A_e} \right) \frac{dq}{dt} A_e \qquad (5.4a)$$

Solution of this equation requires the values of the density of oxide layer, which is not generally known. But the PBR of oxide is commonly available in erosion handbooks. In such a situation, the governing equation for dressing can also be obtained by combining Eqns. 5.1b, 5.2 and 5.3, by using the density of the bond material.

$$(V_0 - U)d_r = \left(R_i + R_e + \eta\rho C_{PBR} \frac{Mq}{zFs_m A_e} \right) \frac{dq}{dt} A_e \qquad (5.4b)$$

5.2.2.4   Relation between Layer Thickness and Growth of Wheel

The insulating oxide layer thickness forms by consuming the metal bond and the electrolyte (Figure 5.2), and the volume of the oxide is greater than the volume of metal bond it consumes. Consequently, oxide formation, without its erosion, increases the radius of the wheel. This *increase in radius*, L_a, (also referred to as *wheel growth*) is a measurable quantity, but not the actual thickness of the layer. So, its relation to the required oxide layer thickness, L, has to be determined.
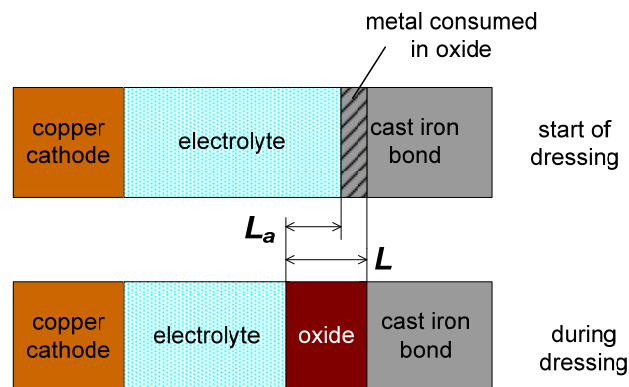
Figure 5.2: Schematic showing oxide forms by consuming bond metal and grows in the direction of the gap as well as the bond metal

A new coefficient c is defined as the ratio of L to L_a, (Eqn. 5.5a) which is related to PBR (Eqn. 5.5b). L_a can be found directly from c and L.

$$c = \frac{L}{L_a} \quad\quad (5.5a)$$

$$C_{PBR} = \frac{c}{c-1} \quad\quad (5.5b)$$

Mass of oxide formed and the mass of metal consumed by the oxide are related to the molecular weights of the constituents. Relation between L and L_a can also be obtained from the relation between their volumes (Eqn. 5.6a). So, when the density of the oxide is known, and the PBR is unknown, the value of the coefficient c can be found using Eqn. 5.6b (obtained by rearranging Eqn. 5.6a).

$$\frac{(L - L_a)s_m}{Ls_o} = \frac{M_m}{M_o} \qu\quad (5.6a)$$

$$c = \frac{s_m \dfrac{M_o}{M_m}}{s_m \dfrac{M_o}{M_m} - s_o} \qu\quad (5.6b)$$

5.2.2.5 Time Variable

The equations discussed so far can obtain oxide layer thickness and dressing current from the *resistance of the electrolyte flow system*, R_e, and the *power supply inputs*, V_0 and d_r. The *growth of the wheel radius*, L_a can also be found. However, solution of the dressing problem also needs the time variable. Wheel speed and total dressing time control the net time of electrolysis. The surface which is electrolyzed is continuously changing because of wheel rotation. So the spindle speed also plays a part in determining the duration of electrolysis. The sector of electrolysis is 90° *i.e.* the angle of the wheel segment covered by the cathode. Here every point on the wheel

undergoes electrolysis for $(90/360) \times 60/S$ sec per wheel rotation, where S is the rpm of wheel. For a total dressing time of T_0 sec, there will be $T_0 \times S/60$ rotations. So, the time of electrolysis for every point on the wheel in a total dressing time of T_0 is $T_0 \times 90/360$ sec.

5.2.2.6　Solution of Equations

The oxide layer thickness can be obtained in two approaches; (i) finding the oxide layer formation rate directly from the dressing current (Eqn. 5.1a); (ii) finding the metal bond dissolution from the dressing current and then multiplying it with PBR to get the oxide layer thickness. Both approaches are discussed below.

i. The differential equation 5.4a is solved to find the charge density, from which the dressing current is obtained. The oxide layer thickness is found with the dressing current and Eqn. 5.1a. The coefficient c is obtained from Eqn. 5.6b with the help of which wheel growth is found from Eqn. 5.5a. The density of the oxide has to be known for this approach of equation solution.

ii. When PBR and density of the metal bond are known, Eqn. 5.4b is solved to find the charge density. The current is obtained, from which the oxide layer thickness is found with Eqn. 5.1b. PBR being known, the wheel growth is then obtained from Eqn. 5.5a. This approach directly finds the metal bond dissolution which will be helpful in wheel wear studies. So, it is used for solving the equations and simulating dressing current and wheel growth.

The set of equations, described so far, consists of several unknown coefficients, the most critical among which are the density of oxide, s_o, its resistivity, ρ, c and η. Others can be obtained from the material specifications of the electrolytic system used. Solution of the equations for representative values of s_o, ρ, c and η is shown in Figure

5.3, which can be tallied with experimental results. The experimental setup and procedures are described in Chapter 3.
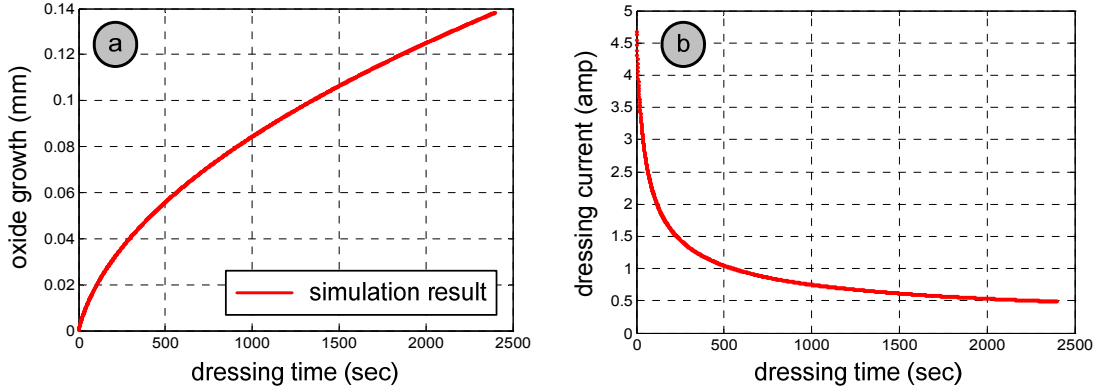
Figure 5.3: Solution of the equations to obtain (a) wheel growth and (b) dressing current for $\eta=25\%$, $c=40$, $\rho=1000$ Ω-cm, $R_e=9.5\Omega$

5.3 Experimental Growth of Oxide Layer

The experimental results show that the change in wheel radius has an increasing (Figure 5.4a), and dressing current has a decreasing trend (Figure 5.4b) with time. When electrolysis starts, there is no oxide layer, and resistance to current flow is only due to electrolyte. Oxide nucleates at favorable sites on the wheel surface. Owing to the electrically insulating property of the oxide layer, its growth increases resistance to charge flow, thereby reducing the current. Reduction in current further decreases the formation rate of oxide and the cycle continues.

Judging by the plots of current and wheel growth (Figure 5.4b and 5.4a), dressing can be divided into two different phases of oxide formation, the *initial phase* and the *post-initial phase*. The initial phase is for the first 5 to 7 minutes of dressing, when the oxide is formed due to a very fast reaction [79]. Figure 5.4c shows the change in charge with dressing time and emphasizes that in spite of the two phases of oxide development, charge flows uniformly. Eqn. 5.1a shows that charge and oxide layer

thickness are proportional. Yet, a plot of ratio of L_a to charge Q (Figure 5.4d) i.e. the proportionality coefficient shows a decreasing trend with time, and not a constant value. This shows that the proportionality coefficient also varies with time and so the process has some other variables, which will be discussed in Section 5.4.
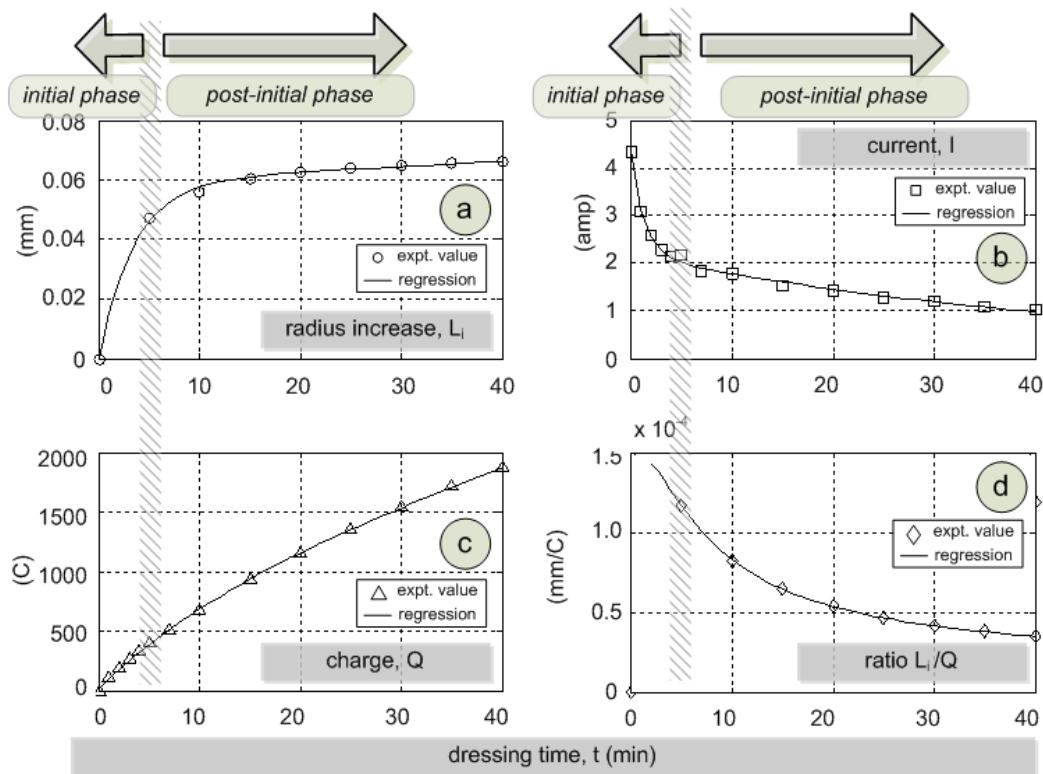
Figure 5.4: Experimentally obtained characteristics of (a) oxide layer formation, (b) dressing current, (c) dressing charge, and (d) ratio of wheel growth to dressing charge

5.4   Properties of Oxide Layer

During the initial phase the oxide grows rapidly to cover all exposed metal surfaces, until the entire metallic surface is covered by the oxide layer deposit (Figure 5.5). In this phase, nucleation of oxide begins at sites on the metal bond and the layer grows at low density so that the volume ratio of oxide formed to metal consumed is high. After the initial phase, oxide nucleates among pre-existing oxide. Poor cohesion between oxide particles makes the layer mechanically weak during this stage of development.
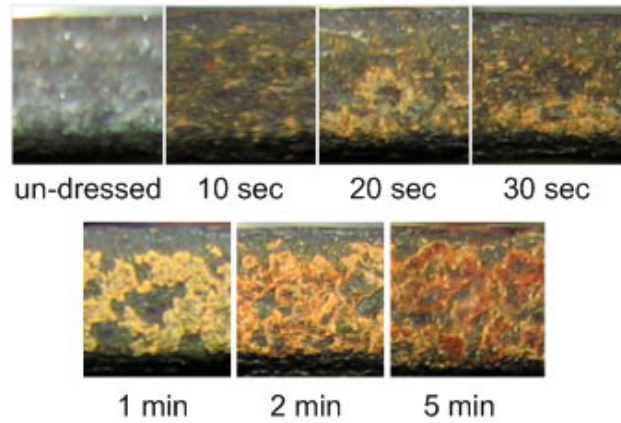
Figure 5.5: Stages of oxide formation on the grinding wheel surface (#325, square pulse, 100V, CG7 electrolyte)

The nature of the weak superficial layer of oxide is investigated with a copper cathode and stationary grinding wheel as anode, immersed in a tray of electrolyte (Figure 5.6a). Oxide is seen to float up with the gas bubbles generated from cathode even when the electrolyte is static (Figure 5.6b). This proves the fragility of the oxide formed. This loss of oxide produces low efficiency in the electrolytic reaction. Nucleation of oxide on the wheel after dressing can also be clearly seen in Figure 5.6c, which is also tested to be of very weak mechanical strength. When opposed by the dynamic forces of the flowing electrolyte, the oxide cannot grow freely beyond a certain thickness which is stably generated during the initial phase of dressing.
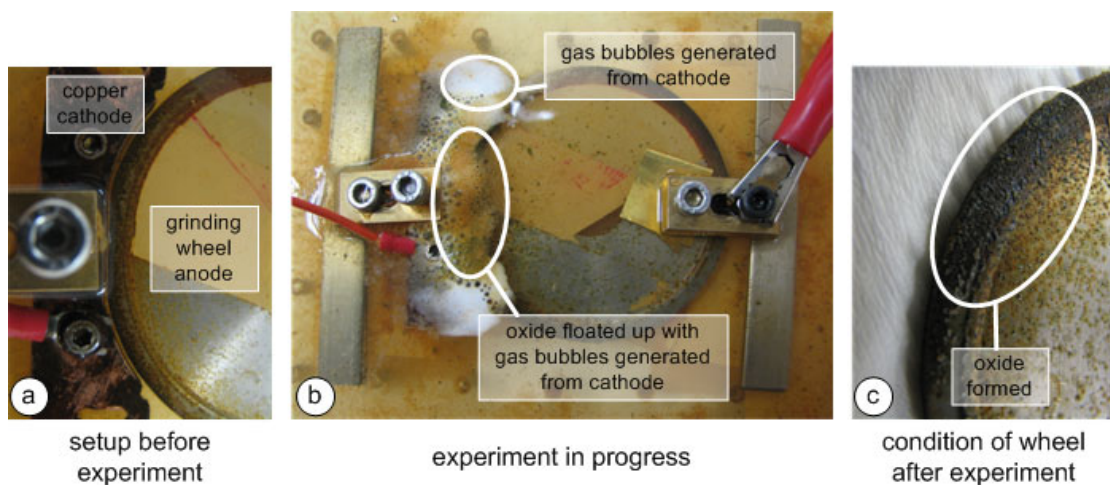
Figure 5.6: Electrolytic dressing carried out in static condition to investigate the fundamental nature of oxide formation
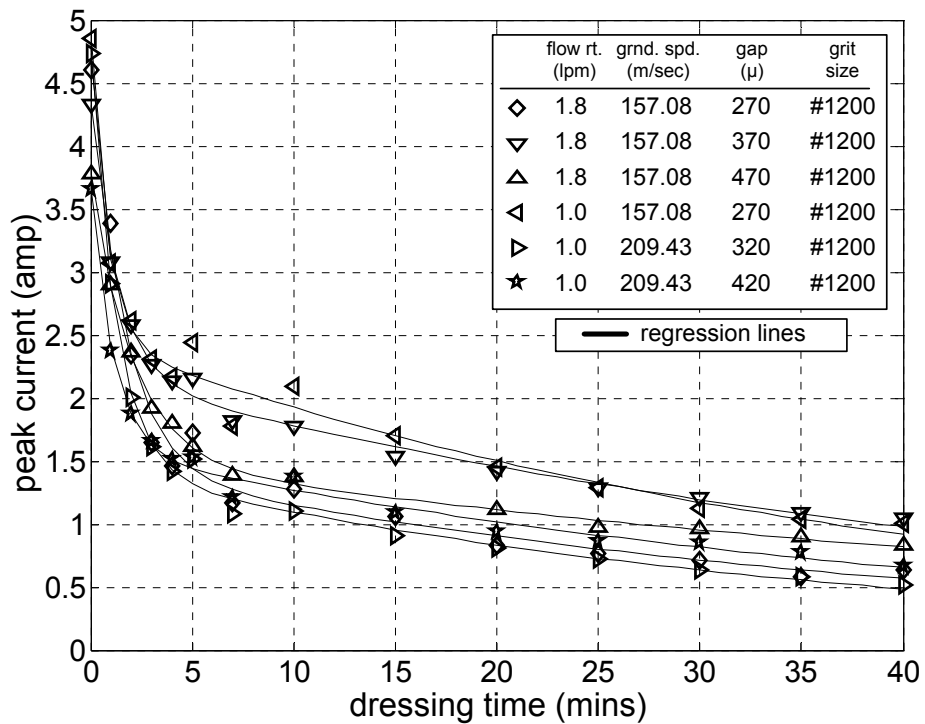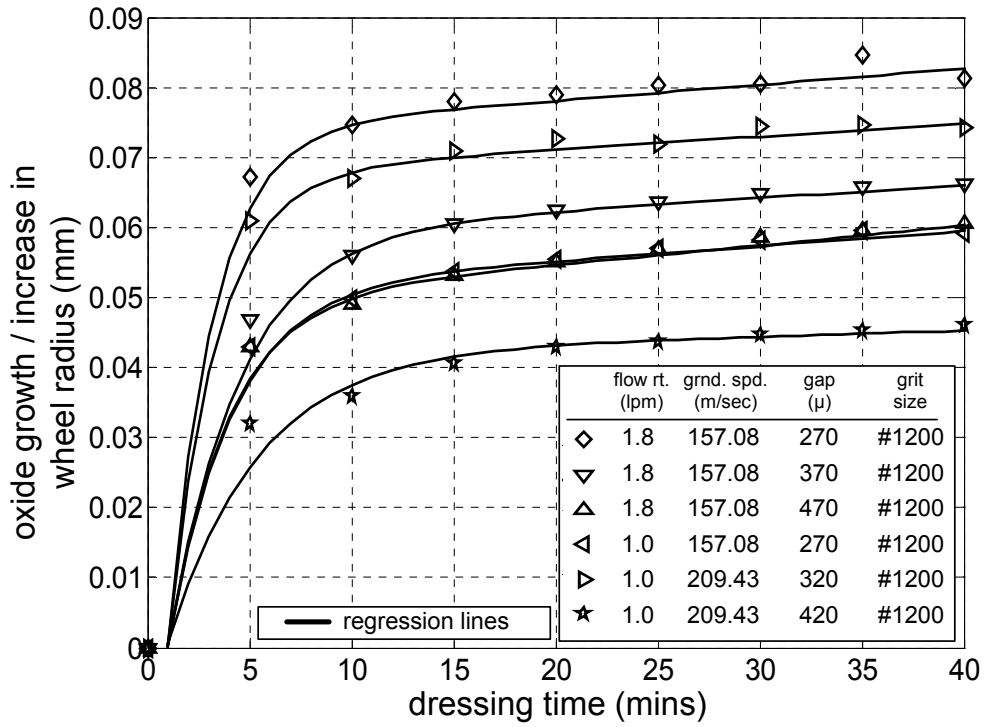
Figure 5.7: (a) Oxide layer formation and (b) dressing current characteristics for various dressing conditions

Input parameters, like electrolyte flow conditions and power supply settings affect oxide formation rate, because each of the parameters affects the current flow: small electrode gap enhances current flow by reducing length of charge flow path; low

electrolyte flow rate starves the path of charge flow; and high spindle speed increases turbulence increasing flow resistance. In the theoretical equations formulated, R_e, d_r and V_0 are the control variables for current and layer formation. However, experimental results suggest that for different values of flow conditions, wheel growth and dressing current do not bear a definite relationship, and is rather stochastic, as shown in Figure 5.7. This is because oxide formation in the post-initial phase is uneven and variation of oxide formation with process inputs cannot be observed experimentally. So, there must be other factors that contribute to the stochastic nature.

The poor mechanical strength of the oxide layer is responsible for erratic wear (friable nature of oxide reported by Bifano [33]) and affects the overall dressing process performance. Factors like surface roughness, impurity and electrolyte also have an important role on the oxide layer formation. They influence the electrolytic reaction in microscopic sites, and the combination of the microscopic phenomenon produce the net macroscopic behavior of dressing [33].
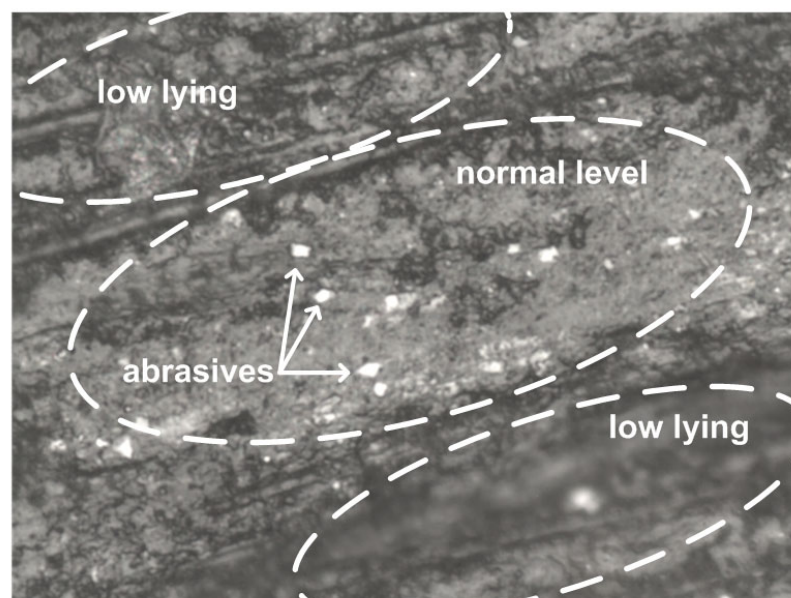
Figure 5.8: Microscopic image of #1200 wheel topography, with oxide layer scrapped off, at 1000x showing surface undulations and abrasives

As an example of the sensitive behavior of electrolytic dressing, minor scratches on passive electrode change the current significantly [80]. Internal stresses also develop in oxide films [81] which can give way under forces due to turbulent flow of electrolyte and produce unpredictable wear. Charge density depends on the surface roughness, with higher charge at the peaks and lower charge at the valleys, and affects oxide formation. It also depends on the presence of insulating chips of the grinding stone or the work material sticking to the wheel surface. If the wheel topography area has a higher density of low-lying regions below the normal level, most of the oxide will be formed in the low area and the measured oxide formation will show a lesser value. Type of topography typical to a grinding wheel without any oxide is shown in Figure 5.8. Charge distribution is also higher at the edge of the abrasives (being insulators) [65, 66]. The electrolyte changes oxide formation over time because it becomes impure with grinding chips, worn wheel, other debris and with aging. These uncontrollable factors occur in a micro-scale so that the process loses uniformity [33], and renders the dressing process partially uncontrollable, specially in the post-initial phase of dressing.

5.5   Validity of Theory

Comparison of experimental with theoretical results shows that the simulated dressing current pattern matches with the experimental current (Figure 5.9). The theoretical and actual increase in wheel radius only matches for the initial phase of dressing. Poor mechanical strength of the oxide in the post-initial phase leads to excess wear and leads to the mismatch of the theoretical and experimental wheel growth curves. Simulated current matches with experimental results. Comparison of the grinding wheel surface during grinding and during pre-dressing is shown in Figure 5.10. It can

be seen that the wheel surface during the first minute of dressing appears similar to the in-process dressed wheel. Mechanical action of grinding continuously wears off the excess oxide from the wheel and only the mechanically strong oxide is retained. The theoretical results match with the experimental values during the initial phase of the process, i.e. when the oxide is mechanically strong. So, this theory is used later in the thesis to simulate the overall ELID grinding process.
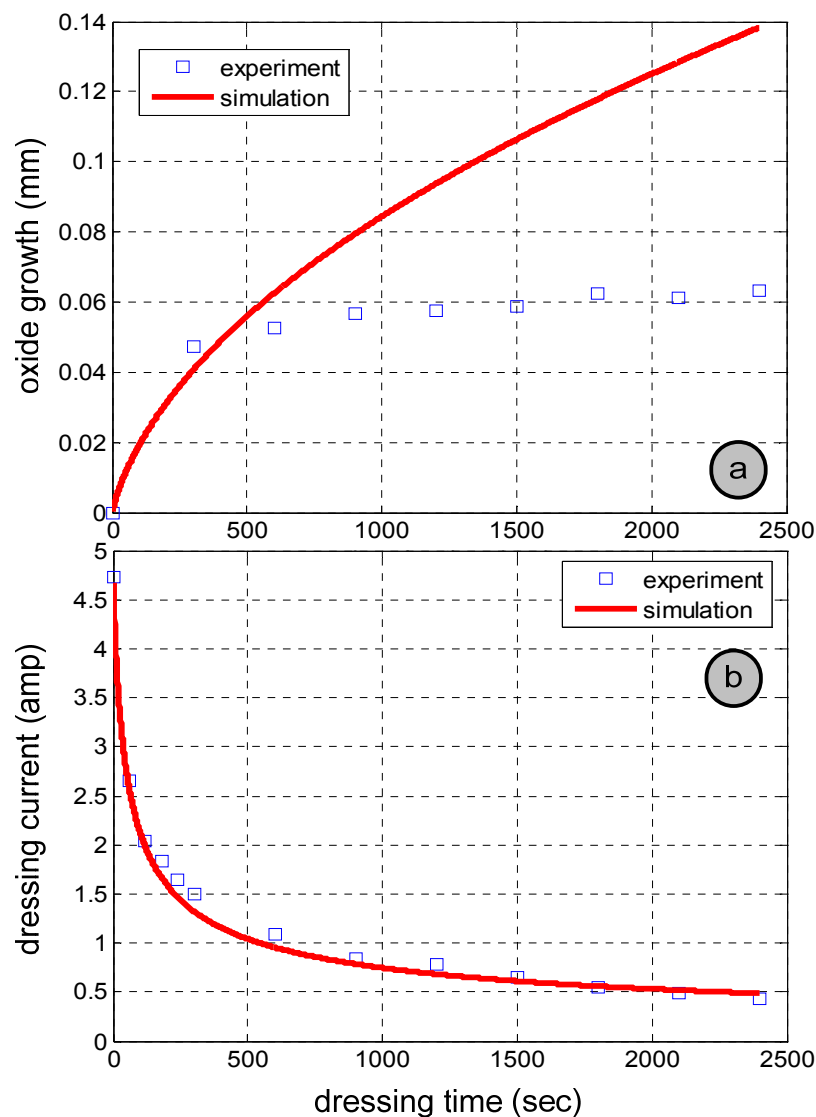
Figure 5.9: Comparison of the simulated values of (a) wheel growth and (b) dressing current with experimental values
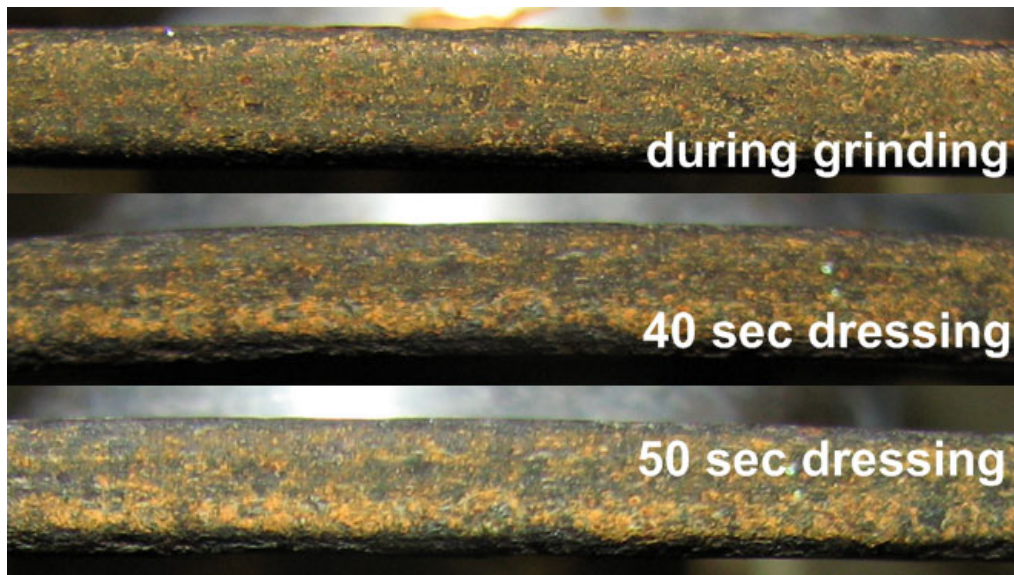
Figure 5.10: Comparison of #325 grinding wheel surface during the first minute of pre-dressing and during in-process dressing

5.6　Summary

In this chapter, the electrolytic dressing operation is investigated. Variation of current and oxide layer thickness during electrolytic dressing operation is examined theoretically and experimentally. The following are the conclusions for this part.

i.　Experiments are performed to find the change in layer formation and dressing current with respect to different input parameters. Initial phase of dressing i.e. during the first 5 to 7 minutes, the wheel growth is very drastic followed by a post-initial phase of slow growth rate.

ii.　Experimental results suggest that variation of dressing curves with input parameters of electrolyte flow system and power supply settings are stochastic due to the effect of several uncontrollable parameters.

iii.　Theoretical equations for oxide layer formation and dressing current are formulated.

In the next chapter, experiments are carried out to investigate the variation of wheel wear with ELID grinding conditions. The mechanism of ELID grinding is also investigated.

Chapter 6

EXPERIMENTAL ANALYSIS OF WHEEL WEAR

6.1 Introduction

Electrochemical action in ELID is reported in Chapters 4 and 5 of the thesis. The studies on wheel wear are discussed in detail in this chapter. Recapitulating the literature survey, wheel wear studies on ELID grinding was first reported by Fathima [31], where the wear mechanism of oxide erosion was discussed. Study of wheel wear as a quantitative function of grinding and dressing parameters has not yet been reported. Lim concluded that the grinding forces and dressing current varied periodically. These changes in force and current were produced by unstable wear of the grinding wheel and points to the unpredictability of wheel wear. Fathima [31] concluded the wear mechanism of the oxide matrix to be macro fracture, which also points to uncertain wear phenomenon. In the previous chapter, it was concluded that several uncontrollable parameters affect the dressing process and so oxide layer properties cannot be ascertained with certainty, as also pointed by Bifano [33]. The uncertainties of the dressing process, coupled with the stochastic nature of grinding [82] makes wear studies challenging.

It is observed in this study that the oxide layer thickness is in the range of 30 to 60μ after pre-dressing operation. A thinner oxide layer has smaller fractures resulting in

narrower margin of unpredictability. Moreover, first 5 mins of dressing is seen to be in accordance with the theoretical formulation and directs towards possible correlation of dressing with input parameters. So, contrary to popular trends (reports of wheel wear on ELID is absent except the one by Fathima [31]), it is worth investigating wheel wear as a function of the input parameters and attempt to achieve better profile accuracy of ground components by understanding first principles.

Wheel wear in ELID is a combination of mechanical and electrochemical actions. Oxide formed during electrochemical reaction is worn off by the mechanical action. Electrochemical reaction depends on the electrolytic current, which in turn depends on the existing oxide layer thickness. Higher mechanical wear of the layer will produce a thin layer of oxide, which will produce high current and result in high electrochemical action. The current is not only controlled by the resistance of the oxide layer, but also by the peak voltage and duty ratio of the voltage pulse. Rate of mechanical action will also vary with the amount of chips sticking to the wheel (wheel loading) and the hardness of the existing oxide layer. The bottom line, for an ideal ELID grinding process, is that actual metal bond wear occurs by electrochemical metal dissolution which forms the oxide. The mechanical action is merely responsible for erosion of the layer.

Investigations on both, brittle mode (with mesh size #325) and ductile mode (size #1200) grinding with ELID are carried out. The grinding forces, dressing current and wheel wear are measured, as explained in chapter 3. This chapter addresses the following aspects of ELID grinding, (i) predictability of wheel wear as a function of the input parameters, (ii) choice of dressing conditions for a particular set of grinding conditions, (iii) BK7 glass work surface characterization for #1200 CIB-SD wheel.

wheel speed 5.89 m/sec; feed 320 mm/min; infeed 3 μ
peak voltage 100 V; cycle time 20 μ-sec; duty ratio 90%
electrode gap 250 μ; grit size #1200
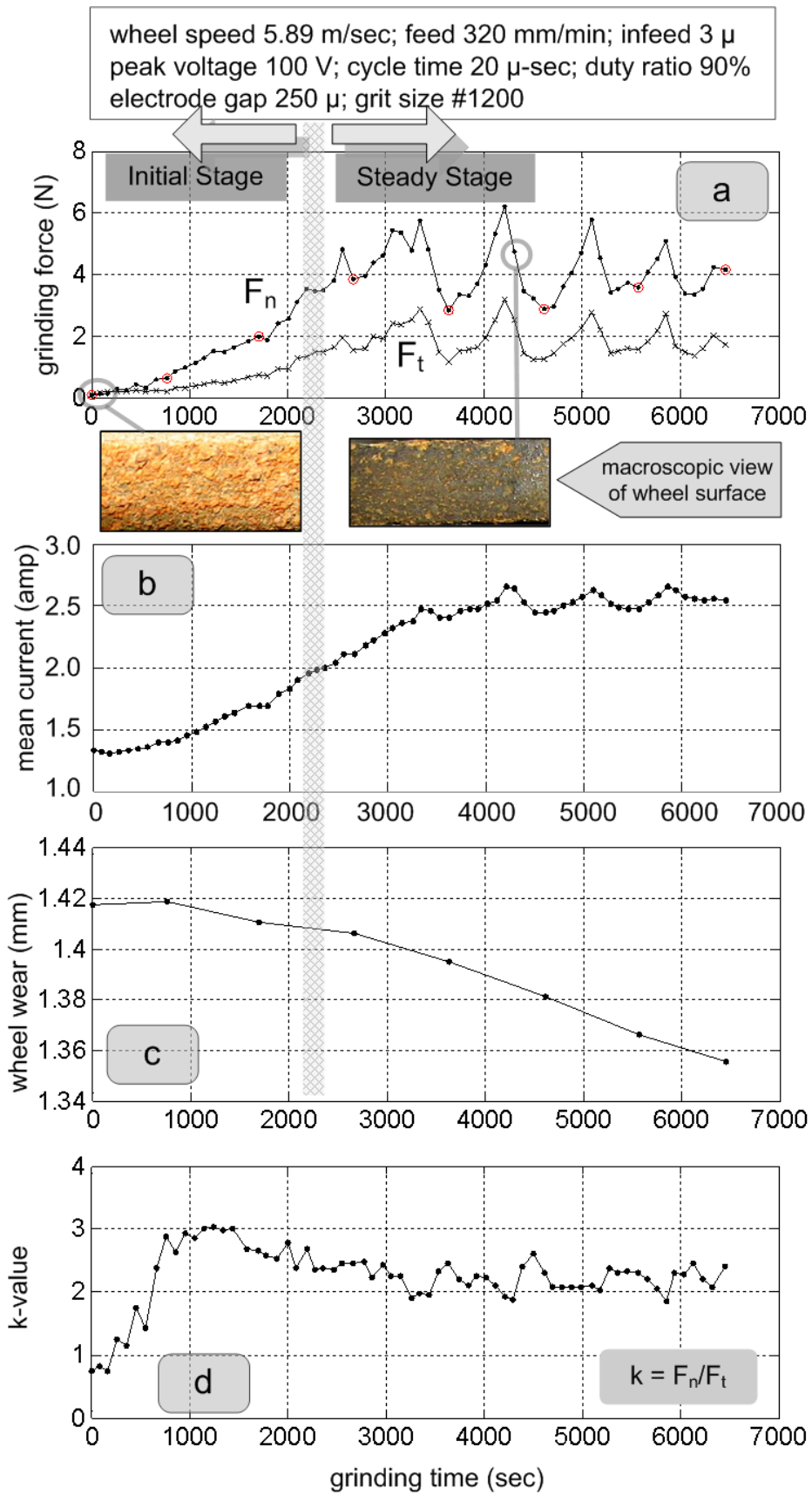
Figure 6.1: Grinding characteristics (a) normal and tangential forces, (b) dressing current, (c) wheel wear, (d) k-value

6.2 Experimental Results and Discussions

6.2.1 Mechanism of ELID Grinding

The experiments are carried out by #1200 abrasive size wheel, with grinding speed in the range of 4.9 to 9.8 m/sec, feed rate of 200 to 1200 mm/min and depth-of-cut from 2 to 4μ. Ductile regime material removal is observed on ground surfaces generated Characterization of the ground surfaces with grinding parameters are discussed in later sections and the mechanism of the process is first investigated.

A thick layer of oxide is formed after pre-dressing. The oxide layer is responsible for the non-uniform wear behavior because of its friable nature [33]. Changes in grinding force, dressing current and wheel wear during ELID grinding are shown for a representative experiment in Figure 6.1 which can be used to characterize the process. Based on the results, the ELID process can be distinguished into the initial and the steady stages (Figure 6.1). In the initial or transient stage, the effect of the thick pre-dressed oxide layer is present and it is worn off gradually. Grinding force increases with reduction of its thickness because the oxide layer is firmer towards the metal-oxide interface. Current also increases because the decreasing thickness reduces electrical resistance. But high current increases dressing rate, and a situation is reached when oxide formation competes with mechanical wear rate of oxide. This is when the steady stage of ELID grinding starts.

The steady stage is characterized by periodic rise and fall of the grinding forces (tangential and normal) in-phase with the dressing current within particular upper and lower limits (Figure 6.1a and b). The absence of the pre-dressed layer has formed a thin layer of oxide in this stage. Continuous grinding further reduces the layer thickness, and results in partial wheel loading. Thus oxide erosion rate reduces and

grinding forces increase. Reducing oxide thickness also causes the dressing current to rise along with the grinding forces such that the signals rise simultaneously in-phase. The situation reverses when higher oxide is generated than is worn off. Increased thickness eliminates wheel loading thus reducing grinding forces. Dressing current also lowers due to the presence of thicker oxide. Again, the wear of the oxide layer makes it thin and partial wheel loading sets in and is marked by the off-peaks of current produced in-phase with grinding forces. This rise and fall of grinding forces and dressing current repeat in cycles within specific upper and lower limit values. Average force and current are approximately constant over each cycle and so this stage of ELID grinding is referred as the *steady stage*.

Wheel loading is identified by the ratio of the normal to tangential force, popularly known as the k-value, which is within a particular limit for this stage (Figure 6.1d). Consequently, partial wheel loading, to cause inefficient grinding, is not an issue for the experiments.

The conditions of the oxide layer during the two stages of grinding are shown in insets of Figure 6.1. The oxide layer is considerably thin in the steady region, and unlike the pre-dressed layer, this layer is more stable and consistent (even though its thickness varies periodically) because it is reinforced with the asperities/undulations of the metal bond and the active grits. Also, the amount of oxide erosion and oxide formation are in equilibrium. So, the layer during steady grinding is more predictable. Comparison of wheel wear can therefore be possible for this steady-state grinding stage.

6.2.2   Empirical Relations

One of the foremost concerns of ELID grinding is its wheel wear estimation. Wheel wear rate (WWR), w_r, is determined by the ELID grinding parameters, wheel type, machine stiffness, work material, electrolyte, etc. The dependence on the ELID grinding parameters of grinding speed (wheel speed), S, feed rate, f_r, depth-of-cut, d_c and current duty ratio, d_r are investigated in this study. A benchmark function of these parameters is required to quantify their net effect on wheel wear.
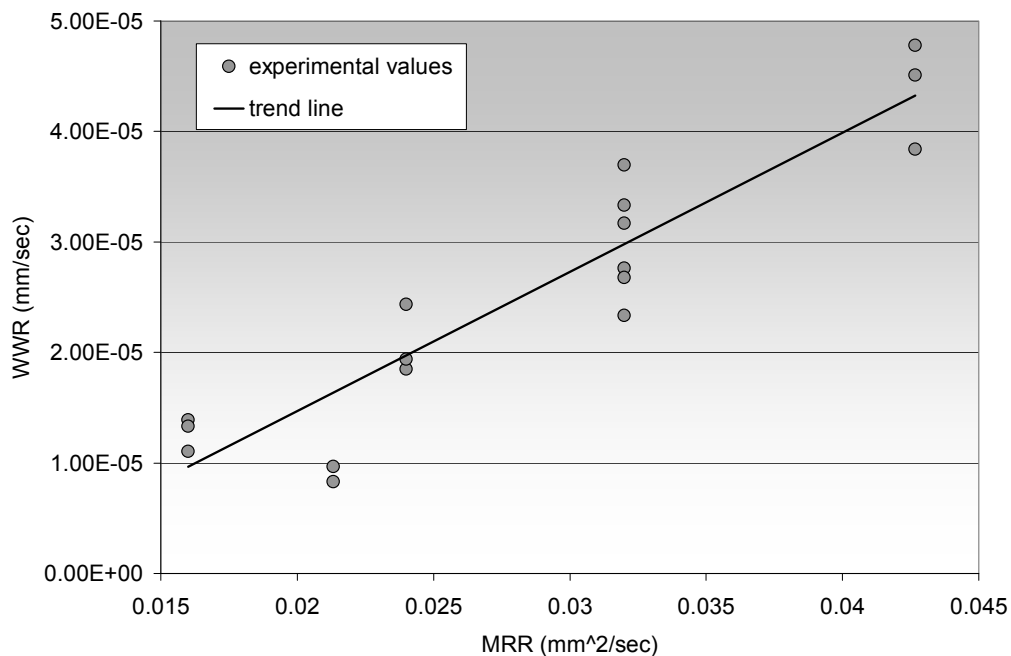
Figure 6.2: Plot of wheel wear rate (WWR) vs material removal rate (MRR)

Material removal rate (MRR), is a commonly used function (defined in Eqn. 6.1 per unit wheel width), but is not specific because it does not consider the grinding wheel speed, S (m/sec). Different combinations of depth-of-cut, d_c (μ), and feed rate, f_r (mm/sec), can have the same value of MRR (mm^2/sec), but the effect of depth-of-cut in wheel wear is more pronounced [83-85] than that of feed rate and should have more weightage than the later. MRR becomes even more irrelevant for wheel wear estimation of ELID Grinding because it does not consider dressing parameters. Figure

6.2 shows the poor correlation of WWR with MRR, with multiple WWR values for different current duty ratios but same MRR.

$$MRR = \frac{1}{60000} f_r d_c \tag{6.1}$$

Regression analysis of the WWR data provided a specific relation with the grinding parameters which has been approximated by the following empirical relations (Eqn. 6.2a).

$$w_r \propto d_c^2 , \; w_r \propto f_r \text{ and } w_r \propto \sqrt{S} \tag{6.2a}$$

Metal dissolution rate is directly proportional to current and hence, WWR is also dependent on current duty ratio, d_r (%). So, the benchmark function, termed the ELID Wear Factor (EWF), w_f is defined (Eqn. 6.2b), with which different grinding experiments can be compared.

$$w_f = d_c^2 f_r \sqrt{S} d_r \tag{6.2b}$$

Mechanical action is responsible for oxide layer wear, which in turn increases electrochemical activity and causes wheel wear. This mechanical action depends on the kinematic parameters of grinding. A mechanical wear factor (MWF) is also defined as a benchmark for comparing mechanical action of grinding among different experiments (Eqn. 6.2c). Justification of this function will be made clear in the following sections.

$$w_{mf} = d_c^2 f_r \sqrt{S} \tag{6.2c}$$

In the subsequent sections, the phrase 'mechanical action' and MWF have been used synonymously for implying the mechanical grinding action responsible for oxide erosion.

6.2.3   Categorization of ELID Grinding

A very basic concern for ELID grinding is the choice of dressing conditions for a particular set of kinematic grinding parameters. Choice of low dressing will lead to wheel loading and high dressing will lead to excessive electrochemical action. Now that a benchmark function (MWF) is defined for differentiating between different sets of kinematic parameters, the rates of electrochemical and mechanical actions can be compared. Figure 6.3 shows a matrix of different MWF versus duty ratio (representing electrochemical action). Identification of good dressing conditions from bad ones is made by comparing their correlation with wheel wear.
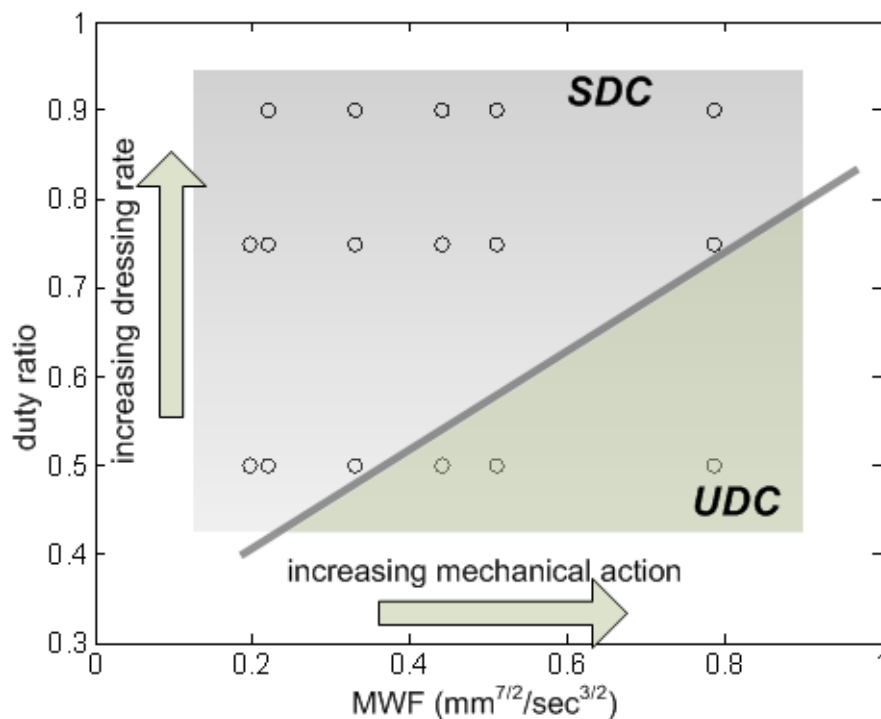
Figure 6.3: Matrix of duty ratio vs MWF (mechanical wear factor)

The upper left corner of the matrix in Figure 6.3 represents low rate of mechanical erosion of the oxide layer with high duty ratio enabling high current. The lower right corner of the matrix represents high mechanical erosion rate of the oxide layer with low electrochemical action for oxide formation and metal dissolution.

High erosion rate of oxide accompanied by its low formation rate leads to smaller transient region of grinding i.e. the pre-dressed layer is worn off sooner than when the in-process dressing rate is higher. High erosion also removes oxide faster during the steady stage of grinding accelerating the partial wheel loading process and therefore increasing the frequency of periodicity for grinding force and dressing current.
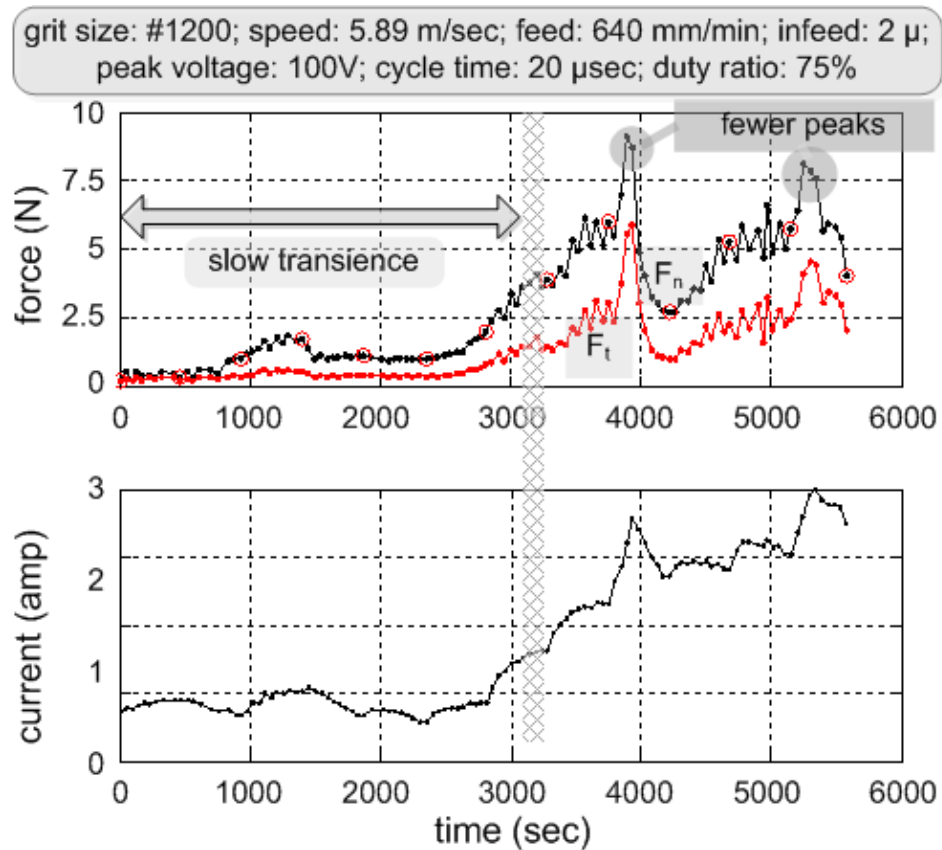
Figure 6.4: Grinding characteristics for experiment with low MRR

Comparative study of Figure 6.1, 6.4 and 6.5 illustrate these variations. Low MWF (d_c = 2μ, S = 5.89 m/sec, f_r = 640 mm/min, MWF = 0.003275 units) with good dressing in Figure 6.4 shows high transient time with low frequency of periodicity of force and current in the steady region, as compared to the case (d_c = 3 μ, S = 5.89 m/sec, f_r = 320 mm/min, MWF = 0.003684 units) shown in Figure 6.1. Equal MWF with different dressing rates can be compared in Figure 6.5a and b with the same conclusions of changing transient times and periodic oscillations of force and current.

Figure 6.5: Grinding characteristics of experiments with high MRR

When the mechanical action is too high compared to electrochemical reaction rate, the oxide formation cannot keep up with its erosion rate. This causes the metal surface of the bond to be exposed, and with low electrode gap, arcing between cathode and

grinding wheel can take place. This causes unusual wear behavior of the wheel and unpredictability sets in. Periodic loads on the wheel can also cause micro-cracks on the metal where the edges of diamond abrasives can act as initiation sites. These micro-cracks might give way to produce pitting again leading to unpredictable wear behavior. Figure 6.6 shows such instances of pitting and/or arcing after grinding with high mechanical action and low dressing rate.
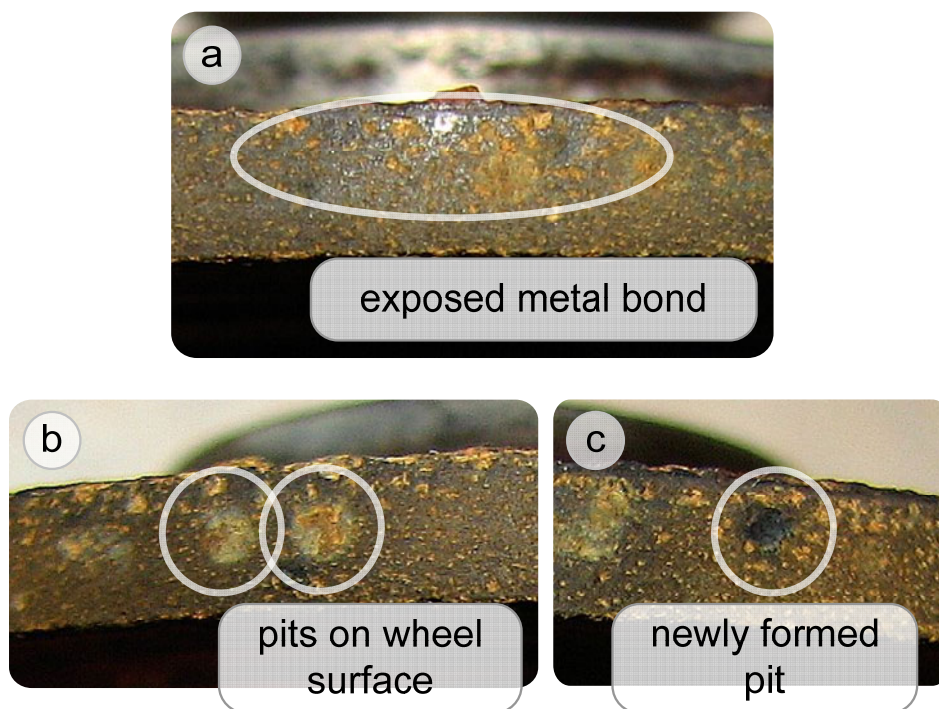
Figure 6.6: Macroscopic view of #1200 grit size grinding wheel surface immediately after steady state grinding insufficient dressing

Based on this criterion of unusual wear phenomenon, the ELID grinding conditions are categorized into under-dressed conditions (UDC) and sufficiently dressed conditions (SDC). The segregation between these two conditions is shown by the diagonal line in the Figure 6.3 matrix with SDC on the upper part and UDC below the line. Comparison of wheel wear for these conditions in the following section will further justify the categorization.

6.2.4   Relationships between Variables

During steady stage of grinding, a stable oxide layer is present on the wheel surface and its amount of wear is dependent on the kinematic parameters. For SDCs, this mechanical action is not directly responsible for metal bond wear because it only erodes the oxide layer. Electrochemical action is directly responsible for wheel wear and can be explained through fundamental electrochemistry. The theory of dressing developed in Chapter 5 explains electrochemical dissolution of metal bond where Eqn. 5.1b relates oxide layer thickness to dressing current and density of metal bond. For constant PBR, volume of oxide is directly proportional to volume of metal dissolved. So, metal bond dissolution can be formulated by Eqn. 6.3.

$$\frac{dL_m}{dt} = \eta \frac{M_m}{zFs_m A_e} I \tag{6.3}$$

This equation only considers the volume of metal in the grinding wheel, and not the volume of abrasives. This can be incorporated into Eqn. 6.3 from the concentration specification of the grinding wheel.

Concentration of the wheel refers to the carat weight of abrasives contained in a unit volume of bond material (expressed in cubic centimeter). A concentration of unity equals to *0.044 carats* (*0.044 x 0.200 gm = 0.0088 gm*) of abrasive per cc of bond material. The concentration of the wheel, p, used in the study is 100. So, mass of abrasives per unit volume of bond is *0.0088p*. Volume of abrasive present is therefore pk_o/s_a where s_a is the density of the abrasives and k_o=*0.0088*. Metal bonded wheels have low porosity [86] and is neglected in the formulation. Eqn. 6.3 is thus modified to Eqn. 6.4.

$$\frac{dL_m}{dt} = \eta \frac{M_m}{zFs_m A_e} \left(1 + \frac{pk_o}{s_a}\right) I \tag{6.4}$$
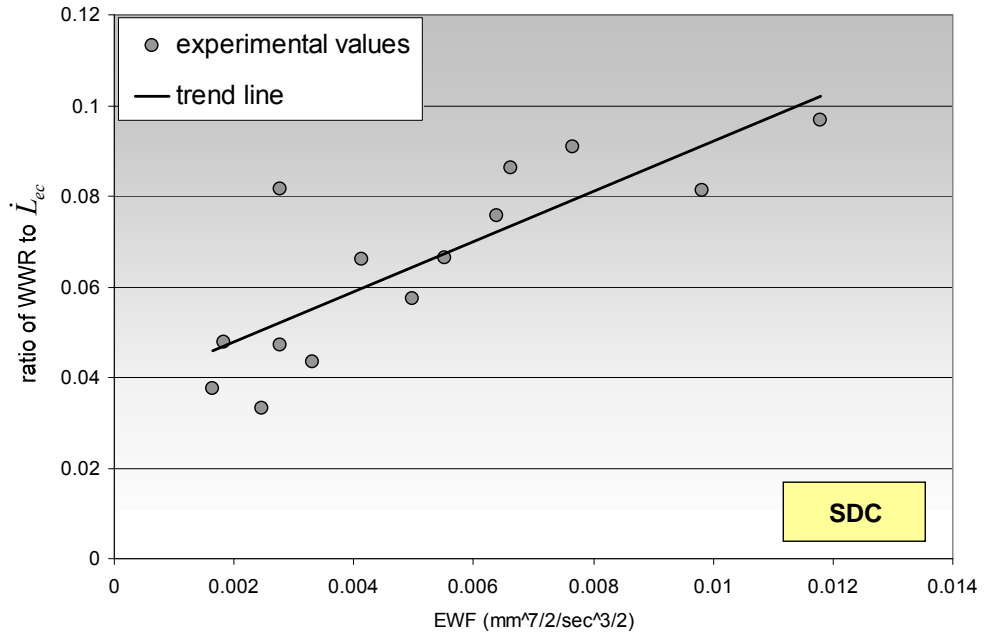
Figure 6.7: Plot of ratio of WWR to $\dot{L}_{ec}$ vs Electrochemical Wear Factor (EWF) for Sufficiently Dressed Conditions (SDC)

The effective time of dressing also governs the metal dissolution rate. For every rotation of the wheel, each point on the wheel is dressed for $\alpha/360^{th}$ time of rotation, where α is the included angle (in degrees) of the wheel being dressed by the cathode at any point of time. This factor is included into Eqn. 6.4 to get Eqn. 6.5.

$$\dot{L}_{ec} = \frac{M_m}{zFs_m A_e}\left(1 + \frac{pk_o}{s_a}\right)\frac{1}{\alpha/360}I \qquad (6.5)$$

Here $\dot{L}_{ec}$ is the theoretical wheel wear rate considering 100% efficiency of reaction. All the coefficients for Eqn. 6.5 are known from the experimental specifications, viz.:

$M = 55.847$, $z = 2$, $s_m = 7.3$ gm/cc, $p = 100$, $k_o = 0.0088$ and $s_a = 3.5$ gm/cc, $\alpha = 90$ deg, $A_e = 1.57$ cm^2.

$\dot{L}_{ec}$ is found to be higher than the actual WWR for all cases and the ratio of WWR to $\dot{L}_{ec}$ has an increasing trend when plotted against EWF (Figure 6.7). If this ratio is

77

tentatively equal for all the experiments, then the WWR would be directly proportional to electrochemical reaction rate, but is not so. Low layer thickness is formed by high mechanical action and vice versa. So, the layer thickness is governed by the ELID grinding inputs. Oxide layer controls movement of ions to and from the anode, so that a thicker layer decreases the efficiency of the reaction and vice versa. In spite of having the current to oxidize the metal bond, the efficiency/rate of the electrochemical reaction is further controlled by the layer thickness. The reaction rate however increases with lower oxide thickness and hence higher EWF, as shown in Figure 6.7. In case of UDCs, the average layer thickness becomes very low so that it becomes almost nonexistent at some locations. This exposed bond metal can trigger pitting or arcing.
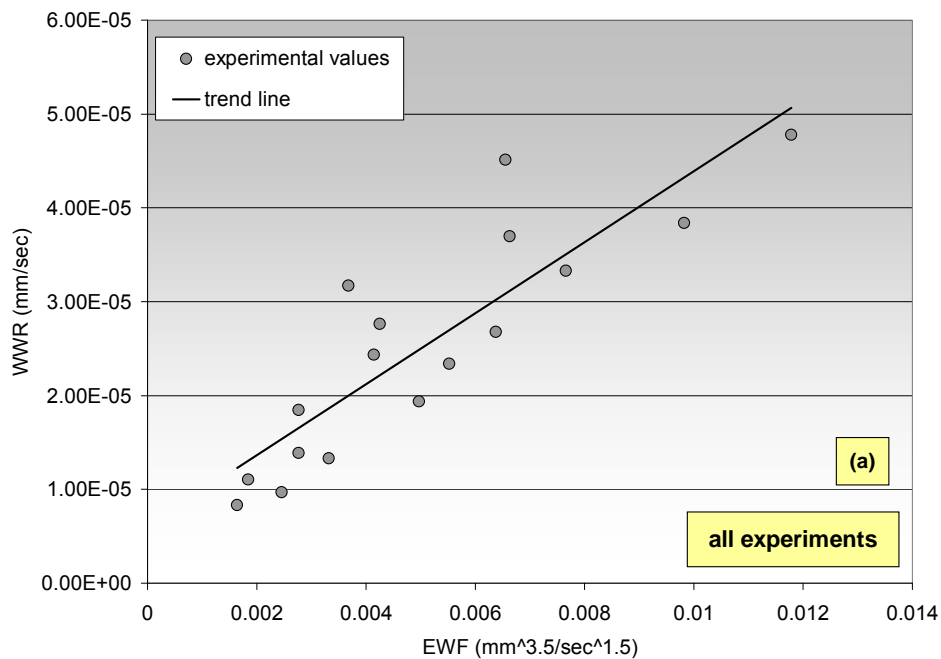
Figure 6.8a: WWR vs Electrochemical wear factor for all experiments

Now that the relation between the two important variables of ELID grinding, current and WWR, is clear, their variation with grinding parameters are discussed. As stated before, oxide layer in the steady grinding zone is more stable and consistent compared

to the pre-dressed layer. A plot of WWR vs EWF in this region is shown in Figure 6.8a for all the cases shown in the matrix in Figure 6.3. The regression coefficient obtained for a straight line is 0.75. When the UDC cases are eliminated from the plot (Figure 6.8b), the linear regression coefficient increases to 0.93 implying a good correlation between WWR and ELID grinding parameters. This indicates the more involved and complicated wear behavior of UDC experiments which may be more difficult to predict. WWR plotted against the product of MRR and duty ratio also has a good correlation for the SDC cases. It is to be noted here that high EWF does not imply UDC though it does imply high wheel wear rate.
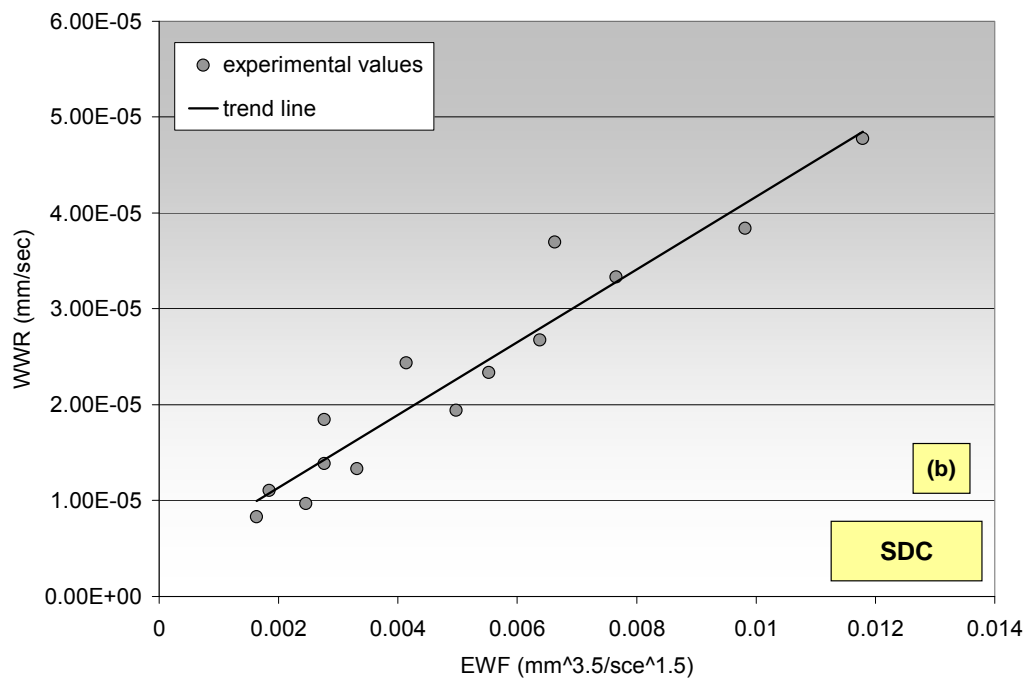
Figure 6.8b: WWR vs Electrochemical wear factor for experiments with SDC

Average dressing current, I_d, during the steady grinding period is plotted vs EWF in Figure 6.9 for SDC cases and a regression coefficient of 0.88 is obtained for a linear distribution. Current depends on the amount of oxide present on the wheel, which in turn depends on its erosion and formation rates. These rates are governed by the mechanical and dressing parameters. Therefore, it is expected that dressing current,

like WWR, will bear a signature of the ELID grinding parameters, which is reflected in Figure 6.9.
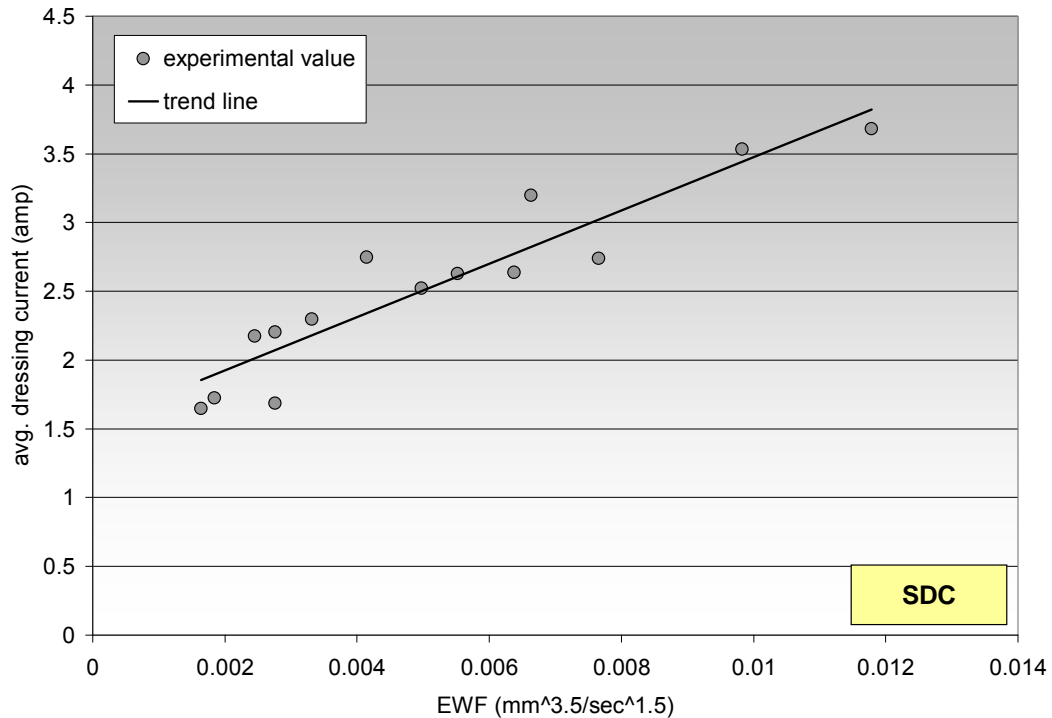
Figure 6.9: Dressing current vs Electrochemical Wear Factor (SDC)

6.2.5   Effect on Finished Surface

Effects on the wheel surface during grinding have been discussed in the previous sections, and this section is dedicated to the quality of ground surface generated during the experiments and methods of improvement. ELID grinding has the initial stage, with a thick layer of pre-dressed oxide, and the steady stage of grinding, with a thin oxide layer. Surface finish of ground component during the two stages of grinding are investigated as follows.

A representative surface generated during the initial stage of ELID grinding is compared with one generated during steady stage of grinding (Figure 6.10). The Ra value does not have any significant change with the operating stages. Change in the material removal mechanism of the two stages is, also, not observed.

Correlation between surface finish for different dressing and grinding parameters is also investigated. Surface finish produced by the #1200 wheel is in the range of 6.5 nm to 25.5 nm Ra. Specific relationship of surface finish (Ra value) with the wheel wear benchmark parameters EWF, MWF or MRPR is not observed (Figure 6.11). However, micro-photographs of the ground surface reveal changes in mechanism of material removal with grinding conditions.

(a)

(b)
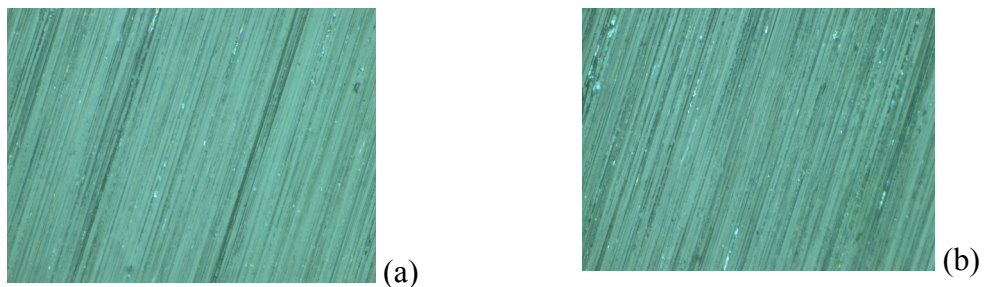
Figure 6.10: Surfaces generated during steady and initial stages of ELID grinding (x1000) with *S = 9.8 m/sec, f_r = 320 mm/min, d_c = 3 μ, MWF = 0.004756 units, EWF = 0.003567 units, d_r = 75%* (a) during steady stage of grinding (Ra 11.5 nm), (b) during initial stage of grinding (Ra 14.7 nm)
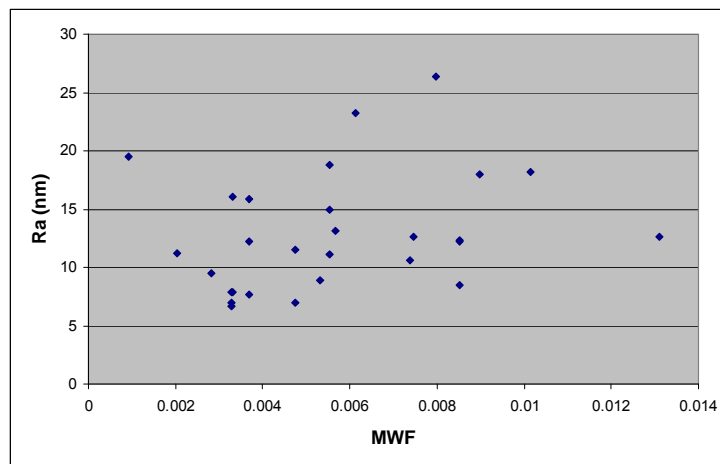
Figure 6.11: Variation of surface roughness (Ra value in nm) with MWF

Ductile regime material removal is predominant during grinding as seen from the magnified view of the ground surfaces (Figure 6.12). Part of the material removal is also through brittle fracture as can be seen in Figure 6.12a, e, f and h where there is a combination of low grinding speeds and low depth-of-cut (2μ). Material removal with 3μ depth-of-cut, with a variety of grinding speeds and feeds, removes material by

plowing action but not by brittle fracture (Figure 6.12b, c, d). It is also observed that grinding with high depth-of-cut of 4 microns has a ductile regime material removal (Figure 6.12g).
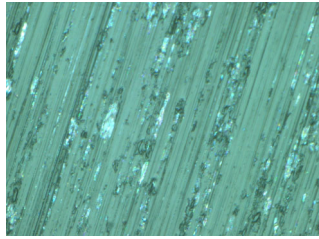
(a) $S = 5.9$ m/sec, $f_r = 640$ mm/min, $d_c = 2$ microns, $d_r = 50\%$, Ra = 6.9 nm, MWF = 0.003265, EWF = 0.001637
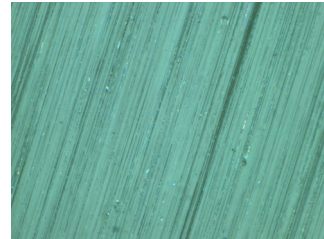
(b) $S = 9.8$ m/sec, $f_r = 320$ mm/min, $d_c = 3$ microns, $d_r = 75\%$, Ra = 11.5 nm, MWF = 0.004756, EWF = 0.003567
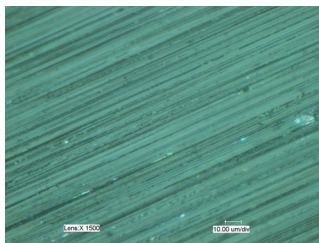
(c) $S = 5.9$ m/sec, $f_r = 780$ mm/min, $d_c = 3$ microns, $d_r = 50\%$, Ra = 18 nm, MWF = 0.00898, EWF = 0.00449
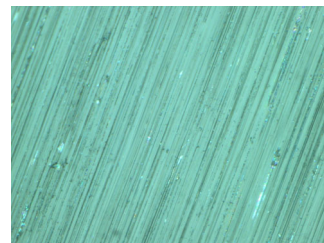
(d) $S = 5.9$ m/sec, $f_r = 640$ mm/min, $d_c = 3$ microns, $d_r = 75\%$, Ra = 10.6 nm, MWF = 0.007368, EWF = 0.005526
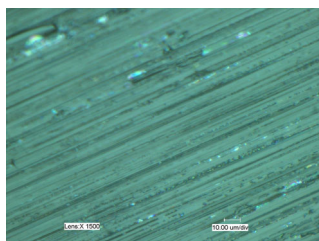
(e) $S = 5.9$ m/sec, $f_r = 1200$ mm/min, $d_c = 2$ microns, $d_r = 25\%$, Ra = 23.2 nm, MWF = 0.00614, EWF = 0.001535
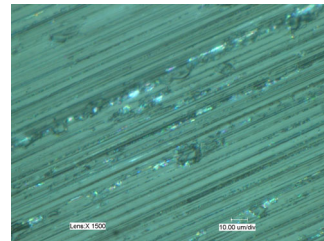
(f) $S = 7.9$ m/sec, $f_r = 960$ mm/min, $d_c = 2$ microns, $d_r = 75\%$, Ra = 13.1 nm, MWF = 0.005672, EWF = 0.004254
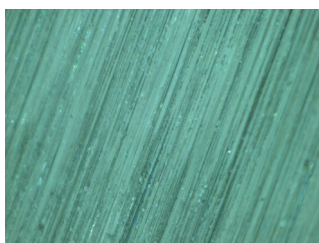
(g) $S = 5.9$m/sec, $f_r = 640$ mm/min, $d_c = 4$ microns, $d_r = 90\%$, Ra = 12.6 nm, MWF = 0.013099, EWF = 0.011789
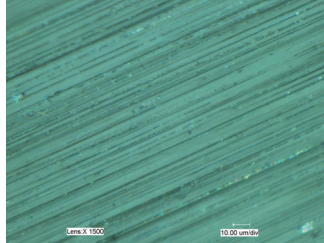
(h) $S = 6.9$m/sec, $f_r = 600$ mm/min, $d_c = 2$ microns, $d_r = 60\%$, Ra = 7.9 nm, MWF = 0.003316, EWF = 0.00199

Figure 6.12: Microphotograph of ground surfaces under 1500x magnification for different grinding and dressing conditions

Surface quality can be enhanced by incorporating idle passes (i.e. dressing operation is performed but grinding is not) in the continuous grinding scheme as shown in Figure 6.13 as opposed to like the scheme shown in Figure 3.3. The distinction between the idle and active passes is explained in the figure. Increased dressing time, t_d, over grinding time, t_g, produces better dressing thereby generating better surface finish. This time of dressing can be controlled by increasing the travel distance d shown in the figure.
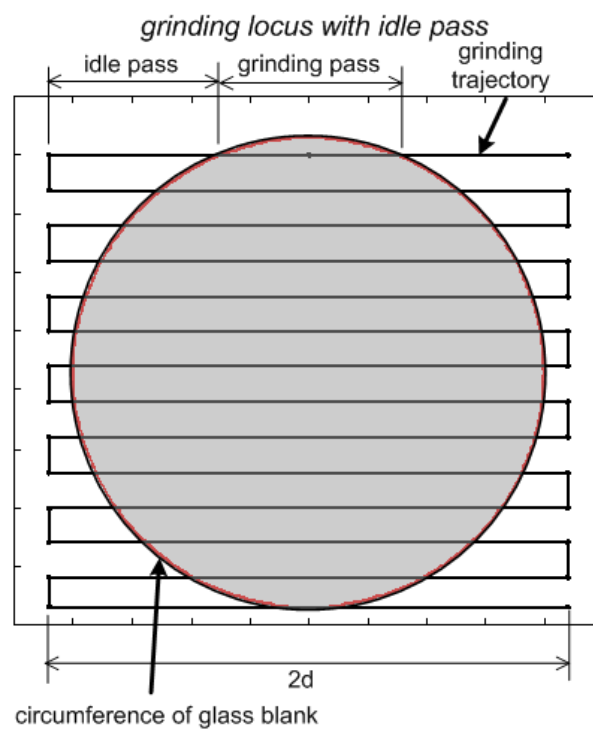
Figure 6.13: Grinding scheme incorporating idle strokes

Table 6.1 shows the grinding conditions with and without idle pass and the respective Ra values achieved. Introduction of idle passes also enables efficient grinding with UDC as shown in the table. Comparison of the ground surfaces generated by grinding with and without idle passes is shown in Figure 6.15. It can be seen that brittle fractures produced with some continuous grinding parameter values are reduced when idle passes are introduced.
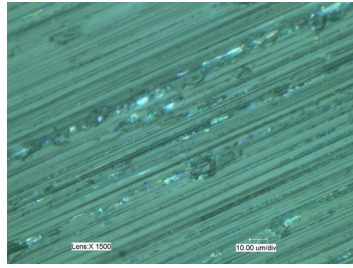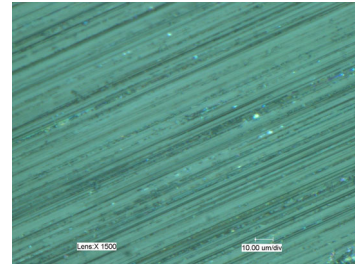
continuous grinding   *with idle pass*

(a) $d_c = 2\mu$, $f_r = 960$ mm/min, $S = 7.9$ m/sec, $d_r = 75\%$, $t_d/t_g = 1.36$
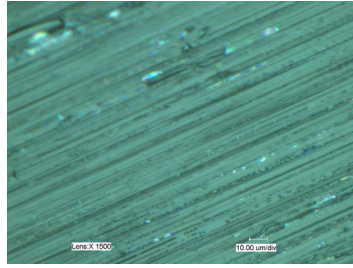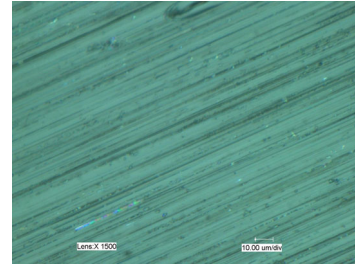
continuous grinding   *with idle pass*

(b) $d_c = 2\mu$, $f_r = 1200$ mm/min, $S = 5.9$ m/sec, $d_r = 25\%$, $t_d/t_g = 1.54$
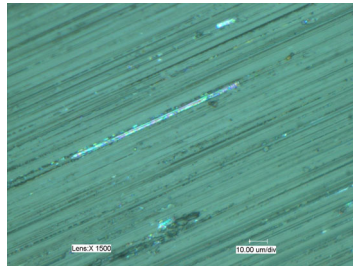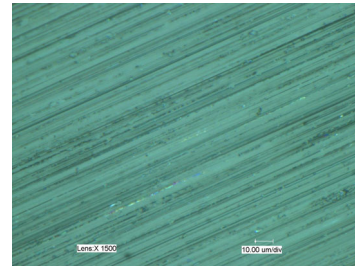
continuous grinding   *with idle pass*

(c) $d_c = 3\mu$, $f_r = 720$ mm/min, $S = 8.8$ m/sec, $d_r = 90\%$, $t_d/t_g = 1.36$

Figure 6.14: Comparison of surface produced by grinding with and without idle pass

Table 6.1: Comparison of surface finish for ELID grinding with and without idle pass

Sl. No.	d_c (μ)	f_r (mm per min)	S (m per sec)	d_r (%)	D (mm)	Ra (nm) without idle pass	Ra (nm) with idle pass	t_d/t_g
1	3	600	7.9	67	22	26.4	17.25	1.36
2	3	720	8.8	90	22	18.2	13.8	1.36
3	2	600	6.9	60	22	16.1	15.7	1.36
4	2	960	7.9	75	22	13.1	13.3	1.36
5	3	780	5.9	50	25	18.0	14.2	1.54
6	2	1200	5.9	25	25	23.2	18.6	1.54

6.3   Brittle Mode Grinding

In ELID grinding of hard and brittle materials with coarse abrasive wheels, mechanism of material removal is through propagation and intersection of brittle fractures, as compared to the plowing action during ductile regime grinding. Brittle mode grinding experiments with #325 abrasive (size 44μ) are carried out to investigate the grinding mechanism. Figure 6.15 shows the variation of current and grinding forces for a representative experiment. The periodic variation of force and dressing current is low or absent. The current and forces reach a steady value after the pre-dressed layer is worn off within a short transient period. A minor increase or decrease in the current can be observed after the pre-dressed layer is worn off. The grinding mechanism is purely through brittle fracture (Figure 6.16). A definite empirical relationship between grinding parameters and current has not been obtained. However, a good correlation is developed theoretically in the next chapter and the results have been clarified.
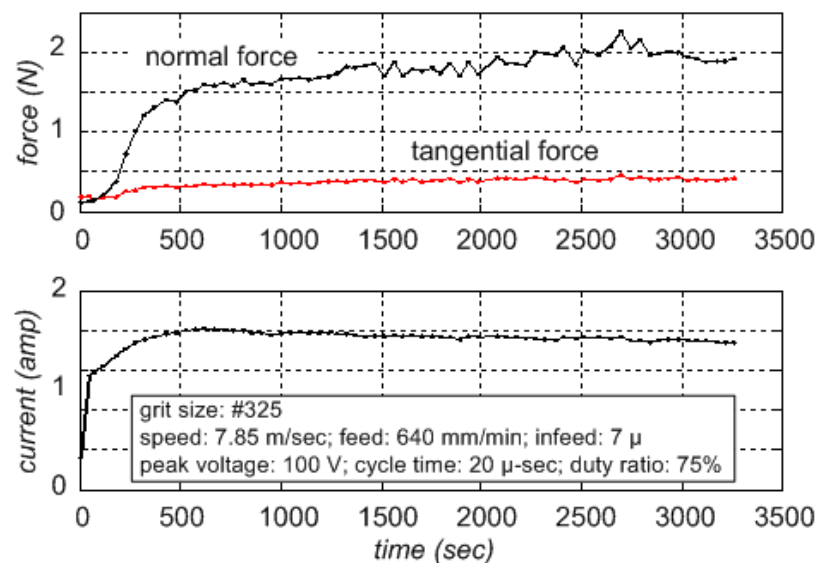
Figure 6.15: Force and current characteristics for grinding BK7 glass blanks with #325 wheel
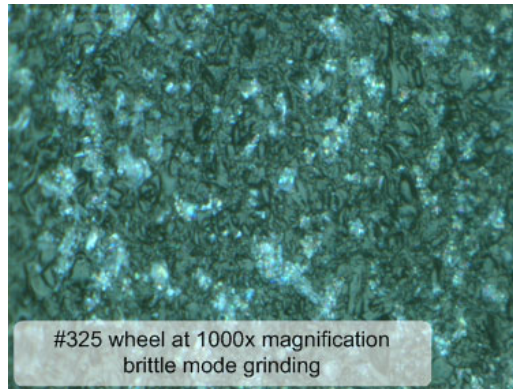
Figure 6.16: Microscopic image of BK7 glass surface ground with #325 wheel showing material removal by brittle fractures

6.4 Concluding Remarks

Two important aspects of ELID grinding are wheel wear and appropriate choice of dressing conditions for a set of machining parameters. In this chapter, experiments are conducted for a quantitative estimation of wheel wear for different dressing and machining parameters for ductile regime ELID grinding. ELID is distinguished into the initial and steady stages of operation and the later stage creates a thinner oxide layer than the pre-dressed layer. So, experiments where the dressing rate is very low, the metal bond is exposed and arcing and/or pitting occurs. Based on these observations, the different experiments are categorized into sufficiently dressed conditions and under-dressed conditions. A benchmark function is defined to correlate wheel wear rate with ELID grinding input parameters. Under sufficient dressing conditions, the wheel wear rate during steady grinding has a good correlation with the input parameters. Dressing current during steady grinding is also found to bear a signature of the input parameters. The surfaces generated during grinding with different parameters values are compared, and a grinding passes incorporating idle passes is seen to provide better surfaces. Brittle mode grinding with ELID is also studied and its force and current did not have the periodic variations.

In the next chapter the analytical model for electrolytic dressing is further developed along with an empirical model for oxide erosion. The two models are combined to obtain a semi-empirical model for wheel wear and dressing current.

Chapter 7

SEMI-EMPIRICAL MODEL

7.1 Introduction

In the previous chapters, the *electrical properties of the electrolyte* are investigated and the results are used in formulating the *equations for electrolytic dressing*. Since metal bond dissolution is the governing mechanism of wheel wear, electrolytic dressing equations can be modified to obtain expressions for wheel wear. Grinding experiments conducted in Chapter 6 explains the *mechanism of grinding* and shows empirical *correlation between WWR and input parameters*. So, a distinct behavior pattern is found to be present in the ELID grinding mechanism. Modeling of ELID grinding is developed and discussed in this chapter.

Electrochemical action is important for the overall ELID grinding process. It forms the anodic oxide layer from the metal bond. The oxide then erodes off due to the grinding action and exposes new sharp abrasives to carry on efficient grinding. Oxide formation rate is determined by the dressing current, which in turn is again determined by the existing oxide layer thickness and the dressing parameters of *applied voltage* and *current duty ratio*. The existing oxide layer thickness depends on the grinding parameters viz.: *grinding speed*, *feed rate* and *depth-of-cut*. The relationship of dressing current with the ELID grinding input parameters are studied and contribute to the fundamental research of ELID grinding.

The electrolytic dressing is first formulated and the relationship between oxide layer thickness, applied voltage and duty ratio is established. The change in oxide layer thickness due to its erosion or formation can consequently reveal the corresponding dressing current. An empirical wear model for oxide erosion is then combined with the analytical model of electrolytic dressing, to obtain a semi-empirical model. The analytical model for oxide erosion is established in Chapter 8.

7.2   Electrochemical Formulations

Electrochemical action is modeled by Faraday's Laws of Electrolysis which relate the metal dissolution rate (or oxide formation rate) with dressing current (Eqn. 7.1, obtained from Eqn. 6.3) [33, 78]. The volume of oxide has a definite ratio to the volume of metal present in it, called Pilling Bedworth Ratio (PBR). This ratio being known, the volume of oxide, without the abrasives, can be obtained (elaborated in Chapter 5) (Eqn. 7.2). Volume of metal dissolved is obtained from Eqn. 7.1, but volume of grinding wheel dissolved also includes the volume of abrasives. Eqn. 7.3 formulates the relation between the total volume of metal bond and abrasives, V_t, to the volume of bond, V_m (explained in Section 6.2.4).

$$\frac{dV_m}{dt} = \eta \frac{M}{zFs_m} I \tag{7.1}$$

$$V_{ox} = cV_m \tag{7.2}$$

$$V_t = V_m \left(1 + \frac{pk_o}{s_a} \right) \tag{7.3}$$

The Eqns. 7.1, 7.2 and 7.3 can be represented by Eqn. 7.4, for oxide formation per unit rotation of the wheel, after expressing the volume of metal bond dissolved in terms of area and oxide thickness.

$$l_e = \eta \frac{M}{zFs_m A_e}\left(c + \frac{pk_o}{s_a}\right)It_e \qquad (7.4)$$

Current efficiency i.e. the efficiency of electrochemical reaction in producing oxide depends on the existing oxide layer thickness with higher thickness hindering the reaction rate more than low thickness. So, it is given as a linear function of oxide layer thickness and has been defined by Eqn. 7.5. The function is explained with Figure 7.1 where the current efficiency η is maximum of η_2 when there is no oxide layer with linearly reducing value upto a thickness $L_{\eta2}$ beyond which η remains constant at the minimum value of η_1.

$$\eta = \eta_1 + \left(1 - \frac{L}{L_{\eta1}}\right)(\eta_2 - \eta_1) \text{ for } L \leq L_{\eta1} \text{ and } \eta = \eta_1 \text{ for } L > L_{\eta1} \qquad (7.5)$$
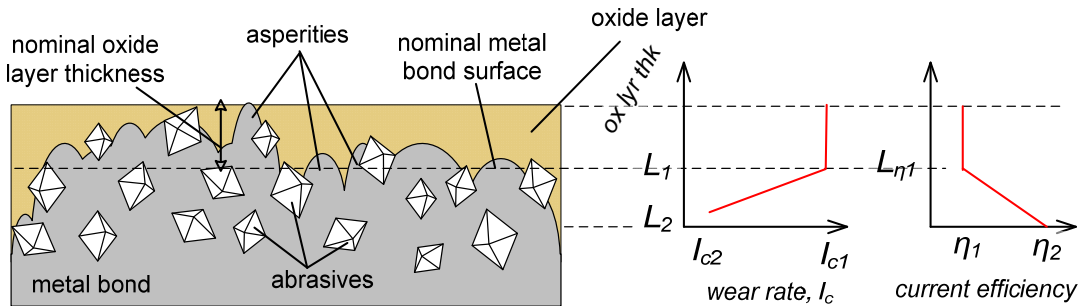
Figure 7.1: Variation of wear and current efficiency with oxide layer thickness

Another relation between oxide layer thickness and current can be obtained from the electrical circuit model of the electrolysis (Section 5.2.2). The electrical circuit has a series of two resistances, one for the electrolyte and another for the oxide layer/film (Eqn. 7.6, from Eqn. 5.2).

$$d_r V_0 = \left(R_e + \frac{\rho}{A_e}L\right)I \qquad (7.6)$$

Equations 7.4, 7.5 and 7.6 can be solved to obtain the change in amount of oxide formed and the respective current, during dressing for every rotation of the wheel.

The time per rotation is calculated from the spindle rpm S, as $60/S$ sec. The time of electrolysis per rotation, t_e is obtained from the segment of wheel that is being dressed (angle α expressed in degrees) at any particular time. So, the dressing time per rotation is given by Eqn. 7.7.

$$t_e = \frac{\alpha}{360}\frac{60}{S} = \frac{\alpha}{6S} \tag{7.7}$$

The oxide layer thickness after the ith rotation can be obtained from Eqn. 7.8.

$$L_{i+1} = L_i + l_e \tag{7.8}$$

This will result in a reduction in the metal bond because it is consumed to form the oxide. There will also be a corresponding increase in the net wheel radius (for $c>1$). But the net wear of grinding is a reduction in wheel radius due to the mechanical reaction on the grinding wheel, for which a suitable model is now required.

7.2.1 Formulation of Oxide Erosion

In spite of the oxide layer being very soft and brittle, it adheres to the grinding wheel surface even under the action of grinding forces. This is possible because the oxide is reinforced by the asperities of the metal–oxide interface (Figure 7.1). Grinding action compresses the oxide, as well as worn off grits and grinding chips, between the grits and the undulations to provide a stable composite layer. The thickness of this layer, which is referred as *oxide layer*, is therefore related to the average height of the asperities.

Wear rate or erosion rate of this layer is stipulated by grinding parameters. In the Chapter 6, it was found that WWR is empirically related to the square of depth-of-cut (Eqn. 7.9).

$$w_r \propto d_c^{\ 2} \tag{7.9}$$

It is reasonable to assume that wheel wear rate is proportional to the material removal per rotation, (also known as the *equivalent chip thickness* [87] of grinding), m_r (Eqn. 7.10) (expressed in µ/sec per unit mm of wheel width).

$$m_r = \frac{d_c f_r}{S} 10^3 \tag{7.10}$$

Combination of relations 7.9 and 7.10 yields the relation 7.11 which relates the order of magnitude of oxide erosion to be a function of the various grinding parameters.

$$w_r \propto \frac{d_c^{\ 2} f_r}{S} 10^3 \tag{7.11}$$

The oxide layer is strongest near the metallic interface because it is reinforced by the metal surface undulations and the active grits partially embedded in the metal matrix. So, the wear rate will decrease with the reduction of the oxide layer thickness. Beyond the undulations, the oxide layer is loosely adhered and of very low mechanical strength. So, the wear rate is assumed to be high and constant when the layer thickness is greater than the height of undulations. Wear rate of oxide, when its thickness is within the undulation height, is defined as a linearly decreasing function of the layer thickness, as shown in Figure 7.1 (Eqn. 7.12). The lowest value of wear rate is l_{c2} at the lowest layer thickness of L_2 and the highest is l_{c1} at L_1.

$$l_c = l_{c2} + \frac{L - L_2}{L_1 - L_2} \left(l_{c1} - l_{c2} \right) \text{ for } L \le L_1 \text{ and } l_c = l_{c1} \text{ for } L > L_1 \tag{7.12}$$

The constants l_{c1} and l_{c2} are defined in terms on l_{c0} (expressed in µ) which in turn is obtained by introducing a constant of proportionality k_x into Eqn. 7.11 as follows.

$$l_{c0} = k_x \frac{d_c^2 f_r}{S} 10^3 \qquad\qquad (7.13)$$

The constant k_x is determined empirically and is termed the *erosion constant.* It depends on the grinding wheel grit size, bond material and work material, and not on ELID grinding parameters.

7.2.2   Combination of Oxide Formation and Erosion

The new oxide layer thickness after the ith wheel rotation i.e. after the ith electrochemical reaction and mechanical wear, is obtained with Eqn. 7.14.

$$L_{i+1} = L_i + l_e - l_c \qquad\qquad (7.14)$$

7.3   Solution for Brittle Mode Material Removal

Experimental results discussed in Chapter 6 are used to evaluate the model. Some different experiments are also performed to evaluate certain coefficients used in the equations, and other coefficients are obtained from the material specifications of the grinding wheel. The coefficients obtained from experimental conditions are *M=55.85, V$_0$=100V, s$_m$=6.87gm/cc, p=100, s$_a$=3.5gm/cc, A$_e$=1.57cm^2.* PBR for divalent iron oxide is 1.7 and so, *c=1.7.* Pre-dressed layer of oxide is required before starting the grinding operation, and so a layer thickness of *L$_{ini}$=50μ* is assigned as the initial condition of the simulation.

The profile of undulation on #325 wheel surface is obtained by measuring the pre-dressed wheel after scrapping off the oxide with abrasive cloth. Taylor Hobson Ultra Surface 396 machine is used for the measurement (Figure 7.2) and the undulations are found to vary in the range of 30 to 40μ. The maximum wear occurs at the highest peak of undulation, *L$_1$*, which is taken as *L$_1$=40. L$_2$* is the thickness of oxide with

minimum wear rate. So, it is very close to the metal surface and is equal to the minimum oxide thickness on the wheel. This is approximately equal to 6μ, as determined through microscopic observations, i.e. $L_2=6\mu$. The respective wheel wear rates are assumed as, $l_{c2}=l_{c0}$. The ratio of average grinding force during steady stage to initial stage is approximately 5, and so ratio of maximum to minimum wear is also assumed to be in the same ratio and the maximum wear rate is assumed as $l_{c1}=5l_{c0}$.
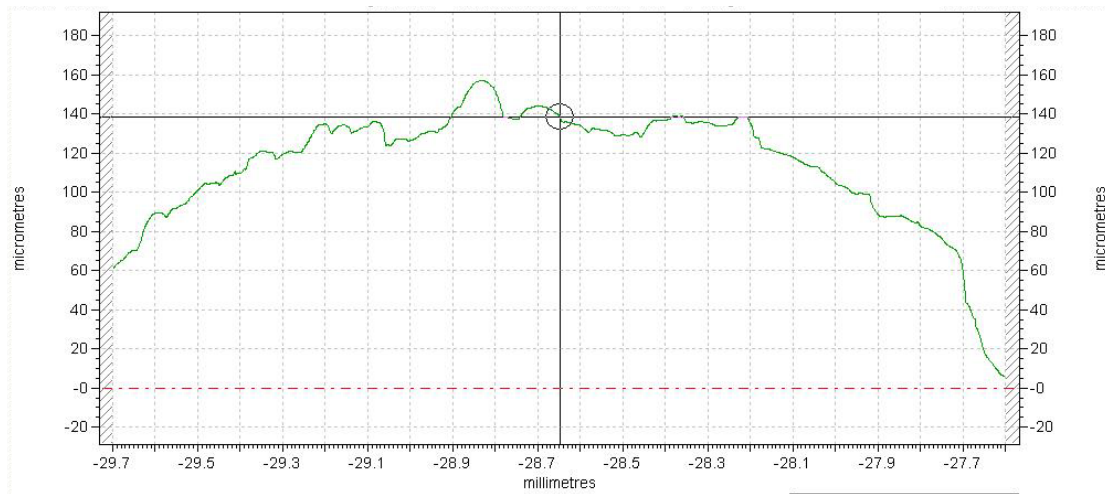
Figure 7.2: Profile of pre-dressed #325 wheel surface measured with touch probe after scrapping off the oxide layer

Current efficiency is determined from pre-dressing experiments. Profile of the wheel is measured after dressing for 40 minutes and then scrapping off the anodic oxide with an abrasive cloth. This is compared with the wheel profile before dressing to get the amount of metal dissolution (27μ) during the dressing operation. The electric charge is calculated from the dressing current measurements and the theoretical metal dissolution is obtained from Faraday's Laws of Electrolysis (377μ). The average current efficiency of the process is thus obtained to be approximately 6%. Current efficiency during the dressing process is maximum when there is no oxide layer and gradually reduces with the increase in layer thickness. The increase in the layer thickness is rapid during the initial stage, followed by a slow increase in the post

initial stage (Chapter 5). Consequently, the current efficiency decreases rapidly in the initial stage and then its decrease is gradual. The average value of this current efficiency variation is 6%. So, the minimum value is close to the average value and the maximum is relatively higher. The current efficiency values for the model are assumed around this experimental value as $\eta_1=5\%$ for oxide thickness $L_{\eta 1}=40\mu$ (equal maximum undulation peak), and the maximum is assumed to be $\eta_2=15\%$ when no oxide is present.

Resistance of the electrolyte is found from voltage and current measurements during dressing operation with the oxide scrapped off the grinding wheel. This way the resistance obtained is offered only due to the electrolyte flow. Effect of gas generation, calculated from Bruggeman equation [67], is found to have negligible effect on the resistivity of the electrolyte (Chapter 4). Resistance of the electrolyte flow conditions thus obtained for the experimental flow conditions is $R_e=12.5\Omega$ (Figure 4.7).

Oxide layer thickness of approximately 30μ is present during grinding with average dressing current of approximately 1.0A at 50% duty ratio and for $R_e=12.5\Omega$. Oxide resistivity under with such inputs is found (from Eqn. 7.6) to be $\rho=15x10^3$ Ω-cm.

Since the coefficients have been evaluated, the governing equations can be solved. Equations are solved for every rotation of the wheel, for each cycle to oxide formation during dressing, followed by oxide erosion due to grinding. Current is calculated from Eqn. 7.6, and Eqns. 7.4 and 7.5 are used to find the oxide formed. Eqns. 7.12 and 7.13 are solved to obtain the oxide erosion from the layer thickness. The new oxide layer thickness is then obtained from Eqn. 7.14, which in turn serves to find the current (from Eqn. 7.6) during the next cycle of oxide formation. Change in dressing current and oxide layer thickness can thus be obtained. The simulation results match with

experimental results for the value of the empirical constant $k_x=5x10^{-6}$ (Figure 7.3 and Figure 7.4).

7.4   Results and Discussions

Simulated results of dressing current development is compared with experimental values in Figure 7.3. It shows that the dressing current during coarse grinding reaches a stable value after the initial transience. This is only possible due to the presence of a stable layer of oxide, and the phenomenon is explained as follows.
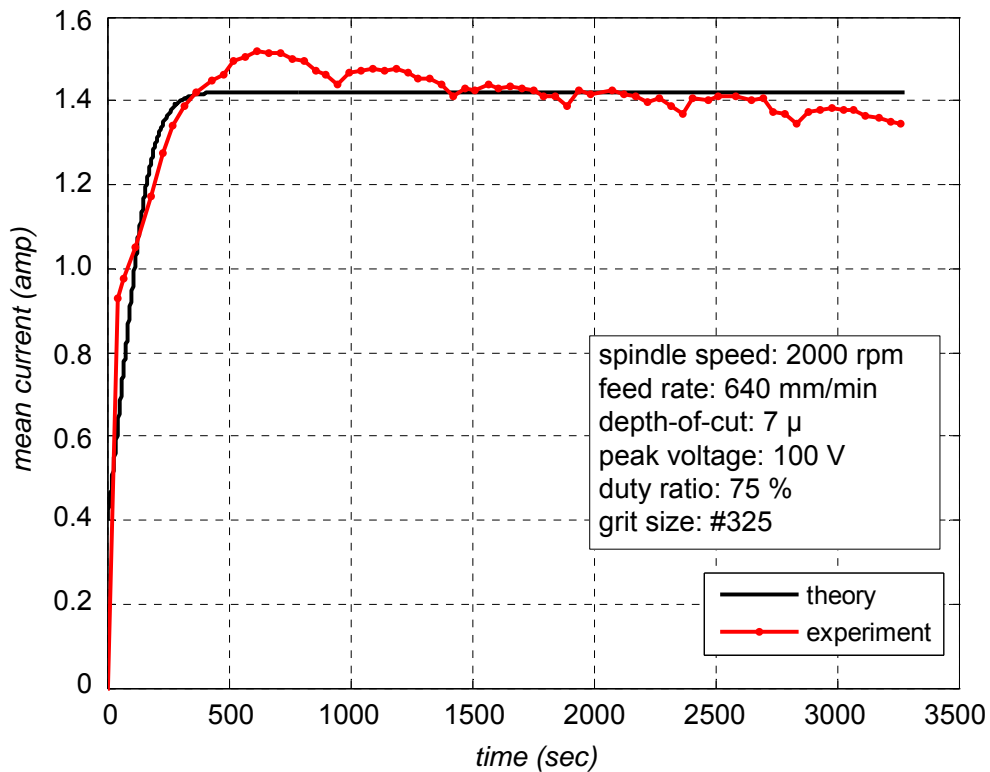
Figure 7.3: Comparison of simulation and experimental current development during coarse grinding

Initially, the oxide erosion rate is enhanced due to the presence of the thick pre-dressed layer, because oxide erosion rate increases with layer thickness (Eqn. 7.15). The thick layer also reduced current (Eqn. 7.6) thereby reducing the oxide layer

formation rate (Eqn. 7.4). As grinding progresses, the layer thickness reduces, thereby increasing the rate of oxide formation and decreasing the rate of erosion. Consequently, a steady state is reached, when the rate of formation and erosion reach equilibrium. So, in this state, the existing oxide layer thickness is such that enough current is allowed to replace the oxide worn off in the previous cycle, and the layer thickness reaches a stable value, as does the dressing current.

speed	2000 rpm	2000 rpm	2000 rpm	2000 rpm
feed rate	640 mm/min	640 mm/min	640 mm/min	1000 mm/min
depth-of-cut	10 μ	7 μ	7 μ	7 μ
duty ratio	25 %	50 %	75 %	50 %
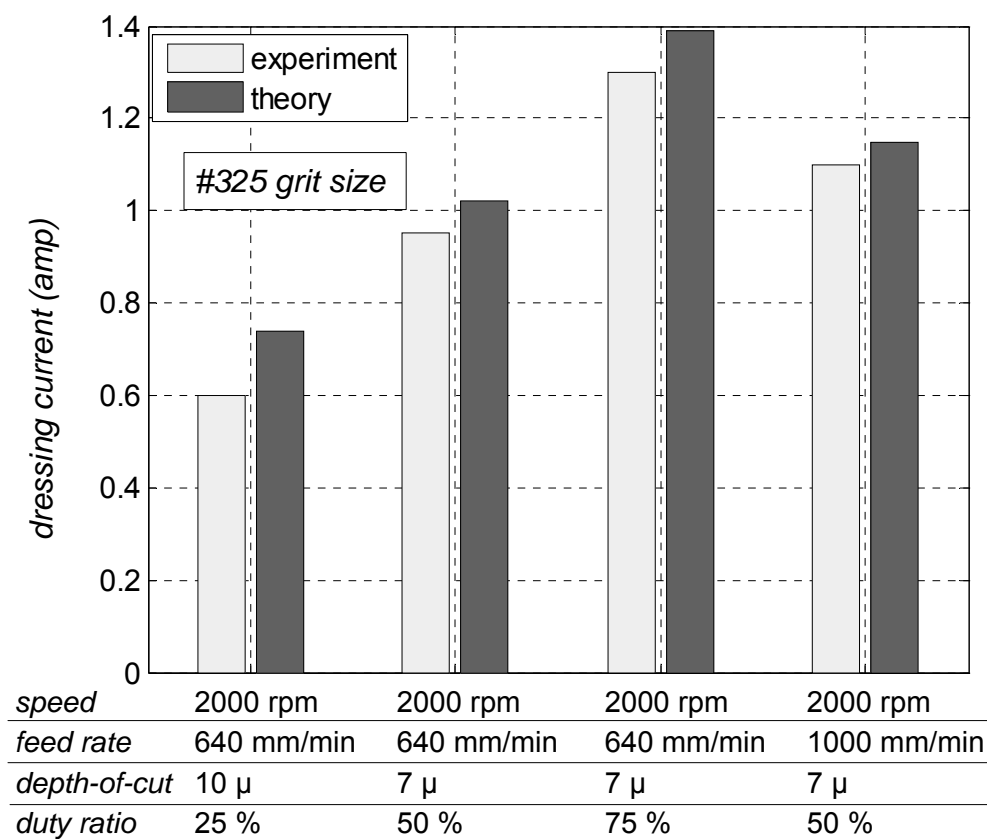
Figure 7.4: Comparison of theoretical and experimental steady state current during brittle mode grinding with #325 grit size

The oxide erosion rate is a function of grinding parameters (grinding speed, depth-of-cut and feed rate) and formation rate depends on dressing parameters (pulse ON time, OFF time and peak voltage), and so is the stable layer thickness. A comparison of the simulated and experimental stable current values shows good agreement in Figure 7.4. So, a distinct correlation between the dressing current and the input parameters is

possible for all combinations of dressing and grinding parameters other than certain conditions discussed hereafter.

The maximum value of current allowed during dressing is controlled by the resistance of electrolyte, duty ratio and applied voltage, when the oxide layer is absent. The rate of oxide formed by the maximum possible current can be lower than the rate of oxide erosion. Under such conditions, the wheel is insufficiently dressed and the lower limit of dressing can be obtained.
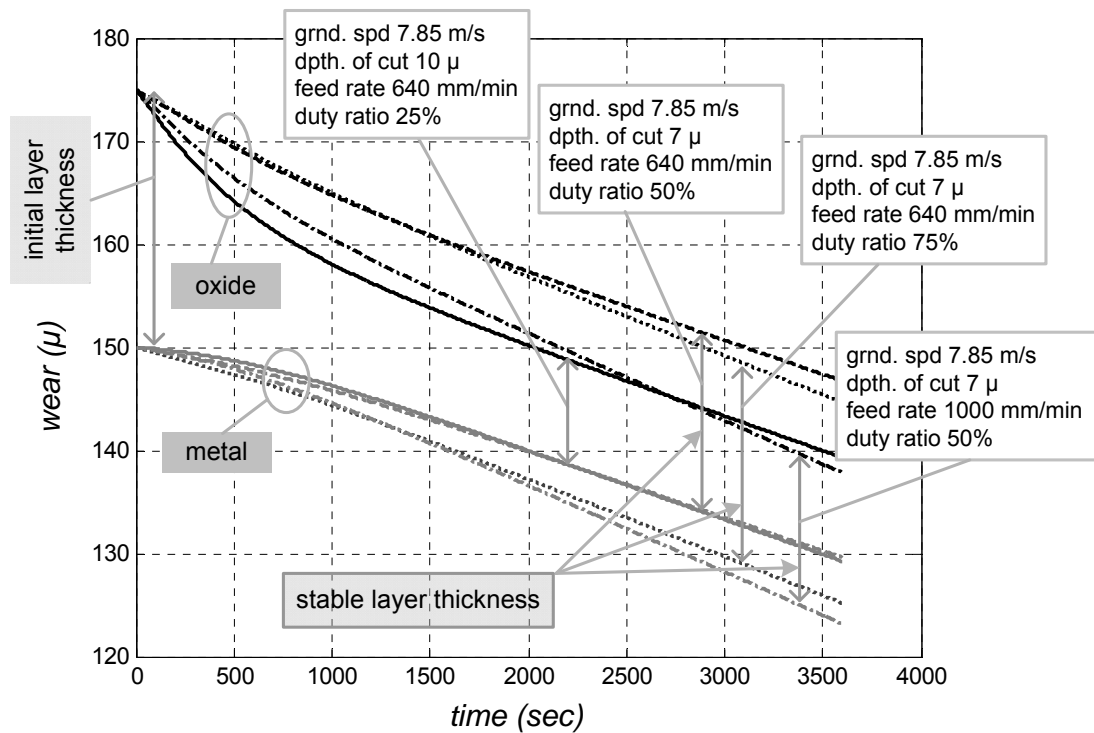
Figure 7.5: Simulated values of wheel wear of oxide and metal surfaces during coarse grinding

Dressing rate can also have a possible upper limit. The oxide layer has stability within the active grit height. When the dressing rate becomes so high that the equilibrium layer thickness goes beyond the active grit height, the un-reinforced oxide layer exhibits unpredictable behavior because of its soft and brittle nature. This situation is however difficult to practically achieve in coarse grinding because the large diameter

abrasives provide a high active grit height so that the stable layer remains within its bounds.

Simulation of changing oxide surface and underlying metal surface for different ELID grinding conditions is shown in Figure 7.5. Low grinding rates have a slow transience (initial stage) and thick stable layer, and vice versa. The figure also shows that thicker stable layer is present for low grinding rate with high dressing rate, and vice versa.
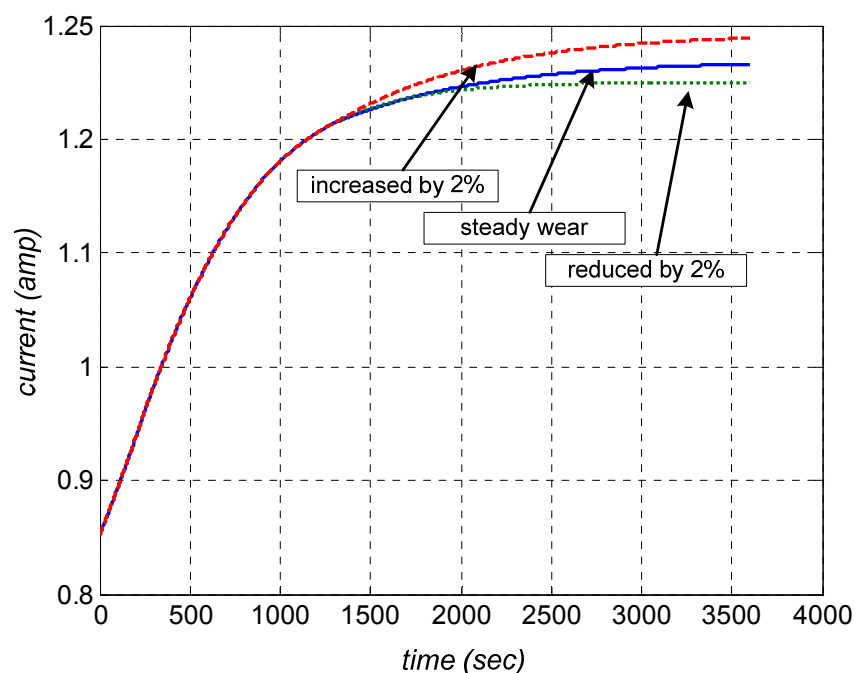
Figure 7.6: Simulation values for change in current characteristics when there is a small increase or decrease in the steady state wear rates

More careful scrutiny of the experimental result in Figure 7.3shows a decreasing trend in the steady state current. The current obtained from simulation is based on the assumption that the function of wear rate is very definite and is dependent on the existing oxide layer thickness only. So, this is a theoretical value which cannot accurately match practical values. In practical cases, the wear rate also depends on several other factors like grinding chips, locus of grinding path, stochastic nature inherent in grinding etc. So, there is invariably some change in the wear rate obtained

under steady state. Figure 7.6 shows the change in the dressing current for a small increase and decrease of 2% from the theoretically obtained steady wear rate. The 2% reduced wear rate shows a slightly decreasing trend of current, similar to the slightly decreasing trend obtained experimentally in Figure 7.3. An increase of 2% from the steady state wear rate shows a slight increase in the steady state dressing current.

7.5 Model Solution for Ductile Regime Grinding

In brittle mode grinding of brittle materials, material removal takes place by propagation and intersection of brittle fractures [4]. During fine grinding of brittle materials, plastically deformed chips are removed from the work surface by plowing action of the abrasives [88]. Difference between the forces and current for ductile and brittle mode ELID grinding experiments is that periodic variations are observed for the former and relatively lesser variation is observed in the later.

Some of the parameter values used in the model will be different for fine grinding. The height of undulations on the #1200 grinding wheel is determined from profile measurement shown in Figure 7.7. The maximum undulation height is found to be 25µ. So, $L_1=25$ and $L_{\eta 1}=25$. Exposed metal bond is observed during some grinding conditions, and so the minimum possible thickness of oxide layer is zero. So, $L_2=0$ and $L_{\eta 2}=0$. The initial value of layer thickness is taken as $L_{ini}=15$, based on pre-dressing experiment results in Chapter 5.

Oxide layer thickness of 5 to 8µ is present during grinding with average dressing current of approximately 1.0A at 50% duty ratio and for $R_e=12.5\Omega$. Oxide resistivity under with such inputs is found (from Eqn. 7.6) to be $\rho=75x10^3$ $\Omega\text{-}cm$ considering the average oxide layer thickness to be average of 5 and 8µ.

Figure 7.7: Profile of pre-dressed #1200 wheel surface measured with touch probe after scrapping off the oxide layer

7.6   Results and Discussions

The model results for steady state current and WWR match with experimental results for $k_x=0.001$ (Figure 7.8). Unlike the brittle mode grinding experiments, the steady stage during ductile mode grinding is marked by periodic variations of force and current. This is because the oxide erosion occurs in discrete steps during this set of experiments. So, the oxide layer does not have an entirely stable value during the steady stage, but varies within a limit so that its average value within periodic variations is constant. The existence of this thin layer of oxide, formed in the steady grinding zone, gives predictability to the ELID grinding process, and hence the definite correlation of WWR and dressing current with the input parameters is possible.

It is seen from Figure 7.8, that the cases with $d_c=2\mu$ have a high oxide layer thickness. WWR for such experiments is very low compared to the others, but the current is comparable to those with higher MRR. This indicates that even a small change in dressing current for an experiment can be an indication of significant change in WWR.

Comparison between experimental and simulation of wheel wear is shown in Figure

7.9 and Figure 7.10 has good agreement.
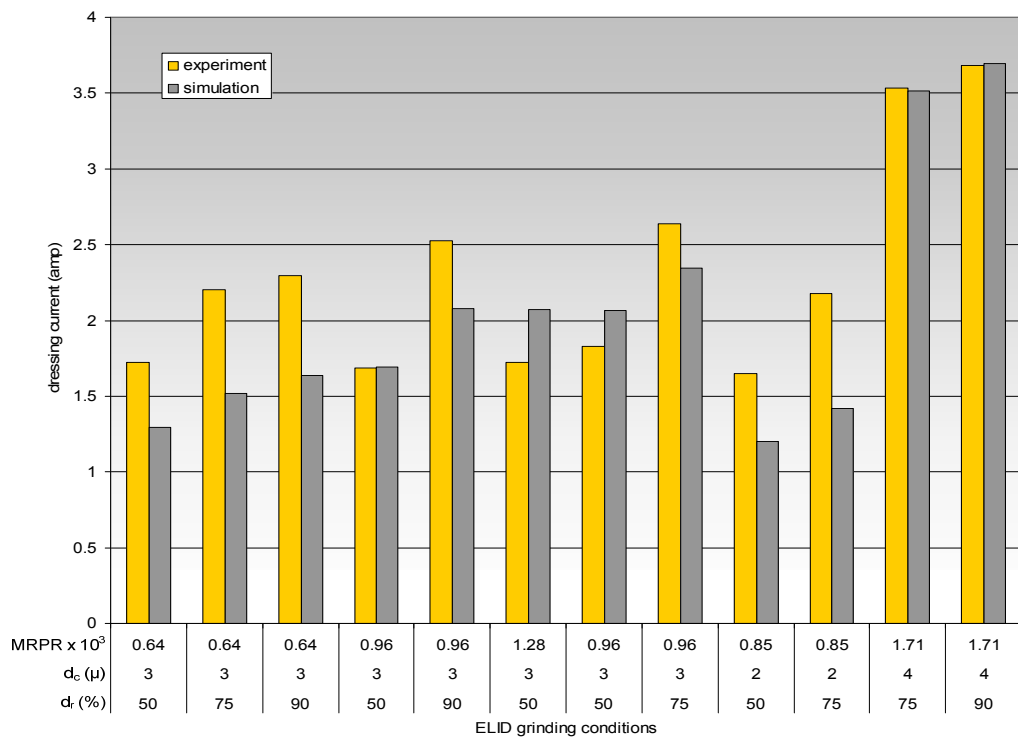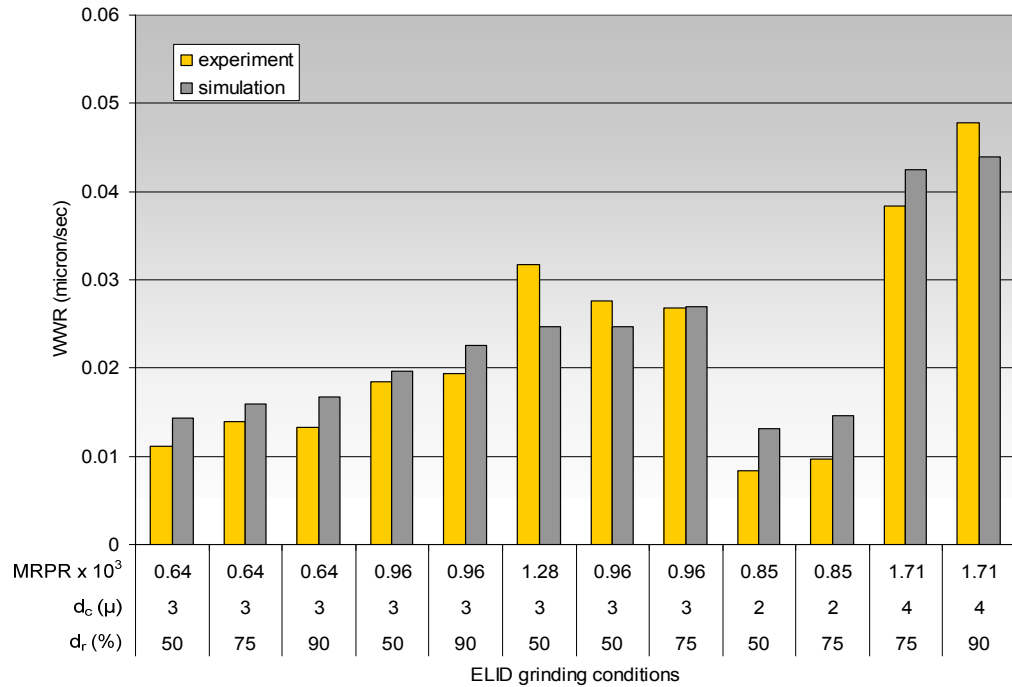
Figure 7.8: Comparison between experimental and simulation results of steady state
current and wheel wear rate for different ELID grinding conditions for mirror finish
of BK7 glass with #1200 wheel
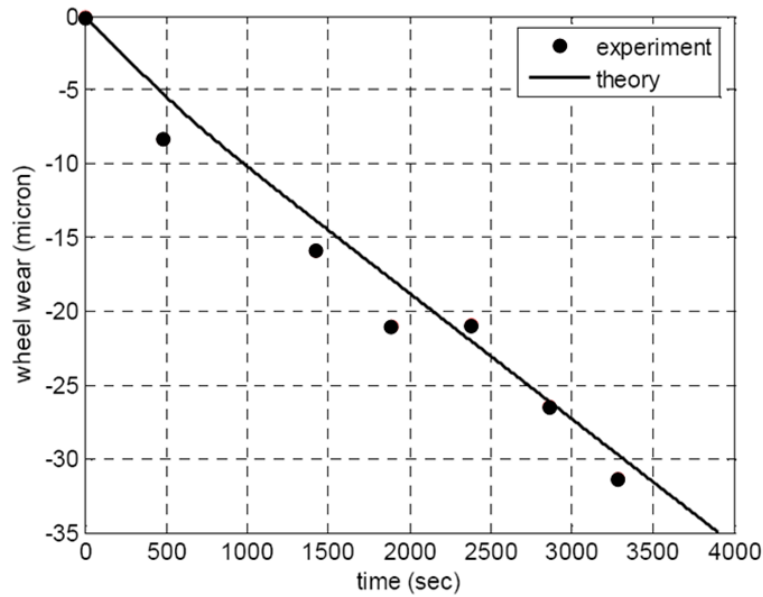
Figure 7.9: Comparison of simulation and theoretical wheel wear during steady grinding for *S=5.9 m/sec, f_r=640 mm/min, d_c=2μ, d_r=50%*
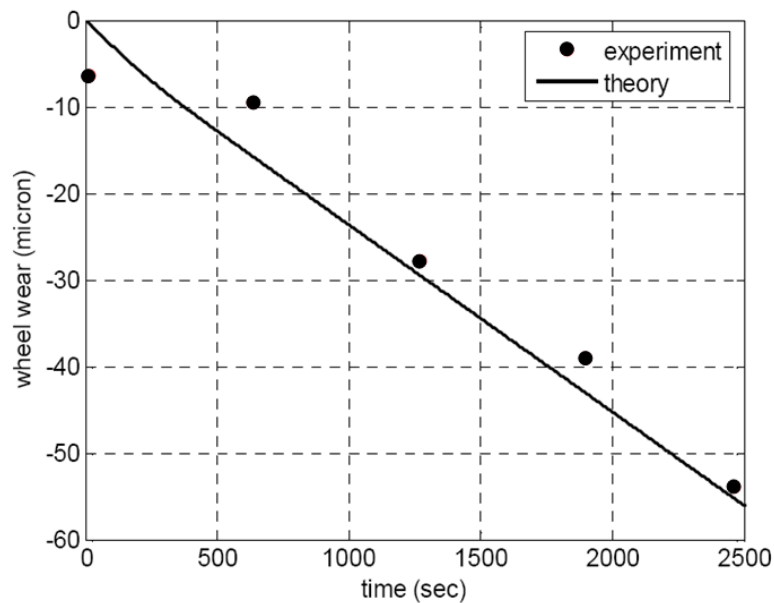
Figure 7.10: Comparison of simulation and theoretical wheel wear during steady grinding for *S=5.9 m/sec, f_r=480 mm/min, d_c=3μ, d_r=90%*

With the help of the model, it is also possible to estimate wheel wear from dressing current. Monitoring wheel wear is an important issue in ELID grinding. In-process accurate measurement of wheel wear with electrical sensor systems, like inductive and capacitive, is difficult due to the insulating oxide layer and its unstable properties. Measurement with optical sensors, like laser displacement sensors, is difficult to

achieve in-process because of the interference caused by the splashing electrolyte. Tactile sensors will erode the oxide and produce erroneous results. However, as seen from the simulation results, wheel wear and current can both be tentatively predicted. So, correlation between wheel wear and dressing current can be used to monitor the former with relative ease. The properties of the oxide layer can also be a hindrance to this approach of wear measurement and so it is required that the measurement be carried out during the steady grinding zone when the layer is relatively stable.

Current signal, I_{exp}, obtained for a particular experiment is used to find the oxide layer thickness, L_{exp}, variation during the grinding operation by manipulating Eqn. 7.6 to get Eqn. 7.15.

$$L_{\exp} = \left(\frac{V_0 d_r}{I_{\exp}} - R_e \right) \frac{A_e}{\rho}$$
(7.15)
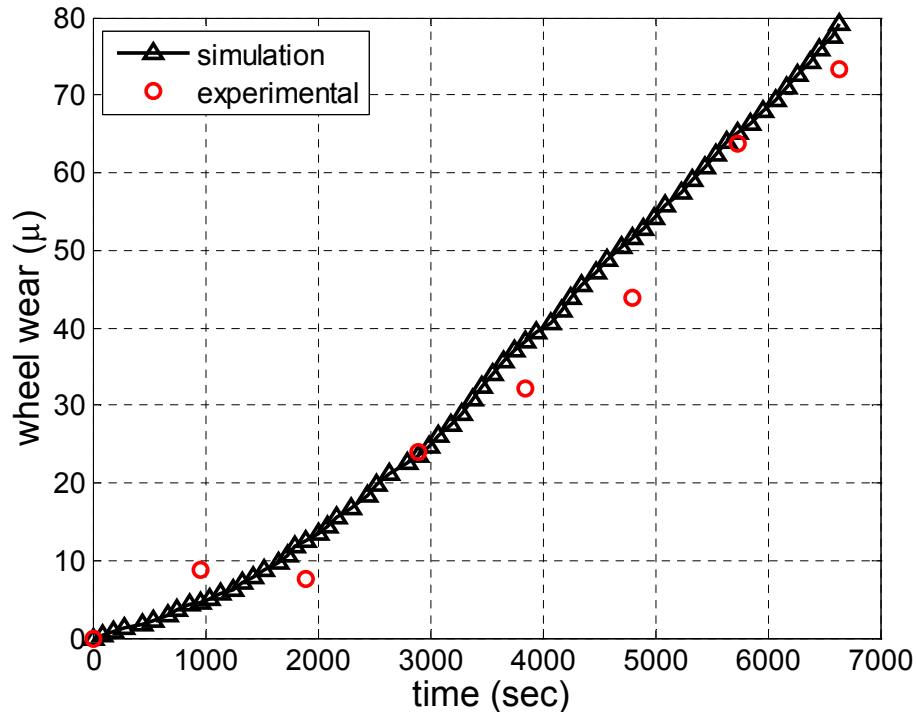
Figure 7.11: Wheel wear obtained from experimental dressing current compared with directly measured wheel wear for $S=5.9 m/sec, f_r=320\ mm/min, d_c=3\mu, d_r=75\%$

The respective current efficiency is obtained by putting the values of L_{exp} into Eqn. 7.5. The WWR is found by putting the current efficiency and I_{exp} values into Eqn. 7.4, which is then integrated, w.r.t. time, to find the variation of wheel wear. The values of the other coefficients used in the equations are the same as the ones used in the model. Figure 7.11 and Figure 7.12 show different experiments where the wheel wear has been predicted from the current signal are compared with the directly measured wheel wear.
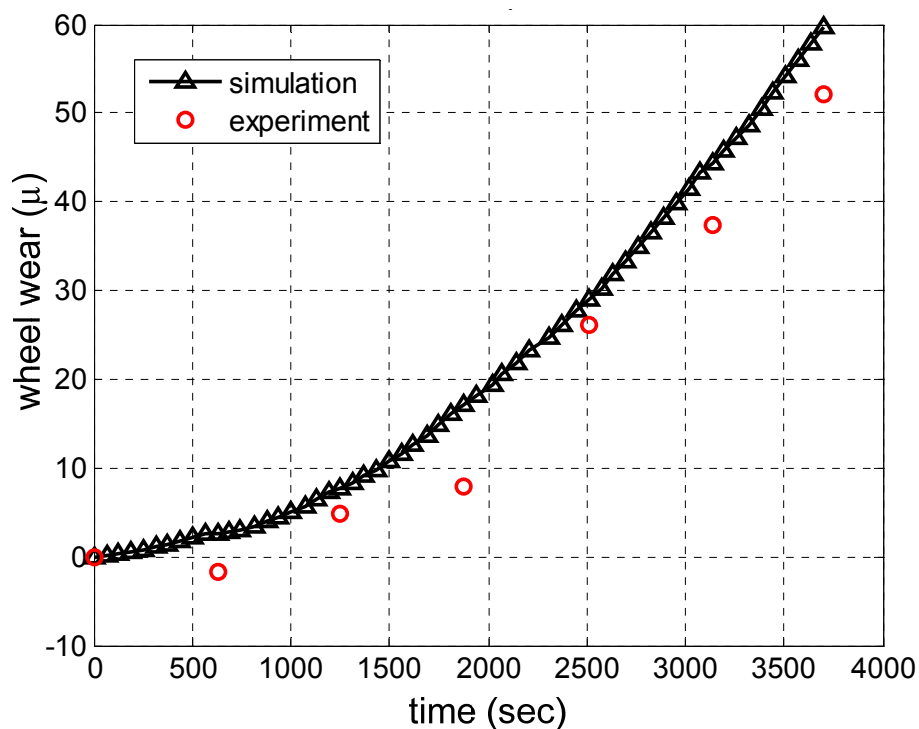
Figure 7.12: Wheel wear obtained from experimental dressing current compared with directly measured wheel wear for $S=5.9m/sec$, $f_r=480$ mm/min, $d_c=3\mu$, $d_r=90\%$

7.7 Concluding Remarks

Ideally, wheel wear in ELID grinding occurs through electrochemical dissolution of the metal bond. Electrolytic action on the grinding wheel is formulated as a function of electrical parameters. Electrolytic action also depends on the existing oxide layer thickness, the erosion rate of the oxide depends on the machining parameters. The

oxide erosion mechanism is formulated empirically. This empirical formulation and the analytical formulation for oxide formation are solved simultaneously to obtain a semi-empirical model for prediction of wheel wear and dressing current, for both, brittle and ductile mode ELID grinding. Simulation results show that the dressing current reaches a steady value after the pre-dressed layer is worn off during the transient stage of grinding. The layer thickness keeps reducing till the rate of oxide formation and erosion come to equilibrium and a *stable layer* thickness is reached, resulting in a stable current. The simulated values of steady state current and wheel wear rates have a good agreement with the experimental findings. Estimation of wheel wear from the experimental current is also possible from the formulation of electrochemical dressing.

Chapter 8

ANALYTICAL MODEL

8.1   Introduction

The semi-empirical model in Chapter 7 was composed of an analytical model of electrolytic dressing with an empirical model for oxide layer erosion. Proposed in this chapter is an analytical model for oxide erosion in ductile regime grinding. In combination with electrolytic dressing formulation, it will create a completely analytical model for wear estimation of ELID grinding.

Asperities on the grinding wheel surface after pre-dressing have peak height of approximately 25µ (Figure 7.7). The abrasive size for #1200 wheel is 13µ, which is responsible for generating the ground surface on BK7 glass. The abrasive size being much smaller than the asperity peaks, the undulations on the metal bond interface is not entirely due to protruded grits, but mostly metallic surface undulations itself [3]. These metallic asperities interact with the ground surface and in course of time undergo elastic, elasto-plastic or plastic deformation. This deformation is dependent on the grinding parameters, the work material and the bond material. In ELID grinding, wear of these asperities take place by electrochemical action. The oxide layer is held in the asperity interstitial sites, and so deformed asperities will partly stipulate the oxide layer thickness.

Oxide layer is worn off during grinding operation because the grinding chips interact with the oxide layer resulting in erosion of the later. Erosion of the oxide layer by the grinding chips also governs the average oxide layer thickness. The rate of electrolytic dressing also determines the layer thickness. So, the oxide layer thickness is determined by three phenomena:

i. deformation of asperity on wheel surface

ii. erosion of oxide by interaction of grinding chips

iii. electrolytic dressing rate

The oxide formation characteristics have already been determined in the last chapter. Since process forces are low in ELID grinding, the deformation of the asperities is elastic and its effect on oxide erosion is assumed to be negligible. The phenomenon of oxide erosion by grinding chips is formulated in this chapter.

When a plane, parallel to the asperity base, intersects the asperity, the intersection area is minimum at the tip of the asperities, from where it increases until it becomes equal to the nominal area of asperity base. The distribution of the intersecting area, A_c, with the distance, H, from a reference in the nominal plane can be represented by a specific relationship.

$$A_c = A_c(H) \tag{8.1}$$

The asperity on the grinding wheel surface is shown in Figure 8.1 where the area of intersection A_c at a distance H from the nominal surface is illustrated.

In case of ELID grinding, the wheel has several asperities which are formed by the interaction of the bond with the grinding chips, work material, pulled out abrasives, electrochemical action and also partially embedded abrasives. Due to electrochemical action on the asperities, they gradually become truncated and the contact area with the

ground surface changes. The model for oxide erosion is based on a control asperity (Figure 8.1b) over a control area on the grinding wheel surface.
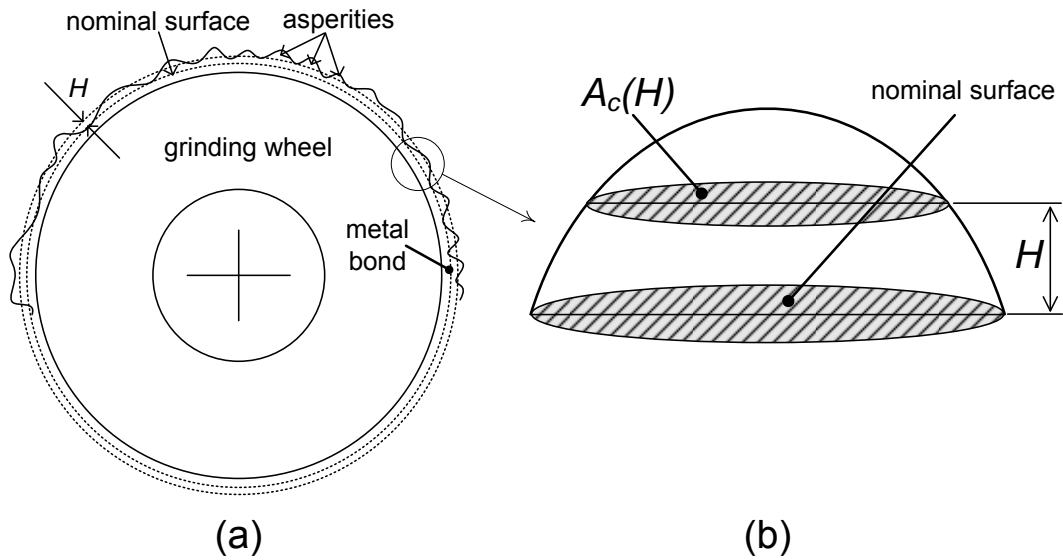
Figure 8.1: Representation of asperity on grinding wheel

The control area represents the *nominal area of the grinding wheel*. The area $A_c(H)$ of the control asperity represents the *probability distribution* of the contact area of asperities on the wheel at distance H from the nominal surface. This representative asperity can be said to represent an *average asperity* on the grinding wheel surface with the following assumptions:

i.   The average asperity shape remains unchanged except for its truncation.

ii. Geometry and volume of the abrasives does not have any significant effect on the shape and volume of the control asperity.

8.2   Geometry of Asperity

Referring to Figure 8.2, the geometry of the control asperity is defined by Eqn. 8.2.

$$\lambda = \lambda(h) \tag{8.2}$$
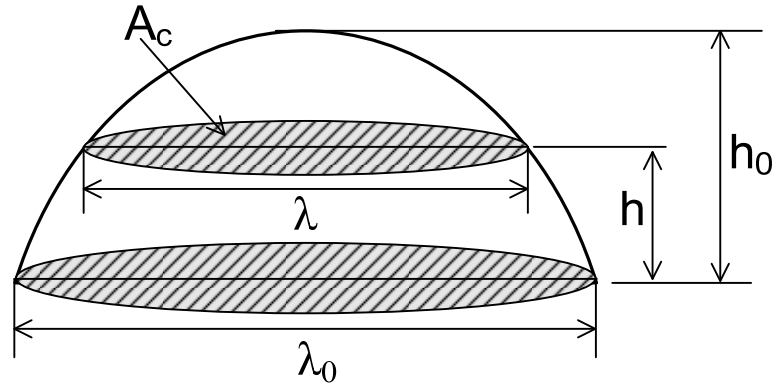
Figure 8.2: Asperity geometry

Here h and λ are the ordinate and abscissa of the central plane of the asperity. h_0 and λ_0 are their maximum values, as shown in Figure 8.2. It is important to note the following:

    i.   The volume of the asperity, V_{asp}, from peak upto a height h is given by the Eqn. 8.3.

$$V_{asp}(h) = \frac{\pi}{4}\int_0^h \lambda(\eta)^2\, d\eta \qquad\qquad (8.3)$$

    ii. The asperity has a circular base, but the control area on which it sits is square with side λ_0.

The oxide being present in the interstitial space of the asperities, the height of oxide present on the wheel is the height of the truncated asperity.

8.3 Oxide Wear from Grinding Chips

The oxide is present in the interstitial space between the asperities. The three dimensional schematic of the plastically deformed asperity over the control area $A_0 = \lambda_0^2$, with the surrounding oxide and the progress of the oxide erosion process, is

shown in Figure 8.3. Two-dimensional view of the same configuration is shown in Figure 8.4 for better illustration of the oxide erosion dynamics.
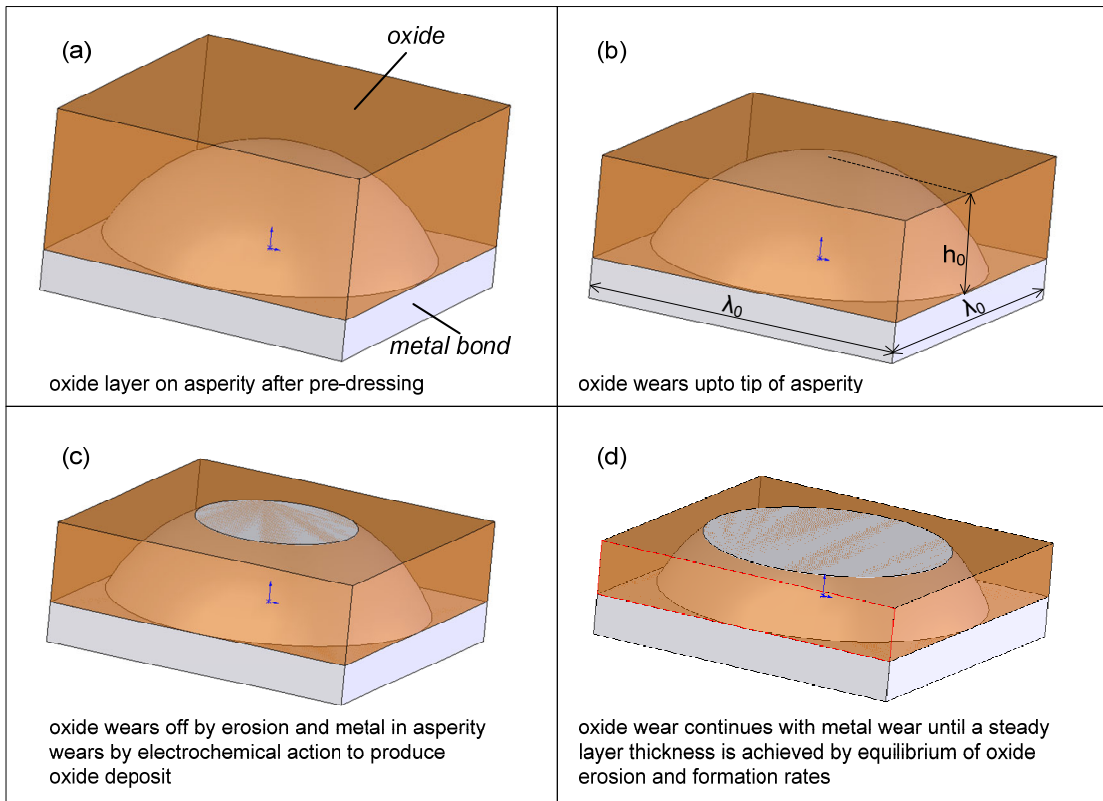
Figure 8.3: Schematic of asperity with adjacent oxide in 3D
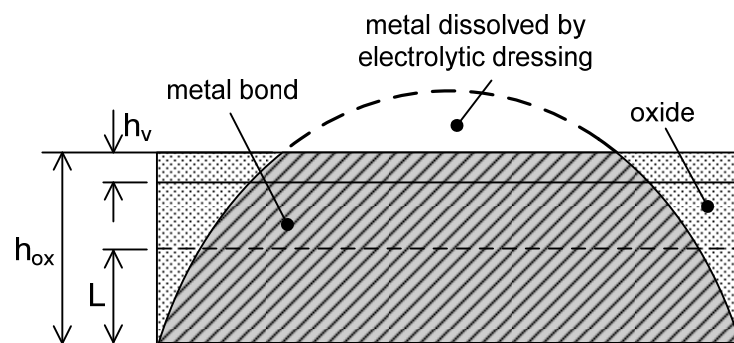
Figure 8.4: Schematic of asperity with adjacent oxide in 2D during erosion

The oxide at any point of time is present upto a height denoted by the variable h_{ox} which is equal to the truncated asperity height. It is important to note that the oxide volume present upto the *height h_{ox}* of the asperity is not equal to the *layer thickness, L,* of the oxide. The 'layer' signifies an average value of the oxide distribution over the

control area. *L* shown in Figure 8.4 signifies the layer thickness obtained from the total volume of oxide of height h_{ox}, present in the control area and the variables are related with the Eqn. 8.4.

$$LA_0 = h_{ox}A_0 - V_{asp} \tag{8.4}$$

Erosion of the oxide from the interstitial sites between the asperities takes place by the interaction of the grinding chips, such that the volume of chips displaces the material off the top of the control area height h_{ox}. The generation rate of grinding chips is determined by the material removal per rotation, m_r, given by Eqn. 7.12. So, the volume $m_r b$ of work material is removed by the entire wheel surface which has the area of πDb (where b is the width of the grinding wheel, and D its diameter). The volume of grinding chips generated by the control area per rotation of the wheel is V_v, is therefore given by Eqn. 8.5.

$$V_v = \frac{m_r A_0}{\pi D} \tag{8.5}$$

This volume of grinding chips is responsible for erosion of the oxide and compression of the metallic asperity. So, the average thickness of chips volume acting on the asperity, h_v, is obtained from Eqn. 8.6 (Figure 8.4).

$$h_v = \frac{V_v}{A_0} = \frac{m_r}{\pi D} \tag{8.6}$$

The value of h_v is within 5 nm and so the compressive load exerted on the truncated asperity is elastic and does not affect the oxide erosion process or deform the asperity shape significantly. The new height of oxide, $h_{ox,i+1}$ after $(i+1)^{th}$ rotation is therefore:

$$h_{ox,i+1} = h_{ox,i} - h_v \tag{8.7}$$

8.4 Electrolytic Dressing

The electrochemical formulation is based on the entire wheel surface and not just on the control area used in the model. So, the oxide *layer thickness*, *L*, is required for solving the dressing equations. The average thickness of the layer, *L* (Figure 8.4), is found from volume calculation of the oxide, V_{ox}, from Eqn. 8.8 (derived from Eqn. (8.4)).

$$LA_0 = V_{ox} = (h_{ox} - h_v)A_0 - \frac{\pi}{4} \int_0^{h_{ox} - h_v} \lambda(\eta)^2 \, d\eta \tag{8.8}$$

Dressing current is calculated by putting *L* into Eqn. 7.6. The current efficiency, η, is calculated from Eqn. 7.5 and the increase in oxide layer thickness, l_e, is calculated from Eqn. 7.4. The new layer height h_{ox}, is then obtained from iterative solution of Eqn. 8.9, i.e. the reverse solution for Eqn. 8.8.

$$(L + l_e)A_0 = h_{ox}A_0 - \frac{\pi}{4} \int_0^{h_{ox}} \lambda(\eta)^2 \, d\eta \tag{8.9}$$

Wheel wear per rotation, is obtained from the amount of metal dissolved, which in turn is obtained from increase in oxide layer thickness l_e, and PBR *c*, so that the WWR is given by Eqn. 8.10 (*S* is the grinding wheel rpm).

$$WWR = \frac{60 l_e}{Sc} \tag{8.10}$$

8.5 Solution of Equations

The coefficients of the equations are first determined through observations of the experimental system. It is observed in Figure 7.7 that the average base of the asperities on the grinding wheel surface profile is approximately 250µ, and the

average asperity height is approximately 25μ. Thus, $\lambda_0 = 250\mu$ and $h_0 = 25\mu$. Diameter of the grinding wheel used in the experiments is 75mm, so that, *D = 75 mm*. The coefficients for the electrochemical formulations have been discussed in Sections 7.4 and 7.6.
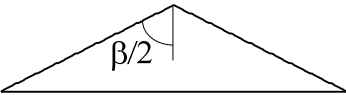
Several types of asperity geometry are chosen for the formulation and their results compared. They are:
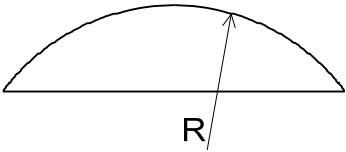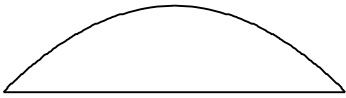
   i. Conical

  ii. Spherical

 iii. Parabolic

 iv. Bell Curve (shape of normal distribution)

The Eqns. 8.2 and 8.3 for the different geometry is given in Table 8.1.

As mentioned before, the asperity height h_0, and base dimension λ_0, are determined from the profile of the grinding wheel surface. These are approximate values and can cause some variation of the results and so the model is evaluated for different values of λ_0 *and* h_0, viz. $\lambda_0 = 200, 250 \& 300\mu$ and $h_0 = 20, 25$ and 30μ, to observe this variation of the results.

Table 8.1: Relations for different asperity geometries

Geometry	Relations
Conical	$\tan(\beta/2) = \dfrac{\lambda_0}{2h_0}$ $\lambda(h) = 2h\tan(\beta/2)$ $V_{asp}(h) = \dfrac{\pi}{3}h^3 \tan^2(\beta/2)$

Spherical	$R = \dfrac{1}{2h_0}\left(h_0^{\,2} + \dfrac{\lambda_0^{\,2}}{4}\right)$
	$\lambda(h) = 2\sqrt{(R - h_0 + h)^2 + R^2}$
	$V_{asp}(h) = \pi\left(\left(2h_0 R - h_0^{\,2}\right)h - (R - h_0)h^2 - \dfrac{1}{3}h^3\right)$
Parabolic	$\lambda(h) = \lambda_0\sqrt{\dfrac{h_0 - h}{h_0}}$
	$V_{asp}(h) = \dfrac{\pi\lambda_0^{\,2}}{4h_0}\left(h_0 h - \dfrac{1}{2}h^2\right)$
Bell Curve	$z = \dfrac{\lambda}{\lambda_0},\ \dfrac{h}{h_0} = \dfrac{1}{\sigma\sqrt{2\pi}}\exp\left(-\dfrac{(z - \mu)^2}{2\sigma^2}\right) = F\left(\dfrac{\lambda}{\lambda_0}\right)$
	$\lambda(h) = \lambda_0 F^{-1}\left(\dfrac{h}{h_0}\right)$
	$V_{asp}(h) = \dfrac{\pi\lambda_0^{\,2} h_0}{4}\int_0^h \left(F^{-1}(\eta/h_0)\right)^2 d(\eta/h_0)$

The simulation procedure for the model is shown in the form of a flow chart in Figure 8.5 and simulation results for wheel wear and dressing current are shown in Figure 8.6 and Figure 8.7. Variation of theoretical WWR for the stated h_0 and λ_0 is shown in Figure 8.6 for parabolic asperity under specific grinding conditions. It can be seen that the WWR increases slowly until it reaches a final steady value due to equilibrium of the oxide erosion and formation rates. Initial layer thickness is assumed zero for this computation.

The model is solved with the different asperity shapes for a particular set of ELID grinding conditions, with initial layer thickness of 25μ, and the simulated current is

shown in Figure 8.7. It is seen that the bell shaped asperity reaches the steady state sooner than the others. The current characteristics are almost same for the parabolic and spherical asperities because they have similar shapes. The conical asperity has the highest steady state value. This steady state is attained by equilibrium of oxide erosion and formation rates.
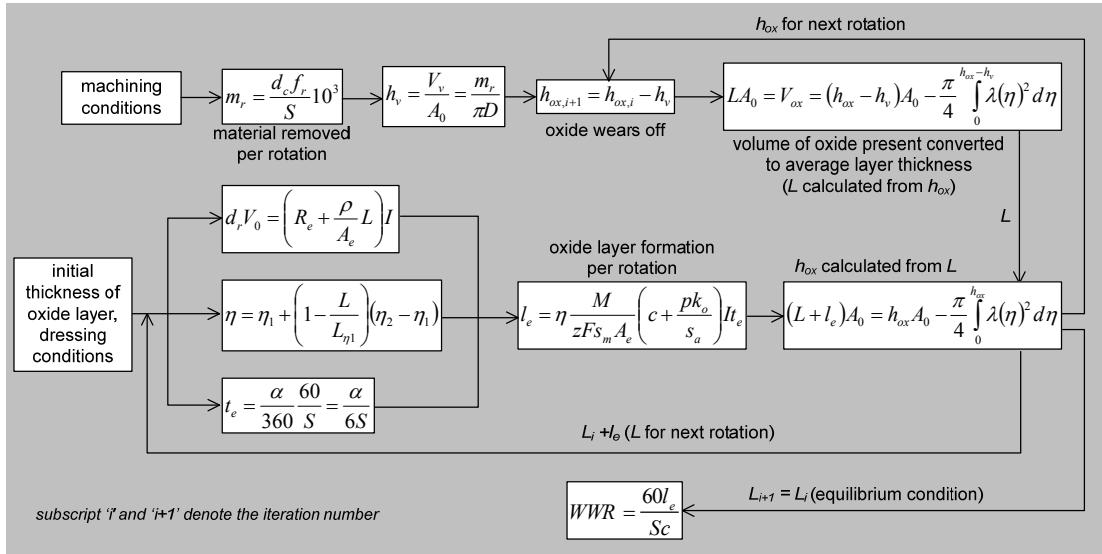
Figure 8.5: Algorithm for solution of analytical model
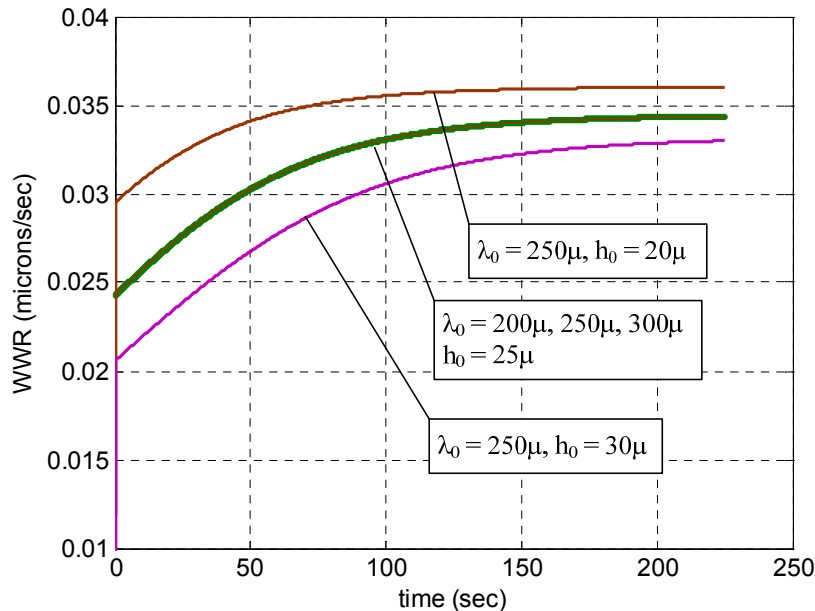
Figure 8.6: Variation of simulated WWR with time, for different h_0 and λ_0 values, for parabolic asperity shape with $d_c=3 \ \mu$, $S=7.9 \ m/s$, $f_r=640 \ mm/min$, $d_r=75\%$, $V_0=100V$

The concept of equilibrium can be understood from the dependence of erosion rate and formation rate on the existing volume of oxide. The volume of oxide removed per rotation of wheel, V_{ov}, (shown by cross-hatched area in Figure 8.8) i.e. by skimming h_v thickness off the top of the oxide is given by Eqn. 8.11.

$$V_{ov} = h_v A_0 - \frac{\pi}{4} \int_{h_{ox}-h_v}^{h_{ox}} \left(\lambda(h)\right)^2 dh \tag{8.11}$$

The value of h_{ox} is in the range of microns, whereas the value of h_v is within a 5nm. So, the Eqn. 8.11 reduces to Eqn. 8.12.

$$V_{ov} = h_v A_0 - \frac{\pi}{4} \left(\lambda(h_{ox})\right)^2 h_v \tag{8.12}$$
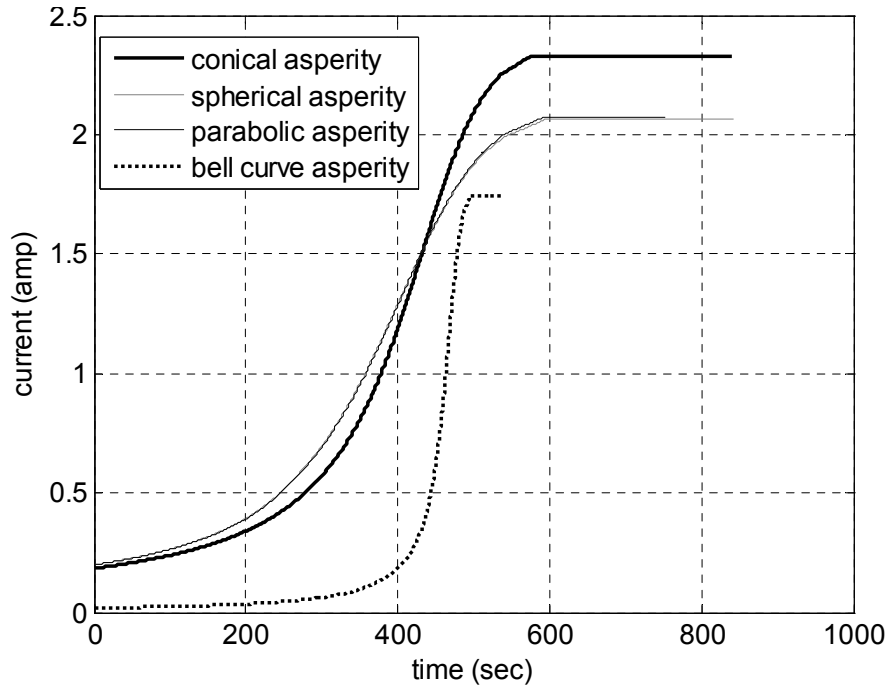
Figure 8.7: Comparison of dressing current for different asperity shapes for $d_c=3\ \mu$, $S=7.9\ m/s$, $f_r=500\ mm/min$, $d_r=50\%$,

Since λ is a decreasing function of h, V_{ov} becomes an increasing function of h, i.e. the volume of oxide eroded increases with h_{ox}. On the other hand, oxide formation rate, l_e, depends on dressing current (Eqn. 7.4), which in turn decreases with increasing oxide

layer thickness L (Figure 8.8) obtained from h_{ox} with Eqn. 8.8. So, l_e decreases with increasing h_{ox}. Eventually, solution of increasing oxide erosions equation and the decreasing oxide formation equations generates an equilibrium condition, i.e. when l_e (Eqn. 7.4) becomes equal to the oxide removed per rotation.
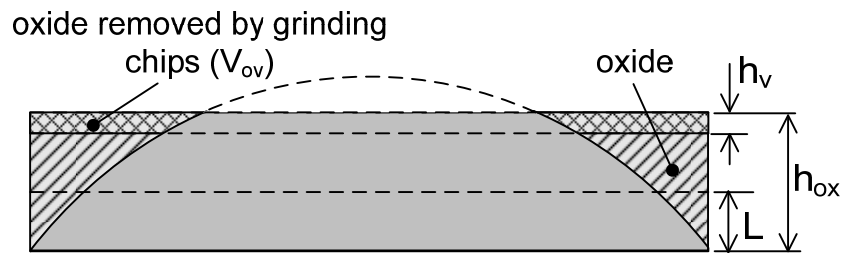
Figure 8.8: Comparison of volume of oxide eroded per rotation of wheel from different volumes of existing oxide layer for the same MRPR

It can also be seen that the WWR varies with the asperity height, h_0, but variation with the control area dimension λ_0 is insignificant. This is desirable because h_0 dictates the oxide layer thickness which controls the current and wheel wear, but the control area for the simulation is not supposed to have a significant effect on the results. In the next chapter, the model is used to predict wheel wear with the different asperity shapes and is compared with several kinds of experimental results and the results of the semi-empirical model.

8.6   Concluding Remarks

An analytical model for simulating oxide erosion is developed based on a control area containing an average asperity on the wheel surface. Oxide is present in the interstitials between the asperities and its rate of wear is controlled by the volume of grinding chips produced. Due to the geometry of asperity, rate of oxide erosion decreases and formation rate increases with the depth of oxide present and equilibrium is finally reached between formation and erosion (steady state) with

continued grinding. Asperity geometries of bell curve, parabolic, spherical and conical are used in the model. Upon solution of the model in conjunction with the dressing model derived in the last chapter, it is seen that variation of the control area of the asperity does not have significant effect on the results.

Chapter 9

CASE STUDIES

The semi-empirical model and the analytical models for different asperity shapes are evaluated with three kinds of experiments:

i.   Wheel wear measurement experiments with continuous grinding passes (without idle strokes/passes)

ii. Wheel wear measurement experiments where grinding passes have intermediate idle passes for additional wheel dressing

iii. Profile estimation experiments where actual material removed is measured from the ground surface and compared with corresponding values calculated from wheel wear estimated from the models

9.1   Continuous ELID Grinding

Continuous ELID grinding is carried out in several passes for material removal along the surface of a circular BK7 glass blank (Section 3.2.3). The steady state WWR and dressing current simulated from the models and the measured values are shown in the bar diagram in Figure 9.1 and Figure 9.2 respectively. The erosion constant for the semi-empirical model was evaluated for 12 experiments in Section 7.7, and is evaluated with 7 additional experimental results in this study. The semi-empirical model has best match with experimental values of WWR and dressing current, followed by analytical models with parabolic and spherical shape asperity. The greatest differences between experimental and simulated values are for the conical and bell curve shaped asperities.
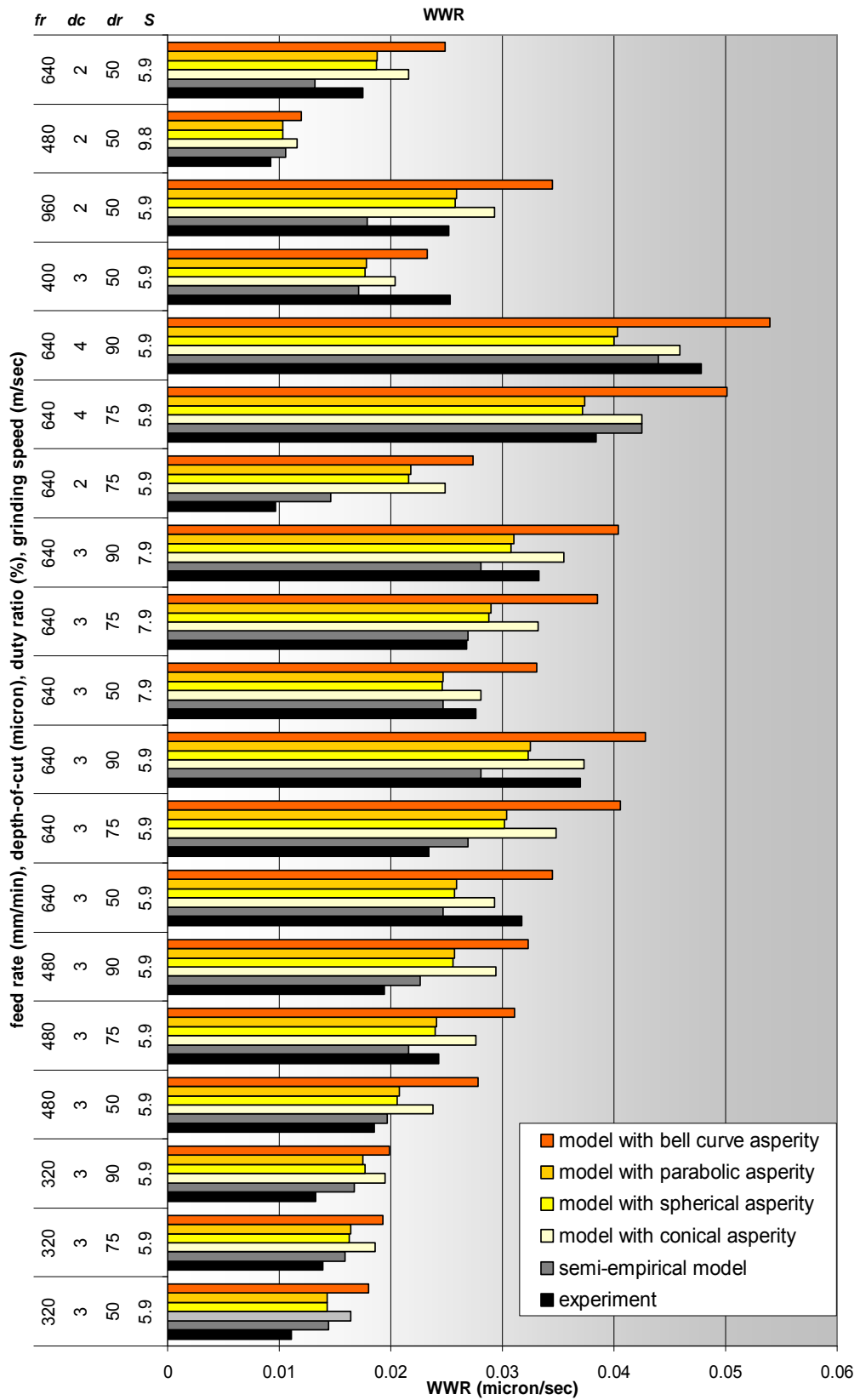
Figure 9.1: Comparison of experimental steady stage WWR for continuous grinding experiments with the simulated values from the different models
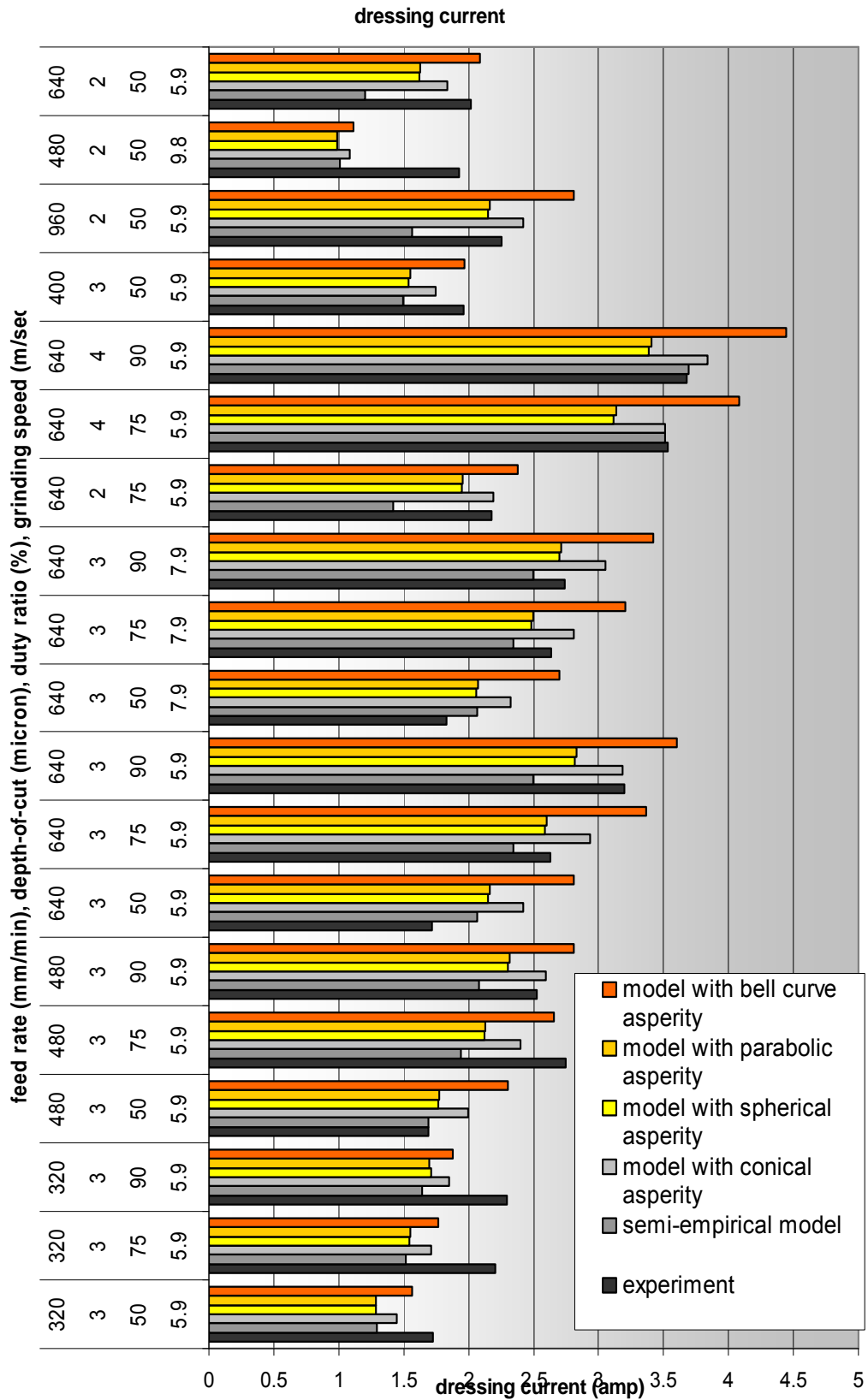
Figure 9.2: Comparison of experimental steady stage dressing current for continuous grinding experiments with the simulated values from the different models

9.2 ELID Grinding with Idle Passes

This section compares the simulated results with a different kind of ELID grinding in order to test the versatility of the models. ELID grinding experiments for wheel wear measurement are performed on circular BK7 glass blanks so that the locus of the wheel pass is in a rectangular scheme (experiments described in Section 6.2.5). The steady values of WWR simulated from different models are evaluated for the experimental conditions and compared with experimental values in the bar diagram in Figure 9.3. The figure shows that the minimum error with the experimental values is for the semi-empirical model, followed by the analytical model with spherical and parabolic asperity shapes.
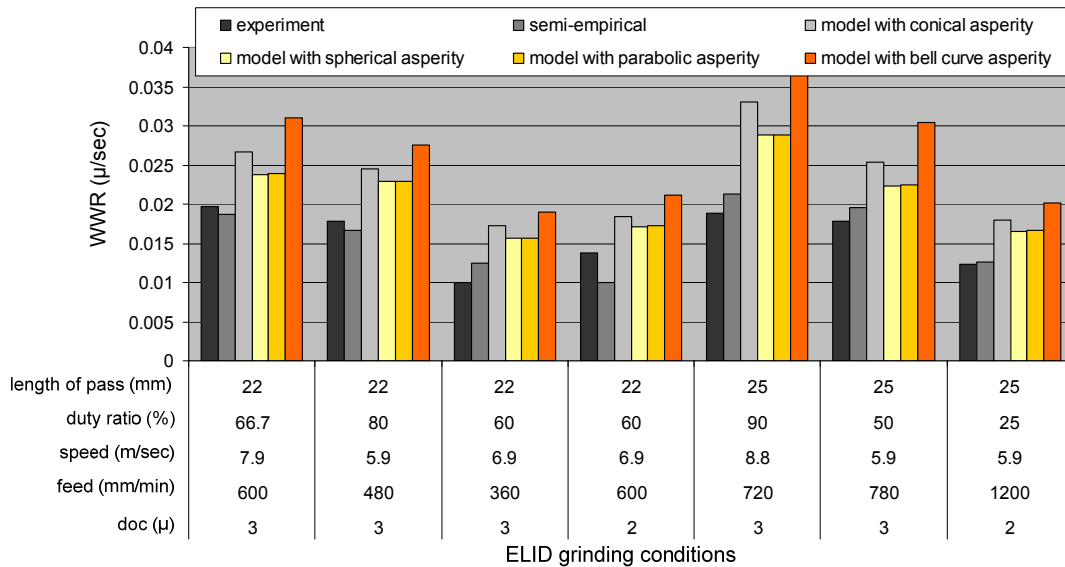
Figure 9.3: Comparison of experimental wheel wear rate for grinding incorporating idle passes, with the simulated values from the different models

9.3 Profile Estimation

During grinding, wheel wear produces a difference between the desired depth-of-cut and the actual depth-of-cut, thereby producing a difference between the desired profile and the actual profile of the workpiece. In this study, a series of experiments

are conducted to surface grind a BK7 glass using #1200 wheel, in multiple passes. The ground glass profile is then measured to obtain the total depth of material removal (MR). The estimated wheel wear is calculated with the models from the ELID grinding conditions. The estimated depth of MR is then obtained by subtracting the wheel wear estimate from the desired depth of MR. the model is validated by comparing the estimated MR with actual MR value measured from experiments.
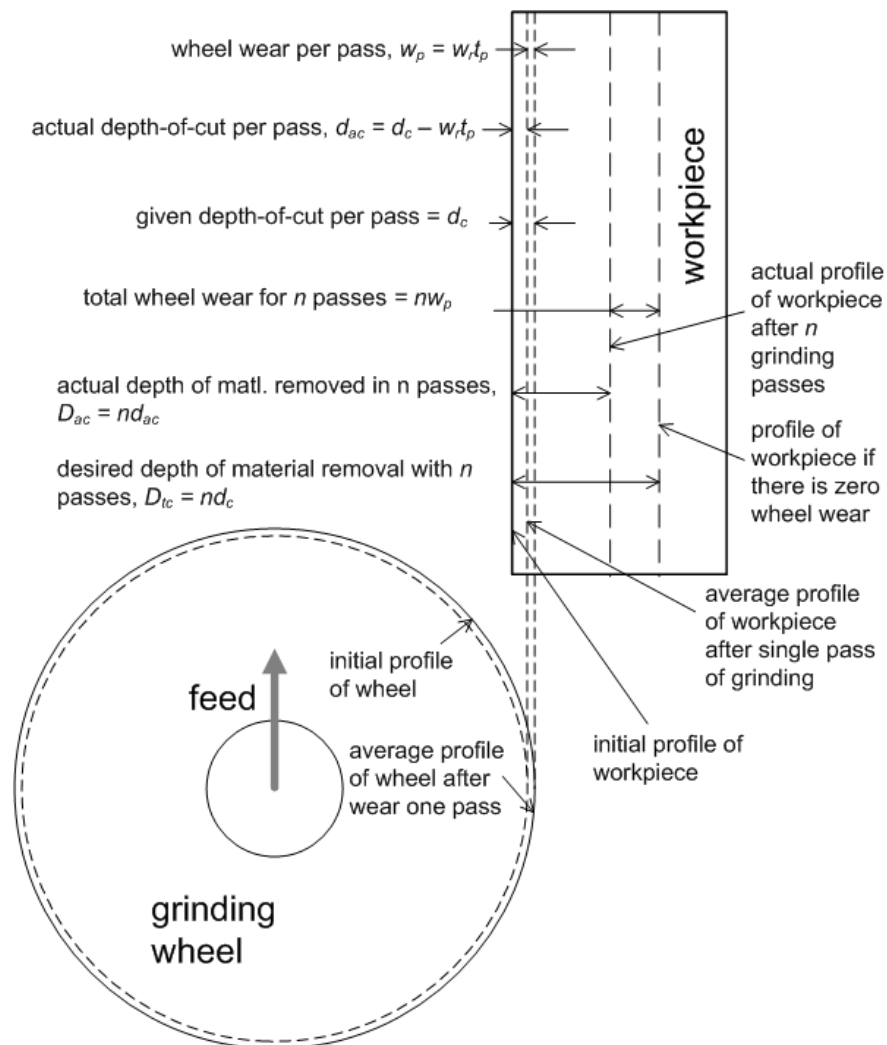
Figure 9.4: Schematic depicting the influence of wheel wear on ground profile

These experiments are carried out with 5 minutes of pre-dressing time so that the transient stage is minimized. The depth of MR from the ground profiles are measured with respect to a reference surface on the workpiece itself, with the Taylor Hobson

Ultra Surface 396, to obtain the actual depth of material removed. Calculation of the estimated depth of material removed from the estimated wheel wear rate is as follows.

Wheel wear rate, w_r, is estimated with (i) the semi-empirical grinding model, (ii) the analytical model with conical asperity, (iii) spherical asperity and (iv) parabolic asperity for the individual experimental conditions. The total wear per pass, w_p, is then calculated from the grinding time per pass, t_p and the wheel wear rate, w_r (Eqn. 9.1). The calculation of estimated depth of MR from the model is explained with the schematic shown in Figure 9.4.

$$w_p = t_p w_r \tag{9.1}$$

So, the actual depth-of-cut per pass, d_{ac}, is obtained from the given depth-of-cut, d_c, and wear per pass, w_p.

$$d_{ac} = d_c - w_p \tag{9.2}$$

For a total of n passes, the given total depth-of-cut D_{tc} is given by Eqn. 9.3.

$$D_{tc} = n d_c \tag{9.3}$$

Therefore, the actual depth of MR for n grinding passes, D_{ac}, is given by Eqn. 9.4.

$$D_{ac} = n d_{ac} \tag{9.4}$$

Tables 9.1, 9.2, 9.3 and 9.4 show the in values obtained from the aforementioned equations from the semi-empirical model, analytical model with conical, spherical and parabolic asperity shapes respectively. The unit of d_c, D_{ac}, D_{tc} and w_p are in microns, w_r is in micron/sec, grinding speed S is in m/sec, f_r in mm/min, t_p in sec and d_r in %. Finally, comparison of the actual depth of MR with the values estimated from the different models is shown in Figure 9.5. Subscripts 1, 2, 3 and 4 are assigned to the variables calculated from the respective models.

Average estimation error for a model is calculated for the current and WWR values with Eqn 9.5, where V_{ex} represents experimental value, V_{sim} is the simulated value, E is the error and n is the number of experiments.

$$E = \frac{1}{n}\sum \frac{|V_{ex} - V_{sim}|}{V_{ex}} \tag{9.5}$$

The semi-empirical model has a close match of 5.47% with the experimental values, followed by the analytical models with spherical and parabolic asperity shapes at 11.75% and 11.73% respectively. The error for the model with conical asperity is maximum at 14.75%.

Table 9.1: Calculation of estimated depth-of-cut with semi-empirical model

	S	d_c	f_r	d_r	w_{r1}	t_p	w_{p1}	n	D_{tc}	D_{ac1}
1	5.89	2	400	40	0.0088	63.75	0.561	26	52	37.41
2	6.87	2	600	60	0.0132	39.5	0.5214	26	52	38.44
3	7.85	3	400	75	0.0188	48.5	0.9118	18	54	37.59
4	8.84	3	200	60	0.0106	73.2	0.7759	18	54	40.03
5	4.91	2	200	40	0.0053	61.23	0.3245	26	52	43.56

Table 9.2: Calculation of estimated depth-of-cut with analytical model with conical asperity shape

	S	d_c	f_r	d_r	w_{r2}	t_p	w_{p2}	n	D_{tc}	D_{ac2}
1	1500	2	400	40	0.0124	63.75	0.7905	26	52	31.45
2	1750	2	600	60	0.0207	39.5	0.8177	26	52	30.74
3	2000	3	400	75	0.0211	48.5	1.0234	18	54	35.58
4	2250	3	200	60	0.0088	73.2	0.6442	18	54	42.41
5	1250	2	200	40	0.0056	61.23	0.3429	26	52	43.08

Table 9.3: Calculation of estimated depth-of-cut with analytical model with spherical asperity shape

	S	d_c	f_r	d_r	w_{r3}	t_p	w_{p3}	n	D_{tc}	D_{ac3}
1	1500	2	400	40	0.0108	63.75	0.6885	26	52	34.1
2	1750	2	600	60	0.018	39.5	0.711	26	52	33.51
3	2000	3	400	75	0.0185	48.5	0.8973	18	54	37.85
4	2250	3	200	60	0.0118	73.2	0.8638	18	54	38.45
5	1250	2	200	40	0.0075	61.23	0.4592	26	52	40.06

Table 9.4: Calculation of estimated depth-of-cut with analytical model with parabolic asperity shape

	S	d_c	f_r	d_r	w_{r4}	t_p	w_{p4}	n	D_{tc}	D_{ac4}
1	1500	2	400	40	0.0109	63.75	0.6949	26	52	33.93
2	1750	2	600	60	0.0181	39.5	0.715	26	52	33.41
3	2000	3	400	75	0.0186	48.5	0.9021	18	54	37.76
4	2250	3	200	60	0.0117	73.2	0.8564	18	54	38.58
5	1250	2	200	40	0.0074	61.23	0.4531	26	52	40.22
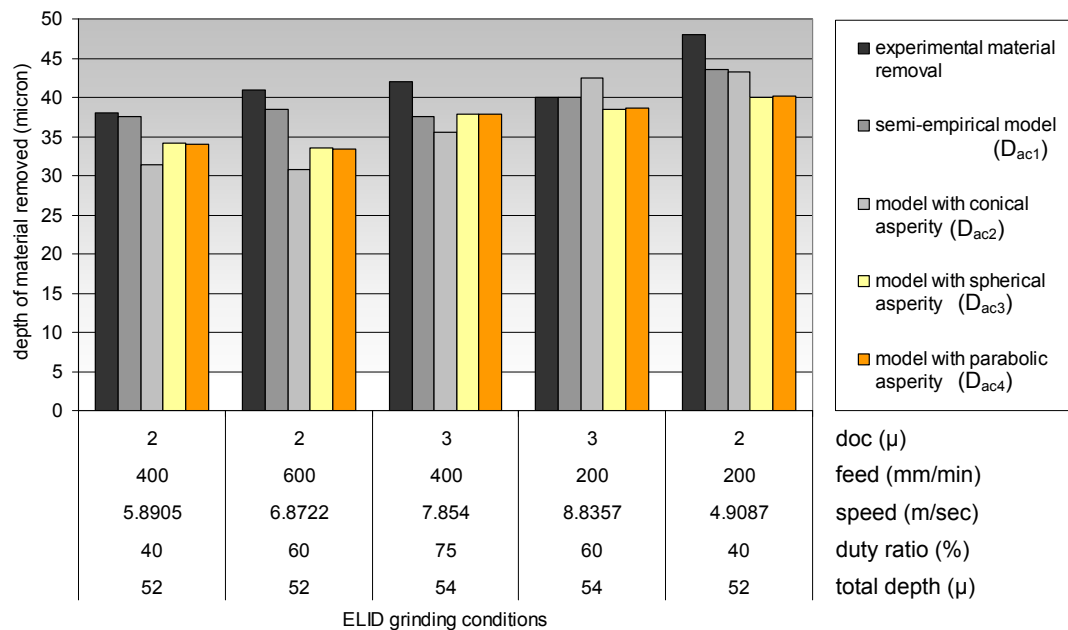
Figure 9.5: Achieved and estimated depth of material removal for given depth

9.4 Discussions

Comparison of experimental and simulation results show that the semi-empirical model has the closest match with the experimental values. The analytical models with spherical and parabolic asperity shapes have the second best agreement with the experimental values. The reason is stated as follows.

Machine accuracy plays an important role in wheel wear as well as profile correctness of ground component. Error in machine axis positioning increase or decrease the desired machining conditions producing uneven wheel wear. So, wheel wear measured during experiments have the some inherent error due to machining inaccuracy. The semi-empirical model being partly derived from the experimental results have an inherent compensation for machining inaccuracy. This is absent in the analytical models and hence the semi-empirical model has better agreement than analytical models.

Further comparison of the simulation results show the wear rate and current obtained from the conical and bell curve asperity shapes are higher than that of the spherical and parabolic shapes. The reason is as follows. The cross-sections of the asperities along with the adjoining oxide layer (shown in the hatched area) is shown in Figure 9.6. It shows the volume of oxide for the conical asperity will be higher than that of the parabolic and spherical shapes. Consequently, the rate of volume of oxide removed by the grinding chips (represented by the cross-hatched area) will also be higher for the conical asperities. Therefore, the rate of oxide wear is higher for conical and bell curve shaped asperities. In the semi-empirical model, the oxide erosion is modeled with the empirically determined erosion constant and hence has a better match than the analytical models.
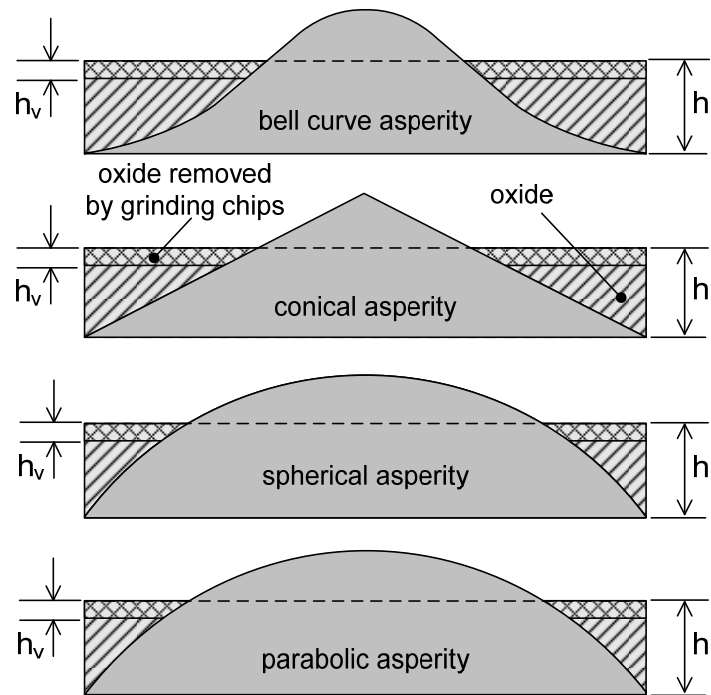
Figure 9.6: Cross-section of different asperity shapes with adjacent oxide layer

It is also interesting to note that the error in current estimation is lower than the WWR estimation error. Ideally, WWR should be proportional to the dressing current (Eqn. 7.4), but is not so in actuality. The oxide layer breaks and reforms in discrete steps. So the wear measurement becomes inherently erroneous when the measurement is taken when the oxide layer has just broken off or is at the maximum thickness and just about to break off. This error is minimized when the measurement of the wheel wear is carried out from the ground surface because the periodic variations are averaged. This is seen for the profile estimation experiments, in Figure 9.5, which has better agreement with experimental values.

9.5   Concluding Remarks

The chapter has compared results from the different models amongst three types of experiments:

    i.   Continuous ELID grinding

ii. ELID grinding with idle passes

iii. Profile estimation experiments

The semi-empirical model derived from some of the continuous grinding experiments has the best fit with all the experimental results. The analytical models with the spherical and parabolic shaped asperities have the second best results. The profiles of the ground surface estimated from the wheel wear models have the lowest error with the experimental results.

Chapter 10

CONCLUSIONS, CONTRIBUTIONS AND FUTURE WORK

10.1 Conclusions

The objective of the thesis is to carry out investigations on wheel wear of ELID grinding as it is of importance for process improvements. The study is started with investigations on the *electrolytic behavior* and *electrical properties of the electrolyte* flow system, which is then used to find the governing equations of *electrolytic dressing*. *Experimental examination of wheel wear* is then carried out and finally, the dressing formulation is combined with a simple model of grinding wear to find the overall *model for dressing current and wheel wear* for ELID grinding. The following conclusions can be drawn from the entire study.

10.1.1   Studies on Impedance of Electrolyte

Investigation of the governing mechanism of ELID and the relevant electrical properties of the electrolyte has revealed the following:

- Surface and concentration overpotentials are negligibly small compared to the high potential difference applied during ELID. The current and applied potential during electrolytic dressing can be related with Ohm's Law.

- Gas generation from the cathode, which is proportional to dressing current, reduces the electrolyte conductivity, but the reduction is marginal because the flow rate of the electrolyte is very high.

- Impedance of the electrolyte is purely resistive for flow conditions relevant to ELID. It decreases with reducing electrode gap, increasing flow rate and reducing grinding speeds.

- Electrolysis carried out with a very small electrode gap (200μ or smaller) and no oxide layer leads to spark-erosion of the bond (ED truing mechanism).

- Current response of electrolyte for square pulsed voltage input is a trapezoidal wave form. The stray impedance of the wires is found to be responsible for the rise and fall times of the wave form and is hence constant for a particular setup, irrespective of pulse ON time, or flow conditions. However, the wave form becomes triangular for ON time less than the rise time.

10.1.2 Investigations on Electrolytic Dressing

Theoretical and experimental investigations on the oxide formation dynamics during the electrolytic dressing process has lead to the following conclusions:

- Equations are formulated which relate oxide layer formation and dressing current with power supply inputs and electrolyte flow conditions.

- Dressing experiments are performed for measurement of oxide layer thickness and dressing current. The dressing process shows the initial and the post-initial

stages of oxide development. The initial stage has a very rapid increase of layer thickness and rapid decrease of dressing current. Development of the oxide layer is poor in the post-initial stage.

- Experimental dressing current pattern matches with the theoretically derived pattern. Experimentally obtained oxide layer thickness agrees with the theoretical result for the initial 5 to 7 mins of pre-dressing.

10.1.3 Experimental Study of Wheel Wear

Examination of the wheel wear is carried out by performing ELID grinding experiments and the following are observed:

- ELID grinding, with brittle and ductile modes are carried out after pre-dressing and show initial and steady regions of operation. The initial region has the effect of the pre-dressed layer, when the grinding forces and dressing current keep increasing up to a threshold level where steady grinding starts.

- Steady grinding in ductile model produces periodic variations of force and dressing current, which is absent in brittle mode grinding experiments.

- Pitting and/or sparking is observed on the grinding wheel when the dressing rate is poor compared to the erosion rate of the oxide. Based on the onset of this phenomenon, a criterion is developed to segregate the sufficiently dressed ELID grinding conditions from the insufficiently conditions.

- Average wheel wear rate during steady ductile mode grinding with sufficient dressing rate is found to have a correlation with input parameters. An empirical function is defined, from the input parameters, with which the wheel wear rate variation is found to be approximately linear.

- Ground surface finish generated by the different grinding conditions is investigated and an idle pass incorporated in continuous grinding operation produces better surface finish.

10.1.4 ELID Grinding Models

10.1.4.1 Semi-Empirical Model

Ideally, electrochemical metal dissolution is the governing principle of wheel wear in ELID grinding. Electrochemical action depends on the oxide layer thickness which is eroded off due to grinding. Analytical model for electrolytic dressing and an empirical relation for oxide erosion are formulated and solved simultaneously to get the semi-empirical model. The model has one coefficient called the erosion constant which is determined empirically and varies with work material and grinding wheel type. Other coefficients of the model are determined from grinding setup and different types of non-grinding experiments.

The model is verified with brittle mode and ductile mode ELID grinding experiments. Simulation results show that the dressing current reaches a steady value after the pre-dressed layer is worn off during the transient stage of grinding. When grinding is initiated after pre-dressing with a thick layer of oxide, the erosion rate is very high and dressing rate is low. As grinding continues, reducing layer thickness increases dressing current and hence the oxide formation rate, until the formation and erosion rates reach equilibrium. Theoretically, this equilibrium is in a steady stage with constant value. But in practical cases the erosion takes place in discrete steps and gives periodic variations in dressing current. The simulated values of steady state current and wheel wear rates have a good agreement with the average experimental values.

10.1.4.2 Analytical Model

The grinding wheel has a rough surface with metallic asperities bigger than the average asperity size. In the analytical model for oxide erosion, this surface is represented by a control area and the real asperities are represented by an average asperity on the control area. Oxide is present in the interstitials between the asperities and its rate of wear is determined by the volume of grinding chips produced by the control area. When grinding starts with a high volume of oxide, the erosion rate is higher than the formation rate. Reduced oxide deposit promotes electrolysis and oxide formation rate increases. Increasing oxide formation rate and reducing erosion rate eventually reach equilibrium. The model is solved in conjunction with dressing model for different asperity geometries of bell curve, parabolic, spherical and conical shapes. Steady state values of dressing current and wheel wear rate simulated from the model have good match with the experimental values.

10.1.4.3 Case Studies

The results from the analytical and semi-empirical models are compared with three different types of experiments:

    i.   Continuous ELID grinding

    ii. ELID grinding with idle passes

    iii. Work Profile estimation experiments

The semi-empirical model derived from some of the continuous grinding experiments has the best fit with the experimental results. The analytical models with the spherical and parabolic shaped asperities have the second best results. The profiles of the ground surface estimated from the wheel wear models have the lowest error of the three sets of experiments.

10.2 Contributions

As such, all the conclusions enumerated in the Section 10.1 are exclusive findings previously unreported. The important contributions of this research in ELID grinding are as follows:

- Properties of electrolyte are investigated to find its response to applied potential is that of a resistor. This finding simplifies the understanding of the process and can be applied in various ways. One of the corollaries for this finding is the effect of very low pulse ON time. The increase and decrease time of the trapezoidal current pulse depends on the stray inductance in the wiring to the ELID electrodes. If pulse ON time is less than the increase time (6μ-sec in this study), the charge flow reduces because the current pulse type becomes triangular and the working voltage reduces. When low ON time is used (general practice is 2 to 4μ-sec), the wiring should be designed so that the increase time is smaller than the pulse ON time.

- The mechanism for oxide formation is theorized and equations are formulated so that the relation with input conditions is clearly defined. This theory can be applied to control electrolysis, so that desired rate of dressing can be achieved.

- Quantitative studies on wheel wear of ELID grinding has been absent because of various literatures on fundamental works concluding instability and uncertainty in the process. It is found in the study that predictability of wheel wear is present in the steady grinding phase where the rate of electrochemical action and oxide erosion, though in discrete steps, are in equilibrium and a *stable layer* of oxide exists. A benchmark function, ELID wear factor, is defined from grinding and dressing parameters to estimate wheel wear rate.

- A semi-empirical and an analytical model are developed for simulating wheel wear rate and dressing current during ELID grinding which are in good agreement with results of different kinds of experiments.

- The actual volume of material removal can be estimated by compensating the machining conditions with the wheel wear estimated from the models.

10.3 Future Work

There is no prior work on wheel wear estimation in ELID grinding. Wheel wear is responsible for achieving profile accuracy of ground components. Profile accuracy of ELID ground components has much room for improvement and so there are many possibilities for development from this research. Some of the possibilities are listed below:

- The profile experimentally achieved after wheel wear is estimated from the models. Further work can be performed in this area to improve the profile accuracy of ground surfaces by compensating the machining conditions with the estimated wheel wear rate. This way the desired profile can be achieved with lesser error.

- The theory for wheel wear being established, relation between dressing current and wheel wear is clearly defined. Dressing current can be monitored and processed to obtain the wheel wear rate, thereafter compensate the grinding parameters so that profile accuracy of machined component can be enhanced. This can be a continuous operation, unlike the intermittent time-consuming method that is presently used and is based on profile feedback of ground surface.

- Composition of grinding wheel and electrolyte can be modified to produce an oxide layer of stable and predictable properties. This will enable easy prediction of the process so that it can be manipulated to obtain desired results.

BIBLIOGRAPHY

[1] D.J. Bodin, T.O. Mason, Britannica Online Encyclopedia, Abrasive Materials, www.britannica.com/EBchecked/topic/1615/abrasive, (2009)

[2] R.S. Woodbury, Studies in the History of Machine Tools, The MIT Press, London, 1972.

[3] I.D. Marinescu, M. Hitchiner, E. Uhlmann, W.B. Rowe, I. Inasaki, Handbook of Machining with Grinding Wheels, CRC Press, Boca Raton, London, New York, 2007.

[4] T.G. Bifano, T.A. Dow, R.O. Scattergood, Ductile-Regime Grinding: A New Technology for Machining Brittle Materials, J. Eng. Ind. 113(2) (1991) 184-189.

[5] L. Yin, H. Huang, K. Ramesh, T. Huang, High Speed Versus Conventional Grinding in High Removal Rate Machining of Alumina and Alumina-Titania, Int. J. Mach. Tools and Manuf. 45(7-8) (2005) 897-907.

[6] Y. Zhou, M. Atwood, D. Golini, M. Smith, P.D. Funkenbusch, Wear and Self-Sharpening of Vitrified Bond Diamond Wheels During Sapphire Grinding, Wear 219(1) (1998) 42-45.

[7] J. Webster, M. Tricard, Innovations in Abrasive Products for Precision Grinding, CIRP Annals - Manuf. Technol. 53(2) (2004) 597-617.

[8] J.H. Liu, Z.J. Pei, G.R. Fisher, Grinding Wheels for Manufacturing of Silicon Wafers: A Literature Review, Int. J. Mach. Tools and Manuf. 47(1) (2007) 1-13.

[9] I.D. Marinescu, W.B. Rowe, B. Dimitrov, I. Inasaki, Abrasives and Abrasive Tools, *Tribology of Abrasive Machining Processes*, William Andrew Publishing, Norwich, NY, 2004, pp. 369-455

[10] A. Hosokawa, T. Ueda, T. Yunoki, Laser Dressing of Metal Bonded Diamond Wheel, CIRP Annals - Manuf. Technol. 55(1) (2006) 329-332.

[11] E. Westkämper, Grinding Assisted by Nd:Yag Lasers, CIRP Annals - Manuf. Technol. 44(1) (1995) 317-320.

[12] K. Suzuki, T. Uematsu, T. Nakagawa, On-Machine Trueing/Dressing of Metal Bond Grinding Wheels by Electro-Discharge Machining, CIRP Annals - Manuf. Technol. 36(1) (1987) 115-118.

[13] Y. Wang, X.-j. Zhou, D.-j. Hu, An Experimental Investigation of Dry-Electrical Discharge Assisted Truing and Dressing of Metal Bonded Diamond Wheel, Int. J. Mach. Tools and Manuf. 46(3-4) (2006) 333-342.

[14] X. Wang, B. Ying, W. Liu, Edm Dressing of Fine Grain Super Abrasive Grinding Wheel, J. Mater. Process. Technol. 62(4) (1996) 299-302.

[15] N. Ortega, J.A. Sánchez, J. Aranceta, J.A. Marañón, X. Maidagan, Optimisation of Grit Protrusion in the Electro-Discharge Dressing Process of Large Grit Size Cbn Grinding Wheels, J. Mater. Process. Technol. 149(1-3) (2004) 524-529.

[16] H.K. Tönshoff, T. Friemuth, In-Process Dressing of Fine Diamond Wheels for Tool Grinding, Precis. Eng. 24(1) (2000) 58-61.

[17] C. Lan-Rong, J. Yan, H. De-Jin, Dressing of Metal-Bonded Superabrasive Grinding Wheels by Means of Mist-Jetting Electrical Discharge Technology, J. Mater. Process. Technol. 209(2) (2009) 779-784.

[18] R. Murata, K. Okano, C. Tsutsumi, Grinding of Structural Ceramics, Milton C Shaw Grind. Symp. PED 16 (1985) 12.

[19] K. Suzuki, T. Uematsu, T. Yanase, M. Honma, S. Asano, T. Matsuo, Development of a Simplified Electrochemical Dressing Method with Twin Electrodes, CIRP Annals - Manuf. Technol. 40(1) (1991) 363-366.

[20] H. Ohmori, T. Nakagawa, Mirror Surface Grinding of Silicon Wafers with Electrolytic in-Process Dressing, CIRP Annals - Manuf. Technol. 39(1) (1990) 329-332.

[21] D. Kramer, F. Rehsteiner, B. Schumacher, Ecd (Electrochemical in-Process Controlled Dressing), a New Method for Grinding of Modern High-Performance Cutting Materials to Highest Quality, CIRP Annals - Manuf. Technol. 48(1) (1999) 265-268.

[22] E.-S. Lee, J.-D. Kim, A Study on the Analysis of Grinding Mechanism and Development of Dressing System by Using Optimum in-Process Electrolytic Dressing, Int. J. Mach. Tools and Manuf. 37(12) (1997) 1673-1689.

[23] R. Boland. Computer Control and Process Monitoring of Electrolytic in-Process Dressing of Metal Bond Fine Diamond Wheels for Nif Optics. *SPIE Conference on Optical Manufacturing and Testing III*, p. 9Denver, Colorado, 1999).

[24] N. Itoh, H. Ohmori, Grinding Characteristics of Hard and Brittle Materials by Fine Grain Lapping Wheels with Elid, J. Mater. Process. Technol. 62(4) (1996) 315-320.

[25] H. Ohmori, T. Nakagawa, Analysis of Mirror Surface Generation of Hard and Brittle Materials by Elid (Electronic in-Process Dressing) Grinding with Superfine Grain Metallic Bond Wheels, CIRP Annals - Manuf. Technol. 44(1) (1995) 287-290.

[26] H. Ohmori, I. Takahashi, B.P. Bandyopadhyay, Ultra-Precision Grinding of Structural Ceramics by Electrolytic in-Process Dressing (Elid) Grinding, J. Mater. Process. Technol. 57(3-4) (1996) 272-277.

[27] H. Ohmori, T. Nakagawa, Utilization of Nonlinear Conditions in Precision Grinding with Elid (Electrolytic in-Process Dressing) for Fabrication of Hard Material Components, CIRP Annals - Manuf. Technol. 46(1) (1997) 261-264.

[28] B.P. Bandyopadhyay, H. Ohmori, I. Takahashi, Efficient and Stable Grinding of Ceramics by Electrolytic in-Process Dressing (Elid), J. Mater. Process. Technol. 66(1-3) (1997) 18-24.

[29] H.S. Lim, K. Fathima, A. Senthil Kumar, M. Rahman, A Fundamental Study on the Mechanism of Electrolytic in-Process Dressing (Elid) Grinding, Int. J. Mach. Tools and Manuf. 42(8) (2002) 935-943.

[30] M. Rahman, H.S. Lim, K.S. Neo, A. Senthil Kumar, Y.S. Wong, X.P. Li, Tool-Based Nanofinishing and Micromachining, J. Mater. Process. Technol. 185(1-3) (2007) 2-16.

[31] K. Fathima, A. Senthil Kumar, M. Rahman, H.S. Lim, A Study on Wear Mechanism and Wear Reduction Strategies in Grinding Wheels Used for Elid Grinding, Wear 254(12) (2003) 1247-1255.

[32] A. Kumar, H. Lim, M. Rahman, K. Fathima, A Study on the Grinding of Glass Using Electrolytic in-Process Dressing, J. Electron. Mater. 31(10) (2002) 1039-1046.

[33] T. Bifano, R. Krishnamoorthy, H. Fawcett, E. Welch, Fixed-Load Electrolytic Dressing with Bronze Bonded Grinding Wheels, J. Manuf. Sci. Eng. 121 (1999) 8.

[34] Z. Zhu, X. Liu, S. Thangam, Development and Analysis of Foil Electrodes for High Speed Electrolytic in-Process Wheel Dressing, Mach. Sci. Technol. 7(1) (2003) 65 - 81.

[35] R. Pavel, M. Pavel, I. Marinescu, Investigation of Pre-Dressing Time for Elid Grinding Technique, J. Mater. Process. Technol. 149(1-3) (2004) 591-596.

[36] F. Klocke, A. Klink, U. Schneider, Electrochemical Oxidation Analysis for Dressing Bronze-Bonded Diamond Grinding Wheels, Prod. Eng. Res. Dev. 1 (2007) 141-148.

[37] K. Fathima, M. Rahman, A.S. Kumar, H.S. Lim, Modeling of Ultra-Precision Elid Grinding, J. Manuf. Sci. Eng. 129(2) (2007) 296-302.

[38] M. Rahman, A.S. Kumar, H.S. Lim, K. Fathima, Nano Finish Grinding of Brittle Materials Using Electrolytic in-Process Dressing (Elid) Grinding, Sadhana 28(5) (2003) 18.

[39] J. Qian, H. Ohmori, W. Lin, Internal Mirror Grinding with a Metal/Metal-Resin Bonded Abrasive Wheel, Int. J. Mach. Tools and Manuf. 41(2) (2001) 193-208.

[40] N. Itoh, H. Ohmori, S. Moriyasu, T. Kasai, K.-D. Toshiro, B.P. Bandyopadhyay, Finishing Characteristics of Brittle Materials by Elid-Lap Grinding Using Metal-Resin Bonded Wheels, Int. J. Mach. Tools and Manuf. 38(7) (1998) 747-762.

[41] H. Ohmori, K. Katahira, J. Nagata, M. Mizutani, J. Komotori, Improvement of Corrosion Resistance in Metallic Biomaterials Using a New Electrical Grinding Technique, CIRP Annals - Manuf. Technol. 51(1) (2002) 491-494.

[42] H. Ohmori, K. Katahira, T. Naruse, Y. Uehara, A. Nakao, M. Mizutani, Microscopic Grinding Effects on Fabrication of Ultra-Fine Micro Tools, CIRP Annals - Manuf. Technol. 56(1) (2007) 569-572.

[43] T. Saleh, I. Biswas, H.S. Lim, M. Rahman, In-Process Truing of Metal-Bonded Diamond Wheels for Electrolytic in-Process Dressing (Elid) Grinding, Int. J. Precis. Eng. and Manuf. 9(2) (2008) 4.

[44] F. Patham, A. Geiss, R. Rascher, P. Sperber, M. Schinhaerl, E. Pitschke. Design and Development of a Novel Computer Controlled Power Device for Electrical-Assisted Optical Grinding. *Optifab* (Proceedings of SPIE Vol. TD04, 2007).

[45] Z. Zhu, X. Wang, S. Thangam, Simulation and Analysis of Rigid/Foil Electrolytic in-Process Dressing (Elid) Systems for Grinding, J. Manuf. Sci. Eng. 126(3) (2004) 565-570.

[46] M.M. Islam, A. Senthil Kumar, S. Balakumar, H.S. Lim, M. Rahman, Performance Evaluation of a Newly Developed Electrolytic System for Stable Thinning of Silicon Wafers, Thin Solid Films 504(1-2) (2006) 15-19.

[47] T. Saleh, M.S. Rahman, H.S. Lim, M. Rahman, Development and Performance Evaluation of an Ultra Precision Elid Grinding Machine, J. Mater. Process. Technol. 192-193 (2007) 287-291.

[48] M. Sazedur Rahman, T. Saleh, H.S. Lim, S.M. Son, M. Rahman, Development of an on-Machine Profile Measurement System in Elid Grinding for Machining Aspheric Surface with Software Compensation, Int. J. Mach. Tools and Manuf. 48(7-8) (2008) 887-895.

[49] H. Ohmori, K. Katahira, Y. Uehara, T. Suzuki, Y. Pan, T. Sasaki, K. Yoshikawa, Y. Ohi. Development of Desk-Top Cutting/Measuring and Injection Molding Machines for Producing Advanced Microcomponents. *Industrial Technology, 2002. IEEE ICIT '02. 2002 IEEE International Conference on*, pp. 1132-1137 vol.11322002).

[50] N. Itoh, A. Nemoto, T. Katoh, H. Ohmori, Eco-Friendly Elid Grinding Using Metal-Free Electro-Conductive Resinoid Bonded Wheel, JSME Int. J. Ser. C 47(1) (2004) 8.

[51] T. Saito, K. Katahira, H. Ohmori, J. Komotori, M. Mizutani, A. Nemoto, Fabrication of High-Quality Surfaces on Precise Lens Mold Materials by a New Elid Grinding Wheel, *Towards Synthesis of Micro-/Nano-Systems*2007, pp. 315-318

[52] J. Qian, W. Li, H. Ohmori, Cylindrical Grinding of Bearing Steel with Electrolytic in-Process Dressing, Precis. Eng. 24(2) (2000) 153-159.

[53] C. Zhang, H. Ohmori, W. Li, Small-Hole Machining of Ceramic Material with Electrolytic Interval-Dressing (Elid-Ii) Grinding, J. Mater. Process. Technol. 105(3) (2000) 284-293.

[54] H. Ohmori, W. Li, A. Makinouchi, B.P. Bandyopadhyay, Efficient and Precision Grinding of Small Hard and Brittle Cylindrical Parts by the Centerless Grinding Process Combined with Electro-Discharge Truing and Electrolytic in-Process Dressing, J. Mater. Process. Technol. 98(3) (2000) 322-327.

[55] H. Ohmori, K. Katahira, Y. Akinou, J. Komotori, M. Mizutani, Investigation on Grinding Characteristics and Surface-Modifying Effects of Biocompatible Co-Cr Alloy, CIRP Annals - Manuf. Technol. 55(1) (2006) 597-600.

[56] J.-S. Heo, Y. Koo, S.-S. Choi, Grinding Characteristics of Conventional and Elid Methods in Difficult-to-Cut and Hardened Brittle Materials, J. Mater. Process. Technol. 155-156 (2004) 1196-1200.

[57] B.P. Bandyopadhyay, H. Ohmori, The Effect of Elid Grinding on the Flexural Strength of Silicon Nitride, Int. J. Mach. Tools and Manuf. 39(5) (1999) 839-853.

[58] C. Zhang, T. Kato, W. Li, H. Ohmori, A Comparative Study: Surface Characteristics of Cvd-Sic Ground with Cast Iron Bond Diamond Wheel, Int. J. Mach. Tools and Manuf. 40(4) (2000) 527-537.

[59] Y. Dai, H. Ohmori, Y. Watanabe, H. Eto, W. Lin, T. Suzuki, Subsurface Properties of Ceramics for Lightweight Mirrors after Elid Grinding, JSME International Journal Series C Mechanical Systems, Machine Elements and Manufacturing 47(1) (2004) 66-71.

[60] D.J. Stephenson, D. Veselovac, S. Manley, J. Corbett, Ultra-Precision Grinding of Hard Steels, Precis. Eng. 25(4) (2001) 336-345.

[61] K. Katahira, Y. Watanabe, H. Ohmori, T. Kato, Elid Grinding and Tribological Characteristics of Tialn Film, Int. J. Mach. Tools and Manuf. 42(12) (2002) 1307-1313.

[62] K. Katahira, H. Ohmori, Y. Uehara, M. Azuma, Elid Grinding Characteristics and Surface Modifying Effects of Aluminum Nitride (Aln) Ceramics, Int. J. Mach. Tools and Manuf. 45(7-8) (2005) 891-896.

[63] S. Yin, S.-y. Morita, H. Ohmori, Y. Uehara, W. Lin, Q. Liu, T. Maihara, F. Iwamuro, D. Mochida, Elid Precision Grinding of Large Special Schmidt Plate for Fibre Multi-Object Spectrograph for 8.2 m Subaru Telescope, Int. J. Mach. Tools and Manuf. 45(14) (2005) 1598-1604.

[64] Q. Zhao, Y. Liang, D. Stephenson, J. Corbett, Surface and Subsurface Integrity in Diamond Grinding of Optical Glasses on Tetraform [`]C', Int. J. Mach. Tools and Manuf. 47(14) (2007) 2091-2097.

[65] H. Chen, J.C.M. Li, Anodic Metal Matrix Removal Rate in Electrolytic in-Process Dressing Ii: Protrusion Effect and Three-Dimensional Modeling, J. Appl. Phys. 87(6) (2000) 3159-3164.

[66] H. Chen, J.C.M. Li, Anodic Metal Matrix Removal Rate in Electrolytic in-Process Dressing I: Two-Dimensional Modeling, J. Appl. Phys. 87(6) (2000) 3151-3158.

[67] J.A. McGeough, Principles of Electrochemical Machining, Chapman and Hall, London, 1974.

[68] K.P. Rajurkar, J. Kozak, B. Wei, J.A. McGeough, Study of Pulse Electrochemical Machining Characteristics, CIRP Annals - Manuf. Technol. 42(1) (1993) 231-234.

[69] K.P. Rajurkar, B. Wei, J. Kozak, J.A. McGeough, Modelling and Monitoring Interelectrode Gap in Pulse Electrochemical Machining, CIRP Annals - Manuf. Technol. 44(1) (1995) 177-180.

[70] K.P. Rajurkar, D. Zhu, J.A. McGeough, J. Kozak, A. De Silva, New Developments in Electro-Chemical Machining, CIRP Annals - Manuf. Technol. 48(2) (1999) 567-579.

[71] J. Kozak, K.P. Rajurkar, Y. Makkar, Selected Problems of Micro-Electrochemical Machining, J. Mater. Process. Technol. 149(1-3) (2004) 426-431.

[72] K.P. Rajurkar, C.L. Schnacker, R.P. Lindsay, Some Aspects of Ecm Performance and Control, CIRP Annals - Manuf. Technol. 37(1) (1988) 183-186.

[73] K.P. Rajurkar, D. Zhu, B. Wei, Minimization of Machining Allowance in Electrochemical Machining, CIRP Annals - Manuf. Technol. 47(1) (1998) 165-168.

[74] E.C. Jameson, Electrical Discharge Machining, Society of Manufacturing Engineers, 2001.

[75] M.M. Islam, A.S. Kumar, S. Balakumar, H.S. Lim, M. Rahman, Characterization of Elid Grinding Process for Machining Silicon Wafers, J. Mater. Process. Technol. 198(1-3) (2008) 281-290.

[76] J.H. Liu, Z.J. Pei, G.R. Fisher, Elid Grinding of Silicon Wafers: A Literature Review, Int. J. Mach. Tools and Manuf. 47(3-4) (2007) 529-536.

[77] C. Zhang, H. Ohmori, T. Kato, N. Morita, Evaluation of Surface Characteristics of Ground Cvd-Sic Using Cast Iron Bond Diamond Wheels, Precis. Eng. 25(1) (2001) 56-62.

[78] G.T. Burstein, A.J. Davenport, The Current-Time Relationship During Anodic Oxide Film Growth under High Electric Field, J. Electrochem. Soc. 136(4) (1989) 6.

[79] H. Cichy, E. Fromm, Oxidation-Kinetics of Metal-Films at 300-K Studied by the Piezoelectric Quartz Crystal Microbalance Technique, Thin Solid Films 195(1-2) (1991) 147-158.

[80] H.J. Pearson, G.T. Burstein, R.C. Newman, Resistance to Flow of Current to Scratched Electrodes, J. Electrochem. Soc. 128(11) (1981) 2297-2303.

[81] P.B. Abel, A.H. Heuer, R.W. Hoffman, Measurement of Oxide Growth Stress on Thin Iron Films, J. Vac. Sci. Technol., A 1(2) (1983) 260-262.

[82] Z.B. Hou, R. Komanduri, On the Mechanics of the Grinding Process - Part I. Stochastic Nature of the Grinding Process, Int. J. Mach. Tools and Manuf. 43(15) (2003) 1579-1593.

[83] H. Yoshikawa, T. Sata, Study on Wear of Grinding Wheels 1: Bond Fracture in Grinding Wheels, Trans. ASME, J. Eng. Ind. February 1963 (1963) 5.

[84] H. Yoshikawa. Fracture Wear of Grinding Wheels. *ASME Production Engineering Research Conference*, pp. 209-2171963).

[85] S. Malkin, N.H. Cook, The Wear of Grinding Wheels Part 1 - Attritious Wear, Trans. ASME, J. Eng. Ind. November 1971 (1971) 9.

[86] P. Koshy, V.K. Jain, G.K. Lal, A Model for the Topography of Diamond Grinding Wheels, Wear 169(2) (1993) 237-242.

[87] S. Malkin, Grinding Technology - Theory and Applications of Machining with Abrasives, Ellis Horwood Ltd, Chichester, England, 1989.

[88] T.W. Hwang, S. Malkin, Grinding Mechanics and Energy Balance for Ceramics, J. Manuf. Sci. Eng. 121(November) (1999) 10.

PUBLICATIONS

Journals

- Saleh, T., Biswas, I., Lim, H. S., Rahman, M.; In-process Truing of Metal-bonded Diamond Wheels for Electrolytic In-process Dressing (ELID) Grinding; *International Journal of Precision Engineering and Manufacturing* Vol. 9, No.2, 2008;

- Rahman, M., Senthil Kumar, A., Biswas, I.; A Review of Electrolytic In-Process Dressing (ELID) Grinding; Key Engineering Materials Vol. 404, *Progress in Abrasive and Grinding Technology*, 2009, pp 45-59;

- Saleh, T., Biswas, I., Rahman, M.; Efficient dressing of the wheel in ELID grinding by controllable voltage with force feed back; *International Journal of Advanced Manufacturing Technology*, published online;

- Biswas, I., Senthil Kumar, A., Rahman, M.; A Study on the Equilibrium Condition of the Oxide Layer in ELID Grinding, *International Journal of Abrasive Technology* (accepted);

- Biswas, I., Senthil Kumar, A., Rahman, M.; Experimental Studies of Wheel Wear in Electrolytically Dressed Grinding, *International Journal of Advanced Manufacturing Technology* (under review);

- Biswas, I., Senthil Kumar, A., Rahman, M.; Studies on Impedance of Electrolyte in Electrolytic In-process Dressing (ELID) Grinding, *International Journal of Advanced Manufacturing Technology* (under review);

Conferences

- Biswas, I., Balakumar, S., Senthil Kumar, A., Nagarajan, R., Rahman, M.; ELID technique for copper polishing to prepare through wafer interconnects, Symposium on Microelectronics, Institute of Microelectronics, Singapore, 2006;

- Biswas, I., Saleh, T., Senthil Kumar, A., Lim, H. S., Rahman, M.; Experimental Study on the growth of Oxide Layer in ELID Grinding, Proceedings of the 7th euspen International Conference, Germany, 2007;

- Biswas, I., Saleh, T., Senthil Kumar, A., Lim, H. S., Rahman, M.; Some Studies on Oxide Layer Formation in ELID Grinding, International Conference on Precision, Meso, Micro and Nano Engineering, India, 2007;

Journals Under Preparation

- Biswas, I., Senthil Kumar, A., Rahman, M.; Estimation of Wheel Wear in Electrolytic In-process Dressing (ELID) and Grinding;

- Biswas, I., Senthil Kumar, A., Lim, Rahman, M.; Model for Wheel Wear in Electrolytic In-Process Dressing (ELID) and Grinding;